Università degli Studi di Firenze
Scuola di Ingegneria
DIEF - Department of Industrial Engineering of Florence

PhD School: *Energetica e Tecnologie Industriali ed Ambientali Innovative*
Scientific Area: ING-IND/08 - *Macchine a Fluido*

Experimental Investigation of Windage and Churning Power Losses of a Spiral Bevel Gears

PhD Candidate: Ing. Sofia Brocchi

Academic supervisor: Prof. Ing. Bruno Facchini

PhD School Coordinator: Prof. Ing. Lapo Governi

XXXVIII PhD School Cycle - 2022-2025

©Università degli Studi di Firenze – Faculty of Engineering
Via di Santa Marta, 3, 50139 Firenze, Italy.

Tutti i diritti riservati. Nessuna parte del testo può essere riprodotta o trasmessa in qualsiasi forma o con qualsiasi mezzo, elettronico o meccanico, incluso le fotocopie, la trasmissione fac simile, la registrazione, il riadattamento o l' uso di qualsiasi sistema di immagazzinamento e recupero di informazioni, senza il permesso scritto dell' editore.

All rights reserved. No part of the publication may be reproduced in any form by print, photoprint, microfilm, electronic or any other means without written permission from the publisher.

Ai miei Genitori

Acknowledgements

Alla fine di un percorso è necessario trarre delle conclusioni, guardandomi indietro ho capito che da sola non ce l'avrei mai fatta e per questo penso che sia necessario ringraziare quelle persone che hanno reso tutto questo possibile. Oggi un grazie immenso va alle persone che mi sono state accanto in questo percorso, supportandomi, ma soprattutto sopportandomi, ogni giorno. Coloro che hanno creduto nelle mie capacità e nei miei sogni, anche quando io ero la prima a crederci poco. Quelle persone che sono state un porto sicuro in cui rifugiarmi e che sempre lo saranno; che hanno cercato di alleviare le mie ansie quando tutto mi sembrava così complicato e più grande di me. In particolar modo, a te Riess, che sei il mio punto di riferimento. Un grazie speciale va al mio relatore; il Prof. Bruno Facchini per le conoscenze e la passione che mi ha trasmesso nel corso di questi anni e per le opportunità datemi. La mia gratitudine va a tutte le persone del laboratorio THT Lab per la cordialità e il calore con cui sono stata accolta e l'atmosfera piacevole che ha accompagnato la mia prima esperienza in un ambiente di lavoro. Infine, ringrazio i miei genitori per i tanti sacrifici fatti, per il sostegno morale, per quella forza d'animo e coraggio trasmesso che mi ha permesso di arrivare alla fine di un percorso così lungo e difficile ma pieno di soddisfazioni. A loro che con il loro amore mi hanno insegnato a vivere.

Publications

International Conferences

- Orsini, L., Picchi, A., Facchini, B., Bonini, A., Brocchi, S., Innocenti, L. (2023). Commissioning of a Newly Designed Experimental Facility for Hot Gas Ingestion Investigation. In 15th European Conference on Turbomachinery Fluid dynamics & Thermodynamics. EUROPEAN TURBOMACHINERY SOCIETY.

- Brocchi, S., Fratini, A., Becchi, R., Facchini, B., Lo Santo, G., Konle, M., Andreini, A. (2026). Windage power losses in high-speed spiral bevel gears: A preliminary experimental and numerical evaluation. In Turbomachinery Technical Conference of ASME.

Abstract

Power transmission systems are critical dynamic components in the field of aeronautics, as they directly influence propulsive efficiency and fuel consumption, thereby affecting overall engine performance. Since significant power losses occur in transmission systems such as gearboxes, minimizing these losses is a primary design objective. In particular in splash lubricated systems, losses may be divided into windage and churning types which are generally both significant for the conditions typical of aeronautical transmission systems. This study investigates windage and churning power losses in spiral bevel gears, which arise from aerodynamic and fluid-dynamic effects and become increasingly significant at high rotational speeds and low-load conditions. An experimental test rig was used to systematically study the power losses of spiral bevel gears, varying both the characteristic geometric parameters of the gears and the operating conditions, and measuring both types of losses. During the preliminary phase, the rig was used to assess the windage losses of a single bevel gear operating in an air-only environment. In parallel with this experimental campaign, a physical model for spiral bevel gears was developed, based on and building upon existing models originally reported to predict windage losses in spur gears. In addition, a velocimetry test campaign was conducted to study the windage velocity field within the casing. In a subsequent test campaign, churning losses were evaluated for the same gears and operating conditions but with the presence of the oil bath at varying immersion depths of the gears and with varying oil properties. Velocimetry was also applied to the tests of the churning test

campaign and a post-processing methodology was developed to obtain phase-averaged velocity fields of the oil projected by the gear above the oil bath. The results of this work represent a characterization of the effect of major spiral bevel gear parameters on power losses as well as demonstrate a methodology for analyzing in a robust way the highly unsteady oil velocity fields resulting from optical velocity measurements of splash lubricated gears.

Contents

Publications v

Abstract vii

Contents xi

Nomenclature xiii

1 Introduction 1

1.1 Gearboxes Background 1

1.1.1 Lubrication 4

1.2 Gearboxes Losses 6

1.3 Aim of the work 7

1.4 Thesis outline 8

2 Literature Review 11

2.1 Introduction 12

2.2 Windage Losses 13

2.2.1 Spur Gear 15

2.2.2 Bevel gear 22

2.3 Churning Losses 24

2.3.1 Flow regimes 26

2.3.2 Influence of gear tooth geometry 26

2.3.3 Influence of wall clearance 33

2.4 Presentation of Models Based on Different Approaches . . 34
2.4.1 Models Based on Experimental Approaches 34
2.4.2 Changenet et al. Model 35
2.4.3 Models Based on Analytical Approaches 36
2.5 Loss models for bevel gears 37
2.5.1 Jeon Model 37
2.5.2 Laruelle and Fossier Model 38
2.5.3 Quiban et al. 39
2.6 Phase Lock Average 41
2.7 Proper Orthogonal Decomposition 43
2.8 Phase Identification Based on Proper Orthogonal Decomposition 52
2.9 Particle Image Velocimetry 56
2.9.1 PIV data post processing 58
2.10 PIV applied to multi-phase flow 60
2.10.1 Particle Tracking Velocimetry 61
2.10.2 LIF-PIV 62
2.10.3 Shadow Photography 63
2.10.4 Planar Fluorescence for Bubble Imaging 64

3 Methodology **67**
3.1 Test rig overview 67
3.2 Description of the test rig 68
3.2.1 Chamber 69
3.2.1.1 Gear Geometries. 71
3.2.2 Power Losses Measurement 74
3.2.2.1 Uncertainty Analysis. 75
3.3 Physical model definition 76
3.4 PIV measurement set-up 80
3.5 Application of POD for the study of splash lubricated gears 84

4 Results **87**
4.1 Windage Power Losses 87
4.1.1 Physical Model Validation 91

4.2 Churning Power Losses 94
4.3 Velocimetry 106
4.3.1 Windage 107
4.3.2 Churning 108
4.3.2.1 Average PIV Results 108
4.3.2.2 Phase-Average PIV Results 111

Conclusions **123**

List of Figures **130**

List of Tables **131**

Bibliography **133**

Nomenclature

b	Gear width	$[m]$
C	Adimensional torque coefficient	$[-]$
$D(x,t)$	Original collection of measurements in space and time (POD)	$[-]$
D_0	Time-average solution (POD)	$[-]$
Fr	Froude number	$[-]$
g	Gravitation acceleration	$[m/s^2]$
h	Oil immersion depth	$[m]$
$\tilde{D}$	k-th POD mode	$[-]$
K	Temporal correlation matrix (POD)	$[-]$
M_g	Resisting torque	$[N \cdot m]$
n	Rotational speed	$[rpm]$
T	Gear tooth passing period	$[s]$
P	Power losses	$[W]$
R	Radius	$[m]$
Re	Reynolds number	$[-]$
S_m	Immersed surface area of the gear	$[m^2]$
V_0	Oil volume	$[m^3]$
V	Velocity	$[m/S]$
Z	Number of teeth	$[-]$

Acronyms

ACW	Anticlockwise

CFD	Computational Fluid Dynamics
$CLAHE$	Contrast Limited Adaptive Histogram Equalization
GT	Gas Turbine
IA	Interrogation Area
LIF	Laser Induced Fluorescence
$PFBI$	Planar Fluorescence for Bubble Imaging
PIV	Particle Image Velocimetry
PLA	Phase Lock Average
POD	Proper Orthogonal Decomposition
PTV	Particle Tracking Velocity
SFC	Specific Fuel Consumption
SP	Shadow Photography

Greeks

α	Pressure angle	$[rad]$
δ	Cone angle	$[rad]$
θ	Mean spiral angle	$[-]$
	Phase angle	$[rad]$
λ	Lagrangian Multiplier	$[-]$
μ	Dynamic viscosity	$[Pa \cdot s]$
ν	Kinematic viscosity	$[m^2 \cdot s^{-1}]$
ρ	Density	$[kg \cdot m^{-3}]$
Σ	Matrix of eigenvalues of the data correlation matrix	$[-]$
σ_r	Eigenvalues of the data correlation matrix	$[-]$
Φ	Matrix of POD spatial distributions	$[-]$
	Cross-correlation function PIV	$[-]$
Ψ	Matrix of eigenvectors of the correlation matrix	$[-]$
ω	Angular velocity	$[rad \cdot s^{-1}]$

Subscripts

c	Cone reference

Ch	Churning
m	Torque
tan	Tangential
wi	Windage

Superscripts

$*$	Parameters refer to spur gear geometry

Chapter 1

Introduction

Contents

1.1 Gearboxes Background **1**
1.1.1 Lubrication 4
1.2 Gearboxes Losses **6**
1.3 Aim of the work **7**
1.4 Thesis outline **8**

1.1 Gearboxes Background

Over the years, in order to improve energy efficiency and mitigate environmental impact by reducing emissions, noise, and fuel consumption (SFC) in mechanical engines, it has become necessary to achieve ever greater machine efficiency through advances in combustion technology and improvements in transmission performance.

Power transmission systems are critical dynamic components in the aeronautical field, and an evaluation of their structure and performance is required to optimize design and maximize efficiency.

Although state-of-the-art transmissions can achieve efficiencies above 99% [1], in high power applications residual power losses can be significant in absolute terms, on the order of $100 - 200$ MW. These losses not only

reduce the overall efficiency of the system, but also generate heat that must be removed by the lubrication and cooling circuits, which in turn add weight, additional losses caused by drag and complexity to the thermal management system.

Transmission systems include different components such as gears, bearings, seals, and auxiliary circuits, which influence the overall performance under different operating conditions, such as high or low loads and speeds. The total power loss of a gearbox, P_L, can be expressed as the sum of the contributions associated with the gears, P_{LG}, bearing, P_{LB}, seals, P_{LS}, and other losses, P_{LX}. The power losses associated with gears and bearings can be further classified into load-dependent and load-independent components, conventionally denoted by subscripts "P" and "0", respectively, as shown in Fig. 1.1.

$$P_L = P_{LG} + P_{LG0} + P_{LB} + P_{LB0} + P_{LS} + P_{LX}$$

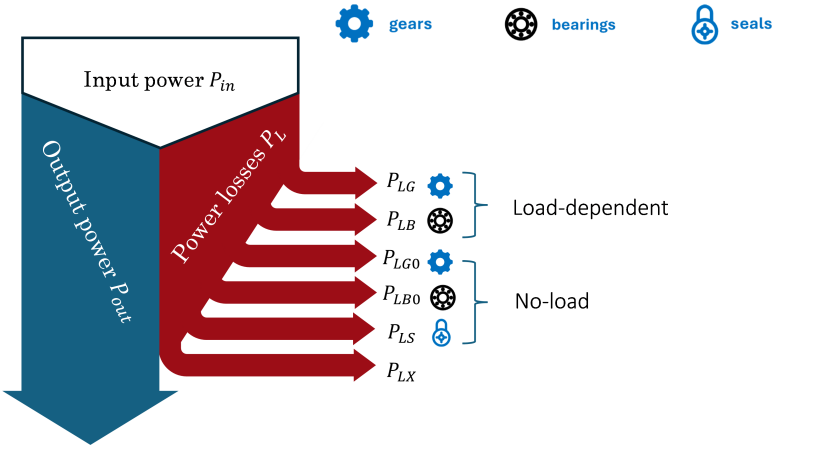

Figure 1.1: General gearbox power losses [2]

Load-dependent and load-independent power losses should be distinguished since they arise from different physical mechanisms. Load-dependent losses are mainly related to friction in the tribological contacts

and depend on the type and size of the components, their sliding velocity in the contact areas, coefficient of friction, and transmitted power. In contrast, load-independent losses are associated with the interaction of the components with the lubricant and are influenced by the operating conditions and housing design. Similarly, "no-load power loss" should not be used interchangeably with "load-independent power loss", as the former refers to the total power loss measured when no useful power is transmitted, whereas the latter describes a specific class of loss mechanisms that can also occur under load. Further details on this distinction can be found in Hildebrand et al. [3].

A physical understanding of the loss mechanisms is therefore essential to support the development of next-generation transmission systems. In transmission systems, different types of gears can be used. The most common geometries include cylindrical gears, which are economical, simple in design, and allow power transmission between parallel shafts; helical gears, always used in parallel configurations, which can achieve higher transmission power but generate significant thrust forces that must be compensated by bearings.

Among the various types of gears used in transmission systems, bevel and hypoid gears are widely employed to transfer power between non-parallel shafts. Bevel gears are characterized by intersecting shaft axes, whereas hypoid gears have offset, non-intersecting shaft axes. This difference in geometry results in distinct contact conditions and operating characteristics. In this work, the focus is placed on bevel gears, with particular attention to their power losses and efficiency under different operating conditions. Their ability to transmit power between intersecting shafts makes bevel gears suitable for numerous applications, ranging from industrial machinery and vehicles to aircraft, including helicopters. In helicopter engines, a gas turbine (GT) is usually used to drive the main and tail rotors. The GT and the main rotor are mounted horizontally and vertically, respectively; for this reason, an angular gear train is required to transmit power between them. The maximum rotational speed of the GT, which can reach up to 18000 rpm, is reduced by one or more set of bevel

gears to achieve a rotor speed typically below 500 rpm, depending on the diameter of the rotor, to keep the blade tip velocity subsonic. In addition, bevel gear sets are used to redirect the rotation of the main driveshaft toward the tail rotor, compensating for the counter torque generated by the main rotor around the vertical axis, see Fig.1.2. Since these solutions require stringent space constraints and a compact design, most bevel gearboxes have a shaft angle of less than 90°. These requirements make helicopter transmissions the most advanced and complex application of bevel gear systems [4].

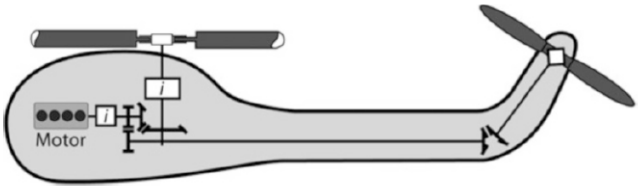

Figure 1.2: Principle of a helicopter drive train [5]

1.1.1 Lubrication

Splash lubrication is a common method for gearbox systems because oil can be easily introduced inside the gearbox and allows to reduce friction and wear, as well as dissipate the heat generated in the gear mesh. Usually, the lubricant is seeded with additives that enhance its properties and help protect the gears against corrosion, wear, and scuffing.
Various types of lubricants are available on the market. In industrial applications, CLP mineral oils are the most commonly used, in accordance with DIN standards. However, when superior performance is required in terms of operating temperature range, durability, and viscosity–temperature behavior (high viscosity index, VI), synthetic oils, as specified by MIL standards, are the preferred choice.
The viscosity of lubricating oil is a key factor in selecting the appropriate lubricant, so a compromise between temperature and operating conditions

must be found. Lubricant viscosity is influenced by temperature, load, and operating circumferential speed. Special additives may be used in the case that oil viscosity is not sufficient to form a protective elastohydrodynamic lubricant film on gear tooth flanks. Higher loads require more viscous oils to maintain sufficient film thickness, whereas at high speeds this is less critical. However, excessively viscous oils increase friction and energy losses under no-load conditions. If the oil viscosity is not sufficient to protect the gear teeth, special additives are used to form a protective chemical film on the surface. Niemann and Winter [6] provide a recommendation for selection of the oil viscosity as a function of circumferential speed, serving as a starting point for lubricant selection, see Fig.1.3.

In aeronautical applications, synthetic polyol ester (POE) oils are com-

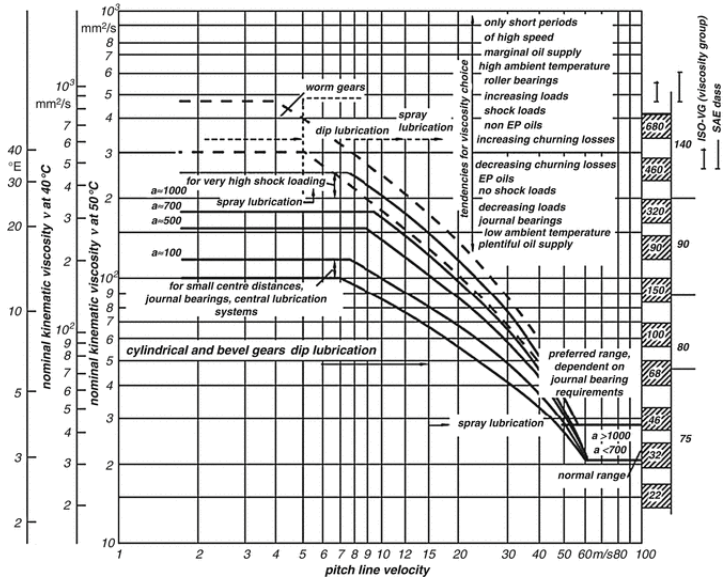

Figure 1.3: Niemann -Winter model for oil viscosities [7]

monly used because the gears are subjected to high operating temperatures and high peripheral speeds.

There are several methods for lubricating gearboxes. In low-speed and low-load applications, the lubrication method has little impact on overall system efficiency. For medium to high-speed applications, however, methods such as splash lubrication or forced oil recirculation are typically used. Splash lubrication is usually adopted in enclosed systems. However, it presents significant issues related to oil level: if the level is too high, excessive losses occur due to agitation, while if it is too low, lubrication and cooling become ineffective. Operating temperature is also a concern, as it can rise due to friction losses inside the gearbox, leading to reduced lubricant viscosity, accelerated oil degradation, and potential deformation of the housing, gears, or shafts.
On the other hand, the forced oil recirculation method continuously circulates the lubricant through the gearbox and uses nozzles to create small oil jets sprayed directly onto the gear contact areas. This method requires auxiliary components such as pumps, oil tanks, filters, and nozzles to ensure continuous oil circulation; for this reason, it is typically used only in high-speed applications and large gearbox arrangements.

However, oil bath lubrication introduces additional losses, such as churning and windage effects, which become particularly relevant at high rotational speeds. Since no single loss source dominates total power dissipation, a detailed investigation of all mechanisms is necessary to enable a meaningful reduction in gearbox power losses.

1.2 Gearboxes Losses

Gear power transmissions remain the most common method of mechanical power transfer due to their high power density, reliability, and precision. In high-performance applications, such as aerospace gearboxes or automotive differentials, even modest improvements in loss prediction and reduction can yield substantial industrial and economic benefits.

However, the efficiency of gear transmissions is affected by multiple sources of mechanical loss. These losses not only reduce the overall energy efficiency of the system but also generate excess heat, which influences

lubrication regimes and reduces component lifetime. In applications where performance and efficiency are critical, such as aerospace gearboxes or high-performance automotive differentials, even small improvements in loss prediction and reduction can yield significant industrial and economic benefits.

Generally, the sources of power loss in such systems are classified into two main groups:

- load-dependent;
- load-independent.

Load-dependent losses are associated with friction at the gear contacts and within the bearing races, whereas load-independent losses arise from fluid-dynamic effects, which are in turn influenced by the lubrication method. Among fluid-dynamic losses, churning and windage losses become particularly relevant at high rotational speeds. Churning losses arise from the interaction between rotating gears and the lubricant when the gears are partially or fully immersed in oil, and are therefore mainly associated with oil-bath or splash lubrication. Windage losses, on the other hand, are caused by aerodynamic drag as the gears rotate in air or oil mist and can occur also in non-immersed lubrication conditions. Although load-dependent losses tend to dominate under high-load and low-speed operating conditions, load-independent losses become increasingly significant at high rotational speeds and low loads, as typically encountered in aerospace and other high-speed mechanical systems.

1.3 Aim of the work

The present research focuses on an experimental study of spiral bevel gears operating under various splash lubrication conditions, aiming to characterize the contributions to power loss. The goal is to develop and validate a methodology for studying the interaction between gear teeth and lubricating oil experimentally. Such methodology is composed of torque and velocity field measurements for a variety of test conditions

(different speeds, oil levels, oil type) and geometrical configurations. It is useful not only for characterizing the gear-oil interactions but also for providing a reference for numerical simulations which attempt to model splash-lubricated gears and estimate their power losses. Therefore, it contributes to the broader objective of improving transmission efficiency in high-performance applications, ultimately enabling more sustainable and environmentally friendly engineering solutions.

1.4 Thesis outline

During this research activity, windage and churning power losses of single high-speed spiral bevel gears, operating under splash-lubricated conditions, were analysed from both an experimental and a correlative point of view. The gears were investigated at circumferential speeds up to 60 m/s, representative of high-speed operating conditions in aerospace transmission systems.

The experimental data were carried out from torque measurements and by Particle Image Velocimetry (PIV). In particular, the PIV measurements focused on measuring the velocity of the oil projected by the gear above the oil bath, using an approach not previously seen in the literature. The results highlighted some characteristic behaviors of churning loss phenomena in splash-lubricated gears allowing to deepen the knowledge of these systems and to provide useful information for bench-marking of numerical simulations an for experimental investigations of more complex models such as gear and pinion systems.

Chapter 2. Describes the background of the power losses in geared transmissions and reviews some of the most important works and research regarding windage and churning power losses for gears. Moreover, the basis of the PIV and subsequent post-processing methods based on Phase-Locked Averaging (PLA) and Proper Orthogonal Decomposition (POD) is reviewed.

Chapter 3. In this chapter experimental facility and measurements set up are described. The measurements are divided in two main categories: torque and velocimetry. Moreover, an extension of an open-literature physical model to predict windage power losses for spiral bevel gears is proposed.

Chapter 4. In this part of the work all experimental results are presented and discussed, including the validation of the physical model for windage losses, the churning results for a variety of test conditions, and the velocimetry results characterizing the interaction between the gear and oil bath.

Chapter 5. The last chapter provides a summary of the main achievements of this research, together with the conclusions.

Chapter 2

Literature Review

Contents

2.1 Introduction 12
2.2 Windage Losses 13
2.2.1 Spur Gear 15
2.2.2 Bevel gear 22
2.3 Churning Losses 24
2.3.1 Flow regimes 26
2.3.2 Influence of gear tooth geometry 26
2.3.3 Influence of wall clearance 33
2.4 Presentation of Models Based on Different Approaches 34
2.4.1 Models Based on Experimental Approaches 34
2.4.2 Changenet et al. Model 35
2.4.3 Models Based on Analytical Approaches . . 36
2.5 Loss models for bevel gears 37
2.5.1 Jeon Model 37
2.5.2 Laruelle and Fossier Model 38
2.5.3 Quiban et al. 39
2.6 Phase Lock Average 41
2.7 Proper Orthogonal Decomposition 43
2.8 Phase Identification Based on Proper Orthogonal Decomposition 52

2.9 Particle Image Velocimetry 56
2.9.1 PIV data post processing 58
2.10 PIV applied to multi-phase flow 60
2.10.1 Particle Tracking Velocimetry 61
2.10.2 LIF-PIV 62
2.10.3 Shadow Photography 63
2.10.4 Planar Fluorescence for Bubble Imaging . . 64

2.1 Introduction

This chapter presents the theory of power losses in geared transmission systems.

As previously introduced in Chapter 1, gear power transmission systems are the most common and efficient way to transmit power. However, in order to further improve their efficiency, a deeper understanding and investigation of losses within these systems from both a physical and fluid-dynamic point of view is required. The different sources of loss, which vary with operating conditions such as load and speed, as well as with geometry, can influence the overall efficiency in different ways.

The load-dependent power losses, caused by friction at meshing gear surfaces, within bearing races and between rolling elements, have been deeply studied in the past, and suitable models are available in the open literature to estimate them [8]. With regard to load-independent power losses, caused by the interaction between the lubricant and rotating elements, they are still difficult to predict and for that also to reduce. Only for splash lubrication, this group can be further divided into Churning and Windage power losses, the first are caused by the viscous drag of the lubricant under a dip lubrication conditions, while the latter are related to the presence of a single-phase lubricant mixture (usually air or oil). In very high-speed gearboxes, which are typical of aero-engine applications where the pitch-line speed exceeds 100 m/s, fluid-dynamic losses account for the majority of the gearbox's overall power loss. The relative size of these losses varies depending on the application. However, windage effects

are extremely important in high-speed gearing systems and can dominate other loss mechanisms [9]. For splash-lubricated gears, churning losses are an important component of no-load losses, so an accurate evaluation of this dissipation source is required [10]. In low- to medium-speed applications, gear losses are predominantly due to tooth friction and lubricant churning, whereas at high speeds windage effects become the major contributor.

2.2 Windage Losses

Windage power losses are caused by aerodynamic forces and fluid drag as gears rotate in air or an air–oil mist. In some applications, such as aeroengines, gears are mounted inside bearing chambers and operate under high-speed, light-load conditions. Under these conditions, windage power losses can become significant and contribute to an increase in oil temperature, making them an important factor in the thermal management and overall efficiency of the transmission system. A review of gear power losses for spur, helical, and bevel gears is presented in [11], which provides valuable experimental data and modeling approaches. However, since in open literature limited informations are available on gear windage loss mechanisms, it can be useful to begin with the study of windage losses generated by rotating disk, which can be considered as a simplification of an single spur gear. Numerous studies have investigated a disk rotating in a fluid with constant angular velocity ω about a vertical axis perpendicular to its plane. The moment of the surface frictional forces was first resolved by Von Kármán [12], for both laminar and turbulent flow. The Navier–Stokes equations for the boundary layer in laminar flow over a rotating disk were solved by Von Kármán for both sides of the disk, neglecting edge effects. The solution was:

$$2M = 1.84R^4\rho\nu^{1/2}\omega^{3/2} \tag{2.1}$$

where M is the moment of frictional foces to one side of the disk.

In turbulent flow conditions, the rotational Reynolds number Re_ϕ is greater than about 10^5 [13]. It depends on the disk radius and the tip

velocity, as shown in Equation 2.2.

$$Re_\phi = \frac{R^2\omega}{\nu} \tag{2.2}$$

By approximating the boundary layer velocity profile using a 1/7 power law model, Von Kármán found that the torque for the turbulent case was given by the following Equation 2.3:

$$2M = 0.0728R^5\omega\rho\left(\frac{\nu}{R^2}\omega\right)^{1/5} \tag{2.3}$$

Both equations can be described in terms of the moment coefficient, C_m, as given by equation 2.4. This yields equations 2.5 and 2.6 that describe laminar and turbulent flows, respectively.

$$C_m = \frac{2M}{\frac{1}{2}\rho\omega^2 R^5} \tag{2.4}$$

$$C_m = 3.68Re_\phi^{-1/2} \tag{2.5}$$

$$C_m = 0.146Re_\phi^{-1/5} \tag{2.6}$$

In 1935, Goldstein addressed the turbulent boundary layer on a rotating disk [13]. To better reproduce a particular set of experimental data, he assumed a logarithmic profile for the boundary layer velocity. He achieved a moment coefficient of the form:

$$C_m^{-1/2} = 1.97log\left(Re_\phi C_m^{1/2}\right) + 0.03 \tag{2.7}$$

Dorfman [14] investigated turbulent flow due to rotating disks with smooth and rough surfaces. Assuming a logarithmic velocity profile, he obtained the momentum coefficient given by Equation 2.8 for smooth surfaces. For rough surfaces, he derived the C_m reported in Equation 2.9, assuming a fully turbulent boundary layer.

$$C_m = 0.982\left(logRe_\phi\right)^{-2.58} \tag{2.8}$$

$$C_m = 0.108\left(\frac{k_s}{Re_\phi}\right)^{0.272} \tag{2.9}$$

In summary, the moment experienced by a rotating disk is entirely due to shear forces. Every author found that the torque related to both sides of the disk depends linearly on fluid density, quadratically on angular velocity, and on the disk radius to the fifth power. Their formulations differ in the value of the moment coefficient, which is a decreasing function of the rotational Reynolds number.

2.2.1 Spur Gear

Estimates of the percentage impact of windage vary because the value depends on several different parameters; therefore, several experimental studies can be found in open literature. Townsend [15] identifies a series of factors that influence windage losses, highlighting pitch line velocity as a critical parameter. Windage effects become significant when the pitch line velocity exceeds 50 m/s. Townsend developed an empirical formula to estimate windage losses based on studies of smooth rotating bodies in air. However, as Townsend notes, this method cannot predict actual losses; rather, it is primarily used to determine when windage effects become a concern for designers.

Anderson and Loewenthal [16, 17] introduced an analytical method for calculating all losses in a gear train and developed a formula for a pinion-gear pair in mesh:

$$P = C_1\left(1 + 2.3\frac{t}{R_p}\right)n^{2.8}R_p^{4.6}(0.028 \cdot \mu + C_2)^{0.2} \tag{2.10}$$

where P is the power loss in $[kW]$, C_1 and C_2 are constants equal to $2.87 \cdot 10^{-7}$ and 0.019, respectively; R_p is the pitch radius in $[m]$, n is the rotational speed in $[rpm]$, ρ and μ are fluid properties, namely density in $[Kg/m^3]$ and viscosity in $[cP]$, respectively. This study involved relatively

low-speed gear, with pitch-line velocities up to 40 m/s.

In 1984, Dawson [18] conducted a study on windage losses in single spur gears, examining the effects of speed, size, gear geometry, and shrouding. The gears were operated in a spin-down test rig. The wheel was initially accelerated to a maximum rotational speed, reaching root-line velocities of up to approximately 90 m/s. Then, the power supply was disconnected, allowing the gear to decelerate freely. Windage power losses were calculated by measuring the deceleration rate. Dawson concluded that the primary source of gear windage losses was the gear teeth. Smoke visualization revealed that the gear teeth behave like the blades of a centrifugal fan. Air is drawn in from both ends of the teeth axially and expelled radially. Dawson then studied the effects of different baffle configurations, which included axial and radial shrouds with varying clearances. The windage was reduced by a certain percentage compared to the same gear rotating in free air. However, since this was tested on only one gear, these conclusions cannot necessarily be generalized to other cases. Based on the measurements, an empirical equation was developed to predict the windage power loss of a single gear. This is presented in Equation 2.11:

$$P = n^{2.9}\left(0.16D_r^{3.9} + D_r^{2.9}F^{0.75}M^{1.15}\right) \cdot 10^{-20}\Phi\lambda \tag{2.11}$$

Where P is the windage power loss in kW, D_r is the root diameter of the gear, F and M are the tooth face width and module in mm, respectively. Additionally, Φ is equal to 1 for an oil free atmosphere and λ ranges from $0.6 - 0.7$ for a gear operating withing a large casing, about $0.5 - 0.6$ in more confined conditions, and 1 in free air.

Building on Dawson's work, Diab et al. [19] carried out experiments on a single high-speed spur gear operating in an oil-free environment without any enclosures. They tested various spur gears using a spin-down rig, reaching pitch-line velocities of up to 100 m/s. They preposed two formulas to estimate windage power losses: one based on dimensional analysis and the other based on a simplified fluid flow analysis. The

experimental results were also used to evaluate the windage calculation models proposed by Anderson and Loewenthal [16] and Dawson [18]. The formulas developed by Diab were more accurate than the earlier models. Additionally, modifying the flow field near the gear teeth using baffles was shown to significantly reduce windage losses. Diab et al. [19] present a formulation (see Equation 2.12) that expresses the power loss P $[W]$ as a function of the fluid density ρ $[Kg/m^3]$, the rotational speed ω $[rad/s]$, he pitch radius R_p $[m]$ and the dimensionless total windage loss coefficient C_t.

$$P = \frac{1}{2} C_t \rho \omega^3 R_p^5 \tag{2.12}$$

Two different formulations were used to compute C_t. The first formulation was obtained using a dimensional analysis approach, which is denoted as Diab-DA.

$$C_t = \eta R_e^{\beta} \left(\frac{b}{R}\right)^{\gamma} Z^{\delta} \left\{ \left(\frac{h_1}{R}\right)^{\psi} + \left(\frac{h_2}{R}\right)^{\psi} \right\} \tag{2.13}$$

Where R, b, and Z denote the geometric gear parameters namely, the pitch radius, face width, and number of teeth, respectively. The coefficients α, β, γ, δ, and ε are empirical constants determined experimentally (see Table 2.1). Parameters h_1 and h_2 account for flanges adjacent to the gear teeth. When there are no side obstacles, $h_1 = h_2 = 0.5^{1/\psi} R$.

Table 2.1: Coefficients of the dimensional analysis formulation

α	β	γ	δ	ϕ
60	-0.25	0.8	-0.4	0.56

The second approach, referred to as Diab-FA, was based on a fluid-flow analysis. As shown in Equation 2.14, the power loss coefficient, C_t, is decomposed into two contributions: the windage loss generated by the front and rear faces of the gear (or disk) and the windage loss associated with the gear teeth. These contributions are represented by the coefficients C_f and C_l, respectively.

$$C_t = C_f + C_l \tag{2.14}$$

The gear face contribution is given by equation 2.15:

$$C_f = \frac{2n_1\pi}{5-2m_1}\frac{1}{Re^{*m_1}}\left(\frac{R^*}{R}\right)^5 + \frac{2n_2\pi}{5-2m_2}\left[\frac{1}{Re^{m_2}} - \frac{1}{Re^{*\,m_2}}\left(\frac{R^*}{R}\right)^5\right] \tag{2.15}$$

where n_1, m_1 and n_2, m_2 are coefficients associated with laminar and turbulent flows, respectively; their values are reported in Table 2.2. Re^* denotes the critical Reynolds number separating laminar and turbulent flow regimes and is fixed at 3×10^5. R represents the pitch radius, while $R^* = \sqrt{\mu Re^*/\rho\omega}$ is the critical radius separating the laminar and turbulent regions.

Table 2.2: Coefficients of the fluid flow analysis formulation.

n_1	m_1	n_2	m_2
1.293	0.5	0.072	0.2

Equation 2.16 provides the expression for the tooth coefficient:

$$C_l = \xi\frac{Z}{4}\left(\frac{b}{R}\right)\left[1+\frac{2(1+X_A)}{Z}\right]^4(1-\cos\theta)(1+\cos\theta)^3 \tag{2.16}$$

where X_A is the profile shift coefficient, ζ_p and ζ_a denote the pressure angles at the pitch point and at the tooth tip, respectively, while the angle θ is given by the following expression:

$$\theta = \frac{\pi}{Z} - 2(inv\zeta_p - inv\zeta_a) \tag{2.17}$$

where $inv\zeta$ denotes the involute function, which is expressed by Eq. 2.18:

$$inv\zeta = tan\zeta - \zeta \tag{2.18}$$

The contributions of deflectors or flanges are introduced through the reduction factor $\xi = \xi_1 + \xi_2$, which represents the influence of obstacles on the fluid aspiration by the gear teeth. Here, ξ_1 accounts for an obstacle on one side of the gear, while ξ_2 accounts for the obstacle on the opposite side. Both coefficients are defined by Equation 2.19 when deflectors or

flanges are present; otherwise, $\xi_1 = \xi_2 = 0.5$.

$$\xi_{1,2} = \left(\frac{h}{R}\right)^{0.56} \tag{2.19}$$

The formulation assumes that the gas flow over a given tooth is influenced by the preceding tooth in the direction of rotation, so that the active surface of the tooth is roughly bounded by a line extending from the tooth profile to the tip corner of the preceding tooth, as illustrated in the figure 2.1.

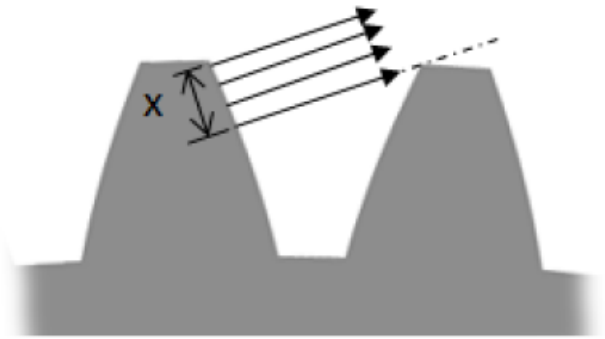

Figure 2.1: The active surface of the teeth is considered in the definition of the tooth coefficient [19].

A comparison was carried out among the windage power losses predicted by the formulations of Anderson and Loewenthal, Dawson, and Diab, as shown in Figures 2.2, 2.3, 2.4. A sample spur gear with a pitch diameter of 288 mm, a face width of 30 mm, a module of 4 mm and a pressure angle of 20° was considered. Experimental studies on single spur gears indicate an approximately cubic relationship between rotational speed and power loss (Fig. 2.2), a power-law dependence on the pitch radius with an exponent ranging between 3 and 5 (Fig. 2.3), and an almost linear dependence of windage losses on the gear face width (Fig.

2.4). Figure 2.2 shows the power losses predicted by Dorfman's correlation (Equation 2.8), which considers the contribution of both sides of a rotating disk. As Dawson concluded, the primary source of gear windage losses is the gear teeth. Thus, predictions obtained from Dorfman's formulation are significantly lower than those from correlations developed specifically for geared systems.

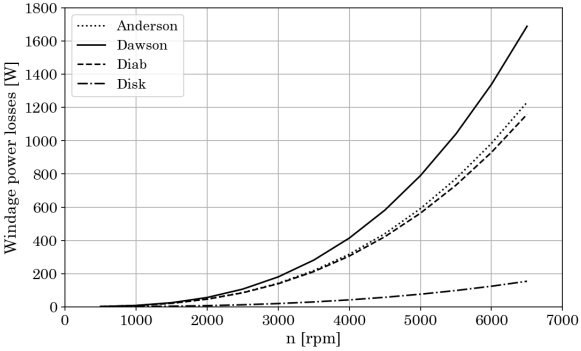

Figure 2.2: Windage power losses for a spur gear varying the rotational speed: comparison between the results obtained by the formulas of Anderson and Loewenthal, Dawson, Diab and Dorfman for a Rotating disk.

Voeltzel et al. [20] emphasized the significant influence of face width and helix angle on windage losses. They demonstrated that these parameters greatly impact the airflow structure within the inter-tooth regions of helical gears. Their numerical results also revealed parameter ranges that lead to reduced windage power losses. Furthermore, comparisons with Dawson's and Townsend's formulas showed significant discrepancies, especially for narrow-faced gears with large helix angles. This underlines the difficulty of defining a single, predictive formulation that is valid for all gear geometries.

Additionally, some experimental studies have investigated windage losses in gears. For example, Ruzek et al. [21] used an improved test rig to examine disk, spur and helical gears. They found that interactions during

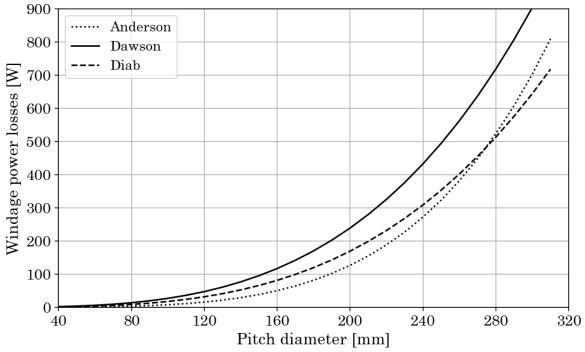

Figure 2.3: Windage power losses for a spur gear varying the pitch diameter: comparison between the results obtained by the formulas of Anderson and Loewenthal, Dawson, Diab at 5000 rpm.

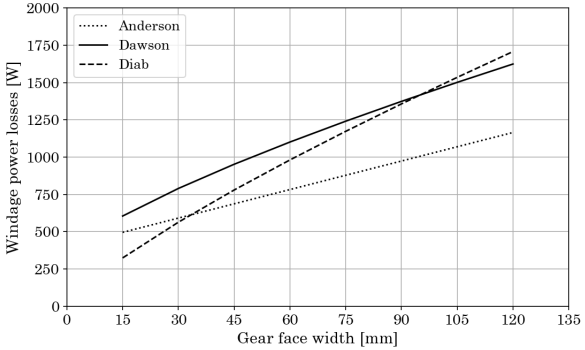

Figure 2.4: Windage power losses for a spur gear varying the gear face width: comparison between the results obtained by the formulas of Anderson and Loewenthal, Dawson, Diab at 5000 rpm.

meshing do not significantly impact total windage loss, which remains nearly equal to the sum of each gear's individual loss when not engaged.

Massini and Fondelli [22] investigated the effect of pressure on windage losses for a single gear and a pair of meshing gears. They housed a single spur gear in a sealed test chamber and reduced the pressure to simulate

aircraft engine conditions. Experiments were performed by varying the rotational speed to reach a maximum pitch velocity of 100 m/s. The results show good agreement with literature data available only at ambient pressure. Tests at lower pressures revealed a significant decrease in power losses. The data were successfully correlated using the dimensionless moment coefficient, C_m. In a related study, the same authors conducted an experimental investigation of windage losses in an unlubricated single spur gear. Using particle image velocimetry (PIV), they measured the flow field generated by the gear under ambient conditions across two measurement planes. This provided the first detailed, PIV-based visualization of flow structures around high-speed gears.

2.2.2 Bevel gear

There is little literature available on the windage of spiral bevel gears. The study conducted by Winfree [23] provided a large amount of experimental data on the windage loss of spiral bevel gears. Winfree thoroughly examined the effects of the shroud on a single spiral bevel gear. Winfree's experimental investigation compared different shrouding configurations. The results showed that the shroud significantly reduces windage power loss in high-speed spiral bevel gears. A series of design guidelines to minimize windage loss in gear systems was also proposed. For example, gears operating at peripheral speeds above 51 m/s require shrouding. This recommendation is also confirmed in Reference [15]. Furthermore, the study demonstrated that the rotation direction of the spiral bevel gear does not affect the windage losses and also the shroud design. An important fluid dynamic observation from the research is that bevel gears pump fluid from the inside to the outside through the tooth of the gear. Consequently, closing the gears inlet end effectively reduces windage, churning, and overall power consumption.

Farrall et al. [24] performed steady-state, single-phase simulations of the flow around a shrouded bevel gear using ANSYS Fluent. However, contrary to the significant windage loss reductions reported in previous experimental studies [23], only a limited decrease was observed in this

study. The maximum reduction was about 11% for a 4 mm shroud–gear clearance compared to an open gear. This discrepancy was attributed to substantial differences in gear geometry and shroud design between the numerical study and the experimental configurations.

Johnson et al. [25] conducted an experimental study comparing shrouded and unshrouded configurations of a single bevel gear rotating in air. The authors concluded that the gear behaves similarly to a centrifugal fan. Based on this finding, they suggested applying principles from fan design to gear and shroud optimization to reduce windage losses. The shrouded gear exhibited significantly lower windage torque, with the unshrouded gear reaching only 40% of this value. This seemingly counterintuitive result highlights the importance of optimizing shroud geometry to minimize power loss.

Subsequently, Webb [26] investigated the influence of key gear size parameters, including inner and outer diameter, cone angle, and module (number of teeth), on windage losses. In air-only conditions, increasing the cone angle and number of teeth or decreasing the outer diameter was found to reduce windage. However, the effect of the inner diameter proved to be more complex due to gear-shroud interactions. It was significantly less influential than the outer diameter; windage scaled with the latter to a power of approximately 4.3.

Zhu et al. [27] developed a quasi-analytical model to predict windage power losses in spiral bevel gears, which is particularly relevant for high-speed aerospace applications (above 90–120 m/s). The model decomposes total windage losses into three contributions: toe, heel, and gear teeth. The airflow in the lateral regions is modeled using the Navier–Stokes equations for a Newtonian fluid. The tooth-related losses are evaluated based on the Akin and Ville assumption [19, 28] , which states that the airflow impinging on a tooth is deflected by the preceding tooth in the direction of rotation. The model was validated using experimental data from Ruzek and Johnson [21, 25], showing an average discrepancy of less than 8%. The results indicate that over 90% of windage losses originate from gear teeth and that introducing a shroud can reduce losses by up

to 70%. Additionally, the study emphasizes the substantial impact of pitch cone and spiral angles, noting that larger angles facilitate smoother airflow and reduce windage losses.

Afterwards, Zhu et al.[29] improved upon their previous analytical formulation by combining an advanced, physics-based theoretical model with an innovative, CFD-based methodology using overset meshes. The enhanced analytical model separates windage losses into two main categories: peripheral losses, which distinguish between the primary flow near the tooth tip and the secondary flow near the tooth root, and toe/heel losses, which consider both the laminar and turbulent regimes through boundary-layer theory. Primary flow losses are evaluated by accounting for the air-pumping effect within the inter-tooth cavities. Secondary flow is modeled using the Stokes assumption for creeping flow.

The CFD approach using overset meshes allows for the simulation of gear rotation with overlapping grids instead of conformal meshes, which significantly reduces computational effort for complex geometries. Results demonstrate that pressure effects dominate total windage losses, accounting for over 90% of the overall contribution, especially at high rotational speeds. The primary inter-tooth flow is the main loss mechanism. Validation against Johnson's experimental data shows a maximum deviation of less than 10%, confirming the model's accuracy for incompressible subsonic flows (Mach number less than 0.3). Overall, this study shows that the analytical and CFD approaches can effectively estimate windage power losses in spiral bevel gears rapidly and reliably.

2.3 Churning Losses

Splash lubrication is the most common and cost-effective method of ensuring lubricant circulation in a transmission gearbox. It is used when the peripheral speeds of the components immersed in the oil bath are moderate, such as in industrial gear reducers, wind turbines, automotive gearboxes, and intermediate and rear helicopter gearboxes. The principle of splash lubrication is relatively simple. It takes advantage of the rotation

of the gearbox's mechanical components, particularly the gears, to set the lubricant in motion. Since the system is confined within the transmission housing, the design of the casing and the moving parts can be arranged to direct or channel oil splashes toward areas that need lubrication if they do not reach all the contact points.

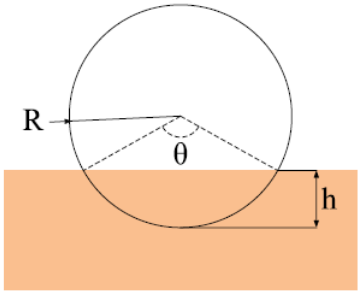

Figure 2.5: Schematic of the geometric parameters of an oil-bath lubricated gear.

The oil immersion level is defined as the ratio of the immersion depth of the rotating component in the oil bath to its radius: h/R (Figure 2.5). This dimensionless height is a first-order parameter that influences power losses. During the design of a transmission gearbox, the gear immersion depth and, more generally, the oil volume are determined in the final stage of the process. This parameter is primarily used to reduce churning losses. Therefore, a balance must be found between reducing losses and ensuring sufficient lubrication and cooling of the components. In helicopters, this relative immersion depth is typically within the range $h/R = 0.02$ to $h/R = 0.40$ [30]. Unlike the windage phenomenon, the churning phenomenon is complex because it involves two phases—generally air and oil—separated by a free surface.

2.3.1 Flow regimes

In 1975, Terekhov [31] conducted an extensive experimental campaign in which he measured the churning torque of spur gears with modules ranging from 2 to 8 mm. The oils used had high viscosities ($20 < \nu < 2000\ mm^2/s$) and the rotational speeds were moderate. Terekhov observed that the drag torque depended on the nature of the flow regime in the oil bath. Three flow regimes were identified and separated by the Reynolds number: laminar, transitional, and turbulent. The Reynolds number describes the relative importance of inertial effects compared to viscous effects. In the laminar regime, characterized by low Reynolds numbers, viscous effects dominate inertial effects. In contrast, the turbulent regime, characterized by high Reynolds numbers, is dominated by inertial effects. For example, Terekhov found that, in the laminar regime, the churning torque varies as the viscosity is raised to the power of 0.6. In the turbulent regime, however, the torque varies as the viscosity is raised to the reduced power of 0.3. Later, in 2011, Changenet et al. [32] continued to focus on the churning of spur gears, which made it possible to explore higher Reynolds numbers. They achieved this by using lower-viscosity oils ($8 < \nu < 150\ mm^2/s$) and higher speeds ($V_T = 58\ m/s$) than in Terekhov's experiments. Above a sufficiently high Reynolds number ($Re_c > 4000$), it was observed that the oil viscosity no longer influences the churning torque.

These investigations demonstrate that the flow regime in the oil bath is an important parameter for characterizing churning torque. Depending on the flow regime, different physical phenomena are involved, leading to more or less significant dependence on certain physical quantities, such as oil viscosity.

2.3.2 Influence of gear tooth geometry

Previous studies show that only the external dimensions of gears, such as diameter and width, have a first-order influence on churning losses. Indeed, in 1975, Terekhov [31] concluded from his experiments that the

tooth module has practically no effect on losses. In 2011, Changenet et al. [32] measured the resisting torque of eight spur gears with modules between 1.5 and 5 mm and of a rotating disk. They experimentally observed that a cylindrical disk with the same external dimensions (i.e., diameter and width) as a cylindrical gear produces similar losses. Furthermore, in 2017, Laruelle et al. [33] measured the resisting torque of four spiral bevel gears with a module of approximately $m \approx 3\ mm$ and of two equivalent smooth cones. The oils used had medium viscosity values ($35 < \nu < 220\ mm^2/s$) and the speeds were moderate ($V_T = 20\ m/s$). They observed the same phenomenon on hypoid gears, i.e., the external diameter has a first-order effect on losses, whereas the module and the number of teeth have a second-order influence.

These results contrast with those of Polly et al. [34]. They conducted a measurement campaign of the churning resistance torque of spur and helical gears, both with a module of 2.7 mm. They also used an equivalent gear without teeth composed of two smooth disks. Moderate speeds ($V_T = 20\ m/s$) and controlled oil temperature were used to obtain different viscosity values ($7 < \nu < 30\ mm^2/s$). Depending on speed and immersion depth, they measured losses 10 to 50% higher for the gears than for the disk of identical diameter and width. The largest differences were observed at immersion depths of $h_{Rp} = 0.05$ and $h_{Rp} = 2$, i.e., in configurations closest to single-phase — air ventilation at $h_{Rp} = 0.05$ and oil ventilation at $h_{Rp} = 2$. These large differences in losses between toothed wheels and smooth disks are understandable for these immersion values. In the ventilation phenomenon, losses primarily come from pressure drag generated by the pressure difference across the tooth flanks. Hence, the teeth play a crucial role, as discussed in the previous section.

Recently, it has become possible to visualize the submerged part of the gear, which has improved understanding of the phenomena that occur when the teeth pass through the bath. Várhegyi and Kristóf [35] used distilled water to photograph the boundary layer of the submerged portion of a spur gear tooth in a bath. Air bubbles form in the inter-tooth space (Figure 2.6 a), and at a certain speed or higher, the inter-tooth

space remains completely filled with air as it passes through the bath (Figure 2.6 b). The free surface then forms an almost perfect cylinder and becomes impermeable to water. This observation confirms the hypothesis

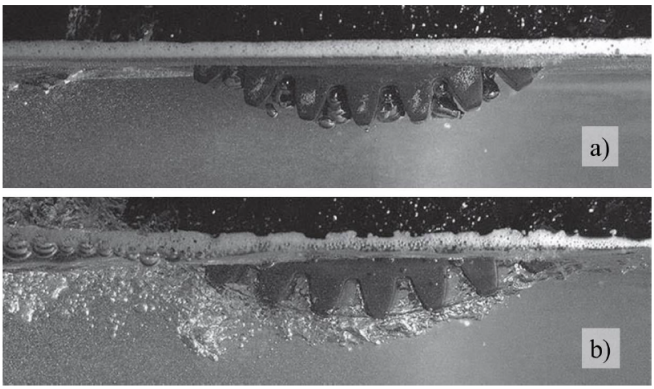

Figure 2.6: Photo of the submerged part of a straight cylindrical gear rotating in a bath of distilled water, clockwise rotation. $h_R = 0.20$, $\nu = 1$ *cSt, a)* $V_T = 0.5$ *m/s, b)* $V_T = 2.5$ *m/s [35].*

proposed by Luke and Olver [36] that the churning phenomenon could induce the formation of an air boundary layer between the moving gear and the oil bath at sufficiently high speeds. Furthermore, the presence of air pockets in the inter-tooth space could explain why the expelled oil flow rate decreases with rotational speed until reaching a constant value, as observed by Leprince et al. [37]. This evolution of the expelled flow rate may reflect the filling of the inter-tooth space by air pockets. This phenomenon has recently been reproduced in two-phase numerical simulations using the volume of fluid (VoF) method [38] and the smoothed-particle hydrodynamics (SPH) method [39]. Figure 2.7 shows an example of a cylindrical gear rotating in an oil bath, presenting the distribution of the oil fraction in the gear's symmetry plane. Chernoray and Jahanmiri [41] also visualized air trapped between the teeth of a pinion using a setup similar to that of the earlier authors, but with a transparent mineral

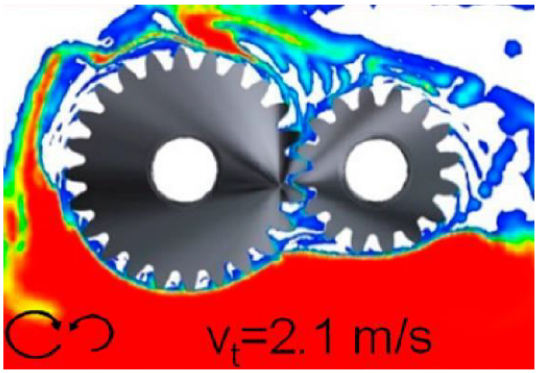

Figure 2.7: Simulated oil fraction by CFD in the symmetry plane of the gear. $V_T = 2.1$ *m/s,* $(h_R/)_1 = 0.10$ *and* $(h_R/)_2 = 0.40$*,* $\nu = 480$ *cSt [40].*

oil bath. They used a PIV system to measure the velocity field in the oil bath and established that the boundary layer thickness is the same for a cylindrical gear and a smooth cylinder with the same external dimensions. In summary, these studies demonstrate that under specific operating conditions, a cylindrical gear rotating in an oil bath exhibits the same behavior as an equivalent smooth disk. Therefore, for the range of operating conditions in which this air-trapping phenomenon between the teeth occurs, the geometric parameters to be considered in churning loss models for cylindrical gears can apparently be reduced to the external dimensions of a disk — namely, diameter and width.

Influence of Speed

In general, non-load losses increase with speed. Regarding the churning phenomenon, the loss varies with speed to a power between 1.47 and 2, depending on the flow regime and on average [32, 36, 42–44]. However, this sensitivity to speed is lower than in the case of ventilation, where losses vary with speed to a power between 2.8 and 3. At increasing rotational speeds, the dominant loss mechanism may also shift from churning towards

windage, depending on the operating conditions and immersion level [3, 30]. Recent investigations have characterized these transition regimes based on the physical mechanisms governing the interaction between the gear and the surrounding fluid [3].

Influence of Immersion Depth

All studies highlight an increase in churning losses as immersion depth increases [31, 32, 43–45]. Therefore, it is important to correctly estimate the immersion depth in order to predict losses. Since the immersion depth can vary as the moving parts rotate, two depths are considered: static and dynamic. The static immersion depth, or the depth without rotation of the moving parts, can be estimated directly from the volume of oil introduced into the gearbox and its internal geometric dimensions. In contrast, the dynamic immersion depth depends on the oil bath's dynamic deformations, which may result from inertia and gravitational effects. While the dynamic immersion depth fluctuates temporally and spatially along the moving part, it is common practice to use a constant, mean immersion depth because an average loss value is expected. Recently, studies on cylindrical and spiral bevel gears have focused on the dynamic deformation of the oil bath and its influence on the resisting torque [33, 34, 43, 46]. Relevant parameters include the presence of a pinion, the pinion's position relative to the oil bath, the rotation direction (Figure 2.8) and the casing's shape (Figure 2.9).

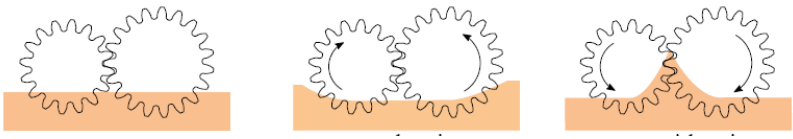

Figure 2.8: Effect of gear rotation direction on oil bath deformation.

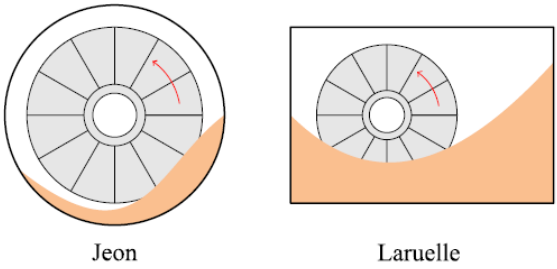

Figure 2.9: Effect of housing shape on the deformation of the oil bath: comparison between the experiments of Jeon and Laruelle et al.[33, 43].

Influence of Oil Aeration, Surface Tension and oil viscosity

When estimating churning losses, lubricants are commonly characterized by two physical properties: density and viscosity. However, other properties may also contribute to loss generation. Air can be present in the oil bath in several forms: air bubbles, air pockets trapped in the inter-tooth space (Figure 2.6), and foam on the surface of the oil bath. Air bubbles may form when the gear teeth enter the oil bath (Figure 2.6) or when the oil jet projected by the teeth falls back into the bath. All of these forms represent sources of oil contamination that may be detrimental to the transmission system [47]. The associated problems include:

- degradation of the thermal properties of the oil bath;
- oxidation of the oil;
- an increase in churning losses.

The rate at which oil aerates depends on the balance between the rate at which air bubbles are generated and the oil's ability to release these bubbles at its surface. The aeration level is defined physically as the volumetric fraction of air within a given volume of oil. It is particularly challenging to estimate this parameter because it is influenced by operating

conditions, such as velocity, immersion depth, and oil temperature, as well as the oil's physical properties. According to Leprince et al. [48], parameters such as the dipole moment, air solubility in oil, and surface tension significantly impact aeration. Their study showed that, when the aeration level exceeds 10%, additional losses caused by bubble breakup become significant, with churning losses increasing by up to a factor of 1.6. Subsequently, Kolekar et al. [49] confirmed the influence of surface tension on churning losses, reporting a 28% increase in losses corresponding to a 16% rise in surface tension.

In conclusion, not all of the physico-chemical properties that influence the aeration phenomenon have been fully identified. Therefore, it is likely that the additives present in the oil also play a role. The main recognized factors promoting aeration are the oil bath temperature and level of agitation, characterized by parameters such as rotational speed and gear immersion depth. For helicopter transmission gearboxes, the relatively low immersion depths typically encountered in these applications may limit the occurrence of significant aeration effects.

With regard to the physical properties of the oil, there are different perspectives regarding the effect of lubricant viscosity on no-load gear losses. According to Terekhov (1975) [31], gear churning losses increase as lubricant viscosity rises, particularly when high-viscosity oils are used. Similarly, Michaelis and Winter (1994) [50] observed a consistent increase in churning losses with higher lubricant viscosity, regardless of oil type, even at relatively low operating viscosities. Under certain operating conditions, reducing the viscosity grade — for instance, from ISO VG 150 to VG 100 — can lead to a decrease in no-load power losses of approximately 10%. However, systematic studies by Mauz (1987) [51] revealed a more complex relationship. At low rotational speeds, churning losses increase with viscosity. At higher speeds, however, they decrease (see Figure 2.10). This behavior is attributed to the reduced volume of oil set in motion at higher viscosities, resulting in lower energy dissipation.

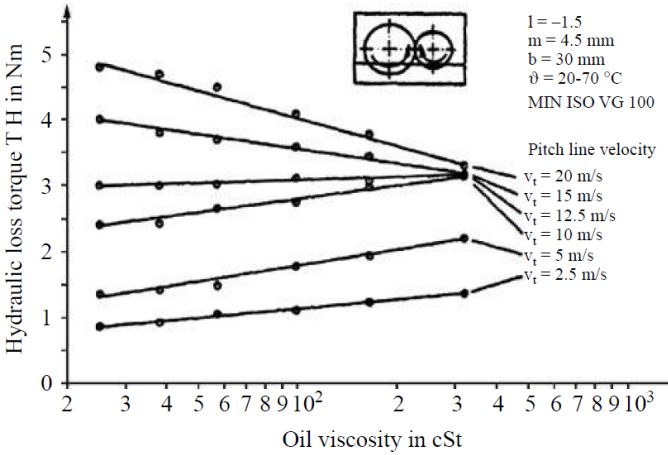

Figure 2.10: Influence of oil viscosity on gear churning losses [51].

2.3.3 Influence of wall clearance

Experimental studies on rotating wheels immersed in an oil bath [18, 52] have shown that deflectors have little effect on the resisting torque. In contrast, end plates can significantly reduce the resisting torque. Indeed, end plates help to mitigate the suction effect, thereby decreasing the amount of fluid projected by the gear teeth. Neurouth [53] proposes a criterion for selecting the axial distance between the gear and the end plates. He observes that oil aeration decreases as the axial clearance is reduced, which in turn reduces churning losses. Across all his experiments, he notes that the dimensionless torque coefficient remains low if $\Gamma > 10$, where:

$$\Gamma = \frac{\omega R_p^2}{\nu g\, h\, J_a^2} \tag{2.20}$$

where Γ is a dimensionless parameter, ν is the kinematic viscosity of the oil, g is the gravitational acceleration, h is the immersion depth in the oil bath, and J_a is the axial clearance between the gear flanks and the end plates.

Oil Squeezing Phenomenon

Depending on the gear's rotation direction, oil can be thrown outward or inward (see Figure 2.8). The preferred rotation direction is that which delivers more oil to the tooth contact. This rotation direction generates higher losses for two reasons: (i) Oil becomes trapped between the teeth during meshing, resulting in squeezing losses [34, 46]. (ii) The pinion and gear splash oil onto each other, which increases their immersed surface area and, consequently, their individual churning losses [52].

In the case of a bevel gear pair, Jeon [43] measured churning losses 2.5 to 3.5 times higher than those of the gear alone when a meshing pinion was added. The pinion is positioned above the oil bath level and is therefore not immersed when the gearbox is stationary. These additional losses are attributed to the onset of trapping losses, i.e., the losses associated with the compression and displacement of oil trapped between the meshing gear teeth, as well as to the increased immersed surface area when the gearbox is operating. Trapping losses are not investigated in this study because they are assumed to be negligible due to the limited oil volume in helicopter gearboxes.

2.4 Presentation of Models Based on Different Approaches

2.4.1 Models Based on Experimental Approaches

Numerous experimental studies have been conducted historically to quantify churning losses. Several empirical formulas have been proposed for cylindrical gears. The formula by Changenet et al. [32] consolidates the various aspects previously discussed. As such, this model has served as the basis for developing loss formulas for bevel gears. These formulas are detailed in the following section.

2.4.2 Changenet et al. Model

As previously discussed, the work of Changenet et al. [32] covered a wide range of operating conditions for cylindrical gears rotating in an oil bath. The proposed loss formula follows the drag-loss form, first used by Boness [54] for rotating gears in an oil bath. The dimensionless churning torque formulation is analogous to that of Terekhov [31], and it is expressed across four different flow regimes. The Changenet et al. churning model is valid for both spur and helical cylindrical gears.

$$P_{\mathrm{Ch}} = \frac{1}{2}\rho\, h_{\mathrm{oil}}\, S_m\, R_p^3\, \omega^3\, C_{m,Ch} \tag{2.21}$$

with

$$S_m = R_p^2(\theta - \sin\theta) + R_p\,\theta b + \frac{2H_{\mathrm{dent}}\, b\, Z\cos(\alpha)\cos(\beta)\,\theta^2}{\pi} \tag{2.22}$$

and

$$\theta = 2\cos^{-1}\left(\frac{R_p - h}{R_p}\right) \tag{2.23}$$

where θ is the immersion angle as defined in Figure 2.5.

A new parameter, γ, in addition to the Reynolds number, has been defined to highlight two new flow regimes associated with centrifugal effects.

$$\gamma = \omega^2 (R_p\, b\, m)^{1/3} \tag{2.24}$$

$$Re_c = \frac{\omega R_p b}{\nu} \tag{2.25}$$

where Re_c is the critical Reynolds number. The dimensionless churning torque coefficient $C_{m,Ch}$ is given by:

If $\gamma < 750\,\mathrm{m}^2/\mathrm{s}$ and $Re_c < 4000$

$$C_{m,Ch} = 0.812\left(\frac{h}{R_p}\right)^{0.45}\left(\frac{V_0}{R_p^3}\right)^{0.1} Fr^{-0.6} Re_c^{-0.21}\left(\frac{b}{R_p}\right)^{0.21} \tag{2.26}$$

If $\gamma < 750\,\mathrm{m}^2/\mathrm{s}$ and $Re_c > 4000$

$$C_{m,Ch} = 0.142\left(\frac{h}{R_p}\right)^{0.45}\left(\frac{V_0}{R_p^3}\right)^{0.1} Fr^{-0.6}\left(\frac{b}{R_p}\right)^{0.21} \tag{2.27}$$

If $\gamma > 1250\,\mathrm{m}^2/\mathrm{s}$ and $Re_c < 4000$

$$C_{m,Ch} = 22.29\left(\frac{h}{R_p}\right)^{0.1}\left(\frac{V_0}{R_p^3}\right)^{-0.35} Fr^{-0.88} Re_c^{-0.21}\left(\frac{b}{R_p}\right)^{0.85} \tag{2.28}$$

If $\gamma > 1250\,\mathrm{m}^2/\mathrm{s}$ and $Re_c > 4000$

$$C_{m,Ch} = 3.906\left(\frac{h}{R_p}\right)^{0.1}\left(\frac{V_0}{R_p^3}\right)^{-0.35} Fr^{-0.88}\left(\frac{b}{R_p}\right)^{0.85} \tag{2.29}$$

where V_0 is the oil volume, and the Froude number Fr is defined as:

$$Fr = \frac{\omega^2 R_p}{g} \tag{2.30}$$

These expressions for the dimensionless churning torque highlight the influence of viscous forces through the Reynolds number. In the turbulent regime ($Re_c > 4000$), where viscous forces become negligible, the Reynolds number no longer appears in the expression for the dimensionless torque. It can be noted that for low centrifugal accelerations ($\gamma < 750\,\mathrm{m}^2/\mathrm{s}$), the immersion depth and the gear diameter have a significant impact on the loss. For high centrifugal accelerations ($\gamma > 1250\,\mathrm{m}^2/\mathrm{s}$), the gear width becomes a dominant parameter affecting churning losses.

2.4.3 Models Based on Analytical Approaches

In addition to the aforementioned experimental studies, other authors have developed analytical relations to quantify churning losses. For example, Seetharaman and Kahraman [55] reduced the Navier–Stokes equations to a simple formula to calculate the resisting torque of a gear train partially immersed in an oil bath. In this framework, churning losses result directly from viscous shear stress and are proportional to oil viscosity. However, as previously noted, the influence of viscous effects

can vary depending on the flow regime in the oil bath. For instance, losses in a water bath can be much higher than in a more viscous oil bath [36, 48, 49]. Consequently, Seetharaman and Kahraman's approach, which includes viscosity in the formulation, is only applicable to flow regimes with moderate Reynolds numbers.

2.5 Loss models for bevel gears

2.5.1 Jeon Model

Jeon [43] measured the resisting torque of gears with pitch diameters of 213 mm and 222 mm in an automotive differential, varying the peripheral speed up to 23 m/s. The experiments were conducted using both mineral and synthetic oils with kinematic viscosities ranging from 30 cSt to 280 cSt, and for relative immersions between 0.3 and 0.8 times the pitch radius. He adopted the churning loss formula from the Changenet model (Eq. 2.21) and modified it as follows:

$$P_{Ch} = \frac{1}{2}\rho\, h_{\text{oil}}\, S_m\, R_p^2 b\, \omega^3\, C_m \tag{2.31}$$

with

$$C_m = 2.185\left(\frac{h}{R_p}\right)^{0.15}\left(\frac{V_0}{R_p^3}\right)^{-0.2} Re^{-0.25} Fr^{-0.53} \tag{2.32}$$

It should be noted that his dimensionless drag coefficient formula does not vary with the flow regime. In this model, viscous forces are present in all flow regimes and are represented by the Reynolds number raised to the power of -0.25. However, Jeon [43] also showed that the Reynolds number exponent varies with rotational speed, becoming less negative with increasing speed. This exponent was calculated using torque data from two churning tests conducted with identical parameters except the oil viscosity. This allowed the effect of Reynolds number to be isolated

and calculated using the formula:

$$A = \frac{ln(Cm_1/Cm_2)}{ln(Re_1/Re_2)} = \frac{ln(Cm_1/Cm_2)}{ln(\nu_2/\nu_1)} \tag{2.33}$$

Where A is the Reynolds number exponent and the subscripts 1 and 2 indicated two different set of test data. The calculated exponents showed that below a certain value of rotational speed a constant exponent value of approximately -0.25 may be used while at high speeds the effect of Reynolds approaches zero.

2.5.2 Laruelle and Fossier Model

Jeon's work was recently extended by Laruelle et al. [33], who highlighted the influence of gear geometry and different flow regimes in the oil bath. Their measurements on various bevel gear geometries, up to peripheral speeds of 20 m/s, allowed adapting the churning loss formula (Eq. 2.31) to give a higher contribution to the gear diameter rather than its width:

$$P_{Ch} = \frac{1}{2}\rho\, h_{\text{oil}}\, S_m\, R_0^3\, \omega^3\, C_{m,Ch} \tag{2.34}$$

where S_m is the wetted surface of the equivalent cone, with the calculation formula detailed in Appendix A.

They also highlighted the presence of two flow regimes separated by the Reynolds number. This phenomenon is similar to that observed for cylindrical gears. In fact as described previously, the Reynolds dependences above a certain rotational speed is ignored in this correlation consistent with Jeon's. Here, the Reynolds and Froude numbers are defined using the outer radii rather than the pitch radii.

For $Re \leq 20000$:

$$C_m = 1.45\left(\frac{h}{R_0}\right)^{0.15}\left(\frac{V_0}{R_0^3}\right)^{-0.2} Re^{-0.25} Fr^{-0.53} \tag{2.35}$$

For $Re > 20000$:

$$C_m = 0.12\left(\frac{h}{R_0}\right)^{0.15}\left(\frac{V_0}{R_0^3}\right)^{-0.2} Fr^{-0.53} \tag{2.36}$$

with

$$Re = \frac{\omega R_0^2}{\nu} \tag{2.37}$$

$$Fr = \frac{\omega^2 R_0}{g} \tag{2.38}$$

2.5.3 Quiban et al.

This literature review reveals that, while there are extensive studies on cylindrical gears, there is limited data on the churning losses generated by bevel gears. Additionally, the models presented here differ in their approaches and formulations.

Quiban et al. [10] propose a model in their work to predict no-load power losses due to churning effects. This model accounts for lubricant behavior and gear operating conditions. This study experimentally investigated the no-load losses of several splash-lubricated spiral bevel gears using a dedicated test rig. Pitch line velocities reached up to 60 m/s. The authors analyzed the variation in gear immersion depth, finding that it correlates with the Froude number. Based on these findings, a new analytical formulation was developed to predict no-load losses, combining both churning and windage contributions. The proposed model incorporates key influencing factors, including rotational speed, immersion depth, lubricant properties, and gear geometric characteristics.

According to previous works [45] the P_{Ch} can be expressed as a dynamic pressure of reference and a wetted surface, see Eq. 2.34. Equally, the windange power losses P_{wi} can be expressed as the dynamic pressure and a related surface area as:

$$P_{wi} = \frac{1}{2}\rho_{\text{air}}\left(S - S_m\right) R_0^3\, \omega^3\, C_{m,wi} \tag{2.39}$$

To obtain:

$$P_{tot} = P_{Ch} + P_{wi} = \frac{1}{2}\rho_{\text{oil}}\, h\, S_m\, R_0^3\, \omega^3\, C_{m,Ch} + \frac{1}{2}\rho_{\text{air}}\, (S - S_m)\, R_0^3\, \omega^3\, C_{m,wi} \tag{2.40}$$

Based on the studies by Laruelle and Fossier [33], the dimensionless formulation of the churning drag torque can be expressed as in Eq. 2.35 and 2.36. A few experimental tests were conducted to determine the dimensionless windage drag torque. It appeared that the expression of the dimensionless drag torque that gave the closest results to the experimental ones was:

$$C_{m,wi} = K\delta^{-1} \tag{2.41}$$

where K is a constant and δ is the gear face angle (rad).

In the study of Quiban et al. [10], a particular trend in drag torque was observed: as rotational speed increased, torque first rose to a local maximum, then decreased to a local minimum, and finally increased again at higher speeds. Since torque depends on immersion depth, the observed reduction can be interpreted as a consequence of a local decrease in immersion level. This minimum appears because the effective immersion depth decreases with increasing rotational speed thus lowering the churning losses. At even higher speeds, torque losses increase again as windage losses become dominant respect churning losses. A series of torque measurements was conducted under various operating conditions (different oil levels, type of oils, rotational speed) to describe the dynamic evolution of oil immersion. The rotational speed at which the local maxima occurs, is strongly dependent on the static immersion level and relatively insensitive to the type of oil. A new model of relative immersion evolution based on a modified Froude number Fr^* to account for the effect of free surface flows: below a critical number of Fr^* the correlation uses the static immersion depth otherwise a dynamic formulation is used, see Eq. 2.42.

$$\left(\frac{h}{R_0}\right)_{dyn} = \frac{\left(\frac{h}{R_0}\right)_{stat}}{-7.88\left(\frac{h}{R_0}\right)_{stat} + 6.51} \tag{2.42}$$

2.6 Phase Lock Average

As stated in Section 1.4, PIV was used to measure the oil projected by the gear above the bath, a highly unsteady phenomenon influenced by the oscillations of the oil bath caused by the gear rotations. This phenomenon does, however, contain a periodic component determined by the gear's tooth-passing frequency. A more robust representation of the oil flow field above the bath may be obtained by using post-processing methods that isolate this periodic component. In this, and the following subsections of this chapter, the methods used to obtain such representation are presented in detail.

The phase-locked average (PLA) is a post-processing technique that, once a frequency of interest has been identified, allows for the extraction of coherent structures occurring at that specific frequency for different physical quantities under investigation. With this extraction, PLA allows to separate, and to clearly identify, the coherent part of the flow field from the purely stochastic, turbulent part. This technique has been used successfully in many studies that involve the analysis of quasi-periodic turbulent and even reactive flows, with the PLA applied to visualize quantities such as velocity, mixture fraction, heat release rate, etc. The basis of this method lies in the observation that the oscillations of a generic quantity, ψ, can be described through a triple decomposition introduced by Hussain and Reynolds [56]:

$$\psi(\vec{x},t) = \overline{\psi}(\vec{x}) + \psi_c(\vec{x},t) + \psi_t(\vec{x},t), \tag{2.43}$$

Where $\overline{\psi}(\vec{x})$ represents the time-averaged component, $\psi_c(\vec{x},t)$ denotes the coherent contribution associated with periodic fluctuations of the analyzed quantity, and $\psi_t(\vec{x},t)$ represents the stochastic component associated with turbulent fluctuations. The coherent component, denoted by the symbol ψ_c, is characterized by a tonal spectrum. In contrast, the stochastic component, denoted by the symbol ψ_t, exhibits a broadband spectrum consistent with the energy cascade mechanism typical of turbulent flows. The Phase-Locked Average aims to isolate the signal component whose

frequency content is dominated by a single frequency corresponding to the selected phase-locking frequency. In other words, the method aims to extract the coherent contribution associated with this specific oscillatory mode. The traditional PLA procedure is carried out in the following steps to achieve this objective:

1. First, the frequency of interest, f_{PLA}, at which the phenomenon is to be analyzed, is identified.

2. The corresponding period is then computed as follows:

$$T_{\mathrm{PLA}} = \frac{1}{f_{\mathrm{PLA}}}. \tag{2.44}$$

3. The period T_{PLA} is divided into n subintervals, each of which is associated with a specific phase angle.

4. Instantaneous snapshots of the system, obtained either from experimental measurements or by numerical simulations, are assigned to the corresponding phase interval. The average associated with each phase bin is then calculated.

This procedure requires the capability to calculate the phase of the single snapshots within the period of interest. This is typically achieved through the use of an external signal which tracks the frequency of the studied phenomenon. For example Giezendanner et al. [57] studied periodic combustion instabilities in a swirl burner using planar laser-induced fluorescence and organized the single measurements within the phase of the self-excited pressure oscillations using a trigger signal derived from a microphone. Canepa et al.[58] used the signal from an optical encoder to calculate the phase corresponding to individual PIV velocity fields in a low pressure turbine cascade wind tunnel in which wakes from the up-stream blade row was simulated by a system of rotated bars that periodically passed in front of the test section. Perrin et al. [59] obtained phase average quantitates from PIV measurements and detached eddy simulations of vortex shedding downstream of a circular cylinder in

cross-flow by using the wall pressure signal on the cylinder as a trigger signal.

As the result of this procedure, the number of phase averages obtained equals the number of sub-intervals into which the period has been divided. These fields represent averages in which contributions from frequencies different from the selected one are largely filtered out. Therefore, PLA provides a way to isolate coherent structures associated with the chosen frequency. From a physical standpoint, the PLA yields n phase-averaged fields, each of which corresponds to one of the n sub-periods into which the fundamental period associated with the selected frequency has been divided. Therefore, the i-th phase average can be interpreted as the coherent structure associated with the chosen frequency at a specific phase of the oscillation cycle. Combining the n phase-averaged fields allows one to reconstruct the temporal evolution of that structure over a complete oscillation period. PLA is commonly used to analyze self-excited phenomena where the flow exhibits well-defined, periodic dynamics. The main limit of the traditional PLA procedure described above is the requirement of the external trigger signal to calculate the phase of the single snapshots. To overcome this limitation, in the case such signal is not available, it is possible to use a special property of the Proper Orthogonal Decomposition (POD), described in the following section.

2.7 Proper Orthogonal Decomposition

This section presents the fundamental principles underlying the velocity field analysis conducted in this work. The advanced data-driven technique called Proper Orthogonal Decomposition (POD) is explained here. POD is a valuable tool for extracting maximum information from extensive datasets, especially for identifying coherent structures within turbulent flows. These structures are often complex and provide valuable insight into their interactions and contributions to specific phenomena.

Data-driven modal analysis (DDMA) is a data processing technique that decomposes a data set into a linear combination of modes $M_j(x_i, t_k)$,

which are characterized by their temporal structures depending on the values assumed by the modes at point x_i during different temporal instants and by their spatial structures depending on the values assumed by the modes at instant t_k in different spatial points, as shown in Figure 2.11. The DDMA has several applications:

- *pattern recognition*: The proper spatial distribution of a mode is strongly associated with the coherent structures that characterize turbulent flows and are present in the dataset under examination. Therefore, DDMA can identify the coherent structures populating a turbulent flow using data collected through experimental analyses (e.g., PIV) or CFD simulations. For this reason, DDMA is a useful post-processing technique for experimental activities and CFD analyses;

- *filtering/data compression*: When working with large datasets, it may be necessary to filter or compress the data by eliminating modes of low importance associated with background noise, reflections, and other unwanted elements. This type of data processing is commonly used in CFD simulations and PIV analyses;

- *model order reduction (Reduced Order Model, ROM)*: to analyze a system's overall dynamics, Direct Discretization and Modal Analysis (DDMA) can be used to obtain a simplified representation by considering only the leading modes. These modes are then used to construct a reduced basis onto which the original problem is projected. This significantly reduces the complexity of the problem and the required computational effort.

Looking at Figure 2.11, the data matrix $D(x_i, t_k) = D[i,k] \in \mathbb{R}^{n_s \times n_t}$ to be decomposed, associated to the complete dataset, can be generally assumed as:

$$D(x_i, t_k) = \begin{bmatrix} d_1[1] & \cdots & d_k[1] & \cdots & d_{n_t}[1] \\ \vdots & \vdots & \vdots & \vdots & \vdots \\ d_1[n_s] & \cdots & d_k[n_s] & \cdots & d_{n_t}[n_s] \end{bmatrix} \tag{2.45}$$

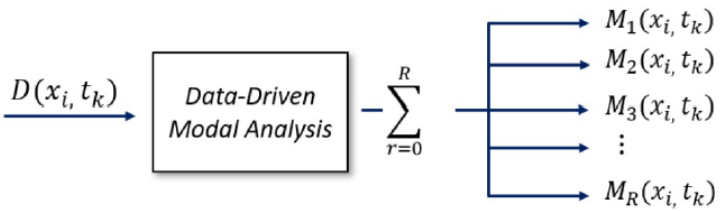

Figure 2.11: Schematic representation of data-driven modal analysis.

where n_s is the number of points in the spatial domain where the data are sampled (in a CFD simulation, these coincide with the mesh nodes), and n_t is the number of snapshots selected for use. Assuming $n_s \gg n_t$, as is common in CFD and experimental applications, the goal of DDMA is to decompose the dataset into n_t modes. The data matrix is typically created by recording the spatial and temporal evolution of one or more quantities. In CFD applications, each "snapshot" may correspond to a plane within the computational domain and is arranged as a column of the matrix. Consequently, the spatial distribution can be obtained by examining the columns, while the temporal evolution is represented along the rows. After normalization, the matrix can be analyzed from two equivalent perspectives, the temporal view:

$$D(x_i, t_k) = \sum_{r=1}^{R} C_r[i]\psi_r[k] = \sum_{r=1}^{R} \sigma_r \phi_r[i]\psi_r[k] \tag{2.46}$$

And the spatial one:

$$D(x_i, t_k) = \sum_{r=1}^{R} C_r[k]\phi_r[i] = \sum_{r=1}^{R} \sigma_r \psi_r[k]\phi_r[i] \tag{2.47}$$

Where:

- σ_r are the eigenvalues of the data correlation matrix, which will be introduced later, represent the energy content of each mode. They indicate the mode's weight in reproducing the system's overall

dynamics and effectively represent its amplitude.

- ψ_r are the eigenvectors of the data correlation matrix and provide information about the temporal evolution of each mode. Performing a Fourier transform (FFT) on these eigenvectors allows one to determine the frequency content associated with each POD mode.

- ϕ_r is the space distribution of each POD mode. They provide useful information about the coherent structures that characterize the turbulent flow.

From a temporal perspective, each snapshot can be represented as a linear combination of the temporal bases ψ_r, with coefficients c_r that vary depending on the spatial location, associated with the corresponding spatial mode ϕ_r. Similarly, from a spatial perspective, each snapshot can be expressed as a linear combination of the spatial bases ϕ_r, with coefficients c_r that depend on the temporal instant, associated with the corresponding temporal mode ψ_r. Thus, if ϕ_r and ψ_r form orthogonal bases, they are coupled and not independent of each other. To simplify the analysis and directly associate σ_r with the amplitude of the POD mode, the temporal and spatial bases are often normalized to unit length ($\|\psi_r\| = \|\phi_r\| = 1$). With this normalization, can be obtained a matrix factorization of the form [60, 61]:

$$D = \sum^{R=rank(D)} \sigma_r \phi_r \psi_r^T \tag{2.48}$$

It is important to note that, assuming $n_s \gg n_t$, a data matrix with rank n_t is a full-rank matrix and therefore does not yield any approximation. Conversely, if the rank is chosen to be less than n_t, as is common practice in fluid mechanics applications, the reconstructed matrix will be an approximation of the original matrix. The POD acts on the initial data matrix via a three-matrix factorization that can be expressed more compactly as follows:

$$D = \Phi \Sigma \Psi^T \tag{2.49}$$

Where D is the initial data matrix, Φ is the matrix containing the spatial POD modes, and Σ is the matrix collecting the energy contribution associated with each mode. Finally, Ψ is the matrix of the temporal coefficients of the modes. The following structure characterizes the matrices, respectively:

$$\Phi = \begin{bmatrix} \phi_1[i] & \phi_2[i] & \cdots & \phi_R[i] \\ \vdots & \vdots & \vdots & \vdots \end{bmatrix} \tag{2.50}$$

$$\Sigma = \begin{bmatrix} \sigma_1 & 0 & 0 \\ 0 & \ddots & 0 \\ 0 & 0 & \sigma_R \end{bmatrix} \tag{2.51}$$

$$\Psi = \begin{bmatrix} \psi_1[k] & \psi_2[k] & \cdots & \psi_R[k] \\ \vdots & \vdots & \vdots & \vdots \end{bmatrix} \tag{2.52}$$

As previously mentioned, the matrices Φ and Ψ are composed of orthonormal column vectors and therefore form orthonormal bases ($\Psi^T = \Psi^{-1}$ and $\Phi^T = \Phi^{-1}$), while Σ is a diagonal matrix. Consequently, Φ and Ψ cannot be chosen independently, as they are uniquely determined by the decomposition of the matrix D. By considering a truncation of rank R, corresponding to the number of retained modes, a reconstructed matrix can be obtained that approximates the original matrix D, and can be written as follows:

$$\tilde{D} = \tilde{\Phi}\tilde{\Sigma}\tilde{\Psi}^T \tag{2.53}$$

Depending on the chosen decomposition method, the matrix Ψ can be derived in different ways. Assuming that this matrix is orthogonal yields the following relationship:

$$D(\Psi^T)^{-1} = \Phi\Sigma = C \tag{2.54}$$

When the columns of the product $\Phi\Sigma = C$ are normalized and the spatial basis vectors have unit length, the singular values, σ, can be determined

using the following expression:

$$\sigma_r = \|C_r\| = \|\phi_r \sigma_r\| \tag{2.55}$$

After inverting the matrix Σ, the matrix Φ can similarly be obtained using the following expression:

$$\Phi = D(\Psi^T)^{-1}\Sigma^{-1} \tag{2.56}$$

As previously mentioned, the matrix Ψ can be derived in different ways depending on the chosen decomposition method. One such method is the Proper Orthogonal Decomposition, also known as Principal Component Analysis (PCA), which is a data-driven modal analysis (DDMA) technique. Originally introduced by Lumley et al.[62], POD is now widely used in CFD applications. POD is an energy-based decomposition method that seeks to represent the original dataset as efficiently as possible by minimizing the approximation error when retaining only the first R modes. These R modes correspond to the largest energy contributions, ensuring that the captured energy is maximized. In this way, the dominant dynamics of the physical system under investigation are retained. Starting from the original data $D(x_i, t_k)$, a reduced subspace is reconstructed using an orthonormal basis. Accordingly, based on the decomposition, a rank-R approximation of the original dataset can be expressed as follows:

$$D = \Phi\Sigma\Psi^T \rightarrow \Phi = D\Psi\Sigma^{-1} \rightarrow D = D\Psi\Psi^T \rightarrow D = D\tilde{\Psi}\tilde{\Psi}^T \tag{2.57}$$

Where $\Psi \in \mathbb{R}^{n_t \times n_t}$ and $\tilde{\Psi} \in \mathbb{R}^{R \times n_t}$. Since Ψ is a unitary matrix, it forms an orthonormal basis of dimension $n_t \times n_t$, so that $\Psi\Psi^T = I$. Consequently, projecting the original data D using the full basis simply reproduces D itself. However, if only the first R columns of Ψ are retained, a reduced orthonormal basis $\tilde{\Psi}$ of dimensions $R \times n_t$ is obtained. The corresponding projection matrix $\tilde{\Psi}\tilde{\Psi}^T$ is no longer the identity, and its application to D yields a rank-R approximation $\tilde{D}$ of the original data. In the context of POD analysis, the temporal basis is selected to achieve an optimal representation, meaning that the chosen modes minimize the

approximation error between D and $\tilde{D}$. This optimization problem can be formulated and solved in two equivalent ways [63],so by minimizing the error:

$$min(\|D - \tilde{D}\|_2) = min(\|D - D\tilde{\Psi}_1\tilde{\Psi}_1^T\|_2) \tag{2.58}$$

Or, maximize the energy content:

$$max(\sigma_1) = max(\|\Phi_1\sigma_1\|_2) = max(\|D\tilde{\Psi}_1\|_2) \tag{2.59}$$

The process is constrained by requiring that the matrix defining the basis for projecting the data have orthonormal elements:

$$\langle\psi, \psi\rangle = \psi^T\psi = 1 \tag{2.60}$$

By formulating the problem to maximize the energy content as in Eq.2.59, the application of the Lagrange multipliers method requires the introduction of an auxiliary function $\mathcal{L}$, defined as follows:

$$\mathcal{L}(\tilde{\psi}, \lambda) = \{(D\psi)^T(D\psi)\} + \lambda\{1 - \psi^T\psi\} \tag{2.61}$$

where λ is the Lagrange multiplier, the first term represents the maximization object and the second one the constraint. To resolve the problem of constrained optimization, it is necessary to derive equation 2.61 and set it equal to zero:

$$\frac{\partial\mathcal{L}}{\partial\psi} = (D^TD)\psi - \lambda\psi = 0 \tag{2.62}$$

where D denotes the known starting data matrix and ψ represents the unknown vector to be determined. From Eq. 2.62, it is easily obtain:

$$(D^TD)\psi = \lambda\psi \tag{2.63}$$

This last expression is the most important part of the entire process, as it indicates how to determine the POD modes. Therefore, the problem is reduced to an eigenvalue problem. This shows that the optimal temporal basis corresponds to the eigenvectors of the matrix $K = D^TD$, which is commonly referred to as the temporal correlation matrix. The associated

eigenvalues are λ. The matrix K is referred to as the temporal correlation matrix because it contains the correlations among different snapshots. Therefore, the eigenvalue problem described above can be solved by determining the eigenvalues, λ, and the corresponding eigenvectors starting from Eq. 2.52. It is also important to note that an alternative POD method can be obtained by applying the same procedure described above, in which the spatial basis ϕ is computed first. As mentioned earlier, the POD decomposition (Eq. 2.49) is based on two assumptions:

- the matrices Ψ and Φ are assumed to be composed of orthonormal column vectors and therefore form two distinct orthonormal bases. This implies that they are unitary matrices ($\Psi^T = \Psi^{-1}$ and $\Phi^T = \Phi^{-1}$);

- the matrix Σ is assumed to be diagonal.

Examining the consequences of selecting these temporal structures as the basis for projecting the initial data is insightful. To this end, the generic factorization of matrix D (Eq.2.49) is used and substituted into the expression for matrix K:

$$K = D^T D = (\phi\Sigma\psi^T)^T(\phi\Sigma\psi^T) = \phi\Sigma\psi^T\phi\Sigma\psi^T \tag{2.64}$$

The symmetry of the matrix K ensures its diagonalizability. Since ψ represents the eigenvectors of the matrix, it is possible to express K as follows:

$$K = \psi\Lambda\psi^T \tag{2.65}$$

From Eq. 2.65 and 2.64, it is possible to obtain:

$$\Lambda = \Sigma\phi^T\phi\Sigma \tag{2.66}$$

Since Λ is a diagonal matrix by construction, being a matrix of eigenvalues, it follows that $\phi^{\mathrm{T}}\phi = 1$. Therefore, the following can be obtained

$$\Lambda = \Sigma^2 \tag{2.67}$$

In this way, previous assumptions have been demonstrated. As previously mentioned, Lumley introduced the POD procedure for CFD applications, focusing exclusively on the spatial distribution of the modes (spatial mode) [62]. In contrast, this work employs the Snapshot-POD method, introduced by Sirovich [64, 65], which accounts for the spatial and temporal evolution of the modes. This method is used since the condition $n_s \gg n_t$ holds, as is common in most CFD studies. The snapshot POD procedure has been implemented in MATLAB as follows:

- First, the matrix K is computed as follows:

$$K = D^T D$$

- Secondly, the decomposition of the K matrix is obtained through:

$$K = \Phi_P \Lambda_P \Psi_P^T$$

- Third, the spatial POD modes and their amplitude coefficients are computed as follows:

$$\Sigma_P = \sqrt{\Lambda_P}$$

$$\Phi_P = D \Psi_P \Sigma_P^{-1}$$

Proper orthogonal decomposition (POD) is used to characterize the coherent, large-scale, unsteady behavior of the system. One key application of POD is extracting the phase of individual events from asynchronously acquired datasets, which allows for the reconstruction of the phase-resolved cycle of the phenomenon of interest. In the case of gears, the phenomenon of interest is the passage of individual gear teeth or the associated dynamic response.

2.8 Phase Identification Based on Proper Orthogonal Decomposition

As previously described (see section 2.7), coherent structures are periodic phenomena, such as vortices, which are formed at specific frequencies depending on the nature of the flow field and can be distinguished from purely stochastic background turbulence. A notable feature of POD is that when it is applied to a flow field containing coherent structures, the temporal coefficients can capture information about the phase within the characteristic frequency of each coherent structure present in a given snapshot. This enables the snapshots to be ordered according to phase, allowing a phase-average analysis even when the original measurements are not time-resolved or synchronised. This approach has already been used in several studies focusing on the analysis of coherent structures. In the work of Van Oudheusden et al. [66] the vortex-shedding phase angles of individual velocity fields were extracted, which were acquired at asynchronous low rate with respect to the vortex shedding cycle. Perrin et al. [59] studied the flow behind a circular cylinder at high Reynolds number with experimental PIV and detached numerical simulations. The phase of the vortex shedding phenomenon was determined and phase average quantities were calculated using different methods, first by using the measure pressure signal in the wake downstream of the cylinder and second by using POD coefficients of the first two modes. It was found that the phase averaged vortices, obtained using POD, were less smeared by those obtained using the pressure signal. The turbulent stresses better followed the evolution of the vortices, and the contributions of both coherent and turbulent fluctuations were found to agree well with those evaluated from the velocity spectra. This enhancement was obtained because the phase angle was determined directly from the velocity fields to be averaged, thereby reducing the phase-jitter effect. A comparison with a detached eddy simulation demonstrated a high level of agreement obtainable between simulation and experiment, as well as confirming the enhancement of the phase averaging using this procedure. Lengani et al. [67] studied

the vortex shedding phenomenon induced by Kelvin–Helmholtz instability in the unsteady flow field developing along the separated flow region of a laminar separation bubble. They found that the first two POD modes of the wall-normal velocity were clearly energetically paired, and thus, it could be used to sort the PIV instantaneous velocity fields in order to phase-average the vortex shedding phenomenon. Another example of this approach was demonstrated in the investigation of the unsteady propagation of upstream wakes in a low-pressure turbine cascade by Lengani et al. [68] in which the first POD modes were used to organize time resolved the PIV measurements with respected to the wake passing period. Figure 2.12 shows a comparison between an original instantaneous velocity field and the filtered one.

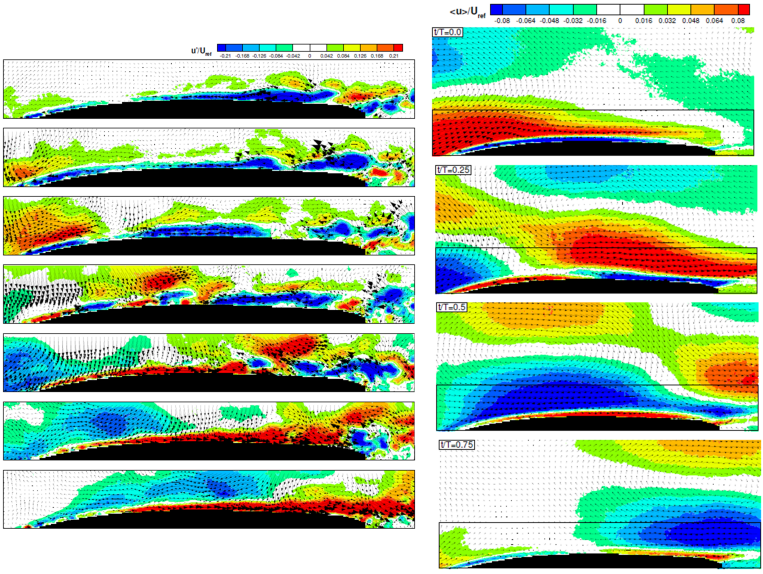

Figure 2.12: Instantaneous velocity vector map (left side), and phase average vector map using the POD method (right side) [68].

On the left side of the figure, a series of instantaneous velocity fields

is shown, while the corresponding phase-averaged velocity fields for four phases are presented on the right. These fields demonstrate the effect of phase averaging, highlighting the large-scale vortices characteristic of the dominant periodic motion of the flow while filtering out the smaller-scale structures and instantaneous flow fluctuations.

The basis of the capability of the POD to determine phase angle of the studied coherent motion depends on the ability to approximate the flow with a low-order flow model incorporating only the mean and the first two POD modes (see Ben Chiekh et al. [69]):

$$D(x,\theta) = D_{medio}(x) + \psi_1(\theta)\cdot\phi_1(x) + \psi_2(\theta)\cdot\phi_2(x) \tag{2.68}$$

$$\psi_1 = \sqrt{2\sigma_1}sin(\theta) \qquad \psi_2 = \sqrt{2\sigma_2}cos(\theta) \tag{2.69}$$

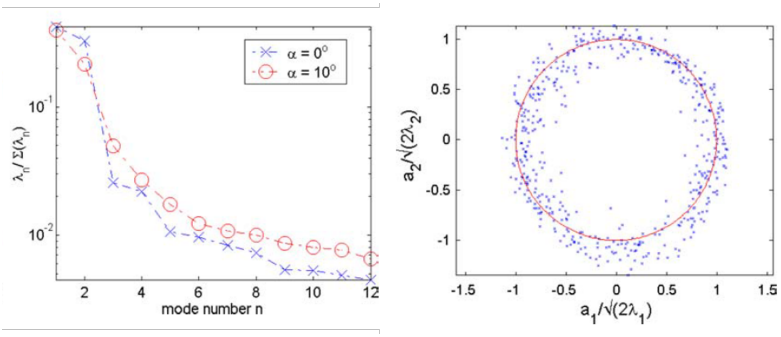

Figure 2.13: Singular value plot (left side) and mode coefficients correlation plot (right side) [66].

This low-order model neglects the higher order harmonics of the coherent motion as well as the random turbulent motion. The form of the model implies that the periodic or coherent part of the flow is captured by the phase shift between the first two POD temporal coefficients. This can be verified by plotting the corresponding mode coefficients ψ_1 and ψ_2 of the individual realizations. According to Equation 2.69, the coefficients

ψ_1 and ψ_2, although statistically uncorrelated, are not independent, but instead are predicted to form an circle in the normalized ψ_1 and ψ_2 plane:

$$\frac{\psi_1^2}{2\sigma_1} + \frac{\psi_2^2}{2\sigma_2} = 1 \tag{2.70}$$

The accuracy of the phase estimation obtained in this manner is dependent on the dominance of the first two modes in terms of energy. Fig. 2.13 shows singular values for two different angles of the square cylinder studied in [66] and the scatter plot in the normalized ψ_1 and ψ_2 plane for only the case labelled $\alpha = 0$. Plots demonstrate that in this case, for which the first two POD modes account for approximately 75% of the total energy, the individual realizations form a circular pattern indicating a strong phase shift correlation.

2.9 Particle Image Velocimetry

Particle Image Velocimetry (PIV) is an optical measurement technique used to obtain instantaneous velocity fields over an extended region of a flow. This section briefly outlines the method's main characteristics to introduce its fundamental operating principles. For a more detailed and comprehensive description of the technique, the reader is referred to specialized literature [70–72].

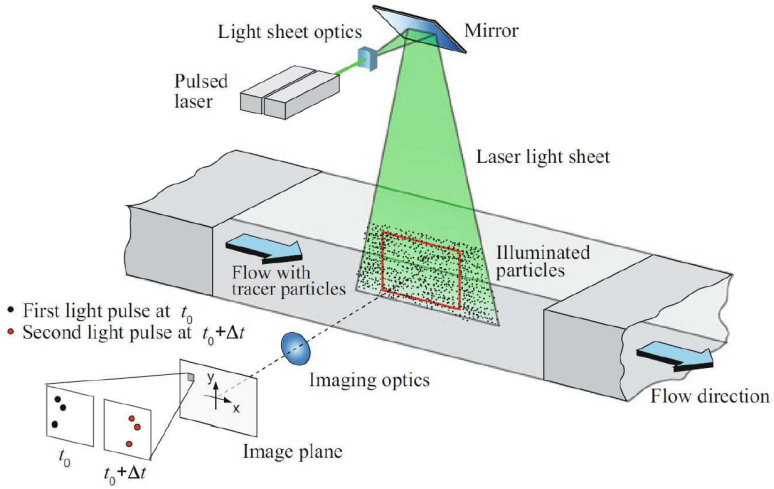

Figure 2.14: Schematic of the experimental arrangement for planar 2D PIV [70].

Figure 2.14 illustrates the operating principle of Particle Image Velocimetry. This technique involves introducing tracer particles into a flow and subsequently tracking their motion. The particles are typically illuminated by a dual-pulse laser sheet, and a CCD (charge-coupled device) camera captures the light scattered by the particles at two successive instants. The velocity field is obtained by determining the particle displacement between the two recorded images, which are separated by a

known time interval. Statistical techniques based on two-dimensional cross-correlation are then applied to estimate the displacement vector in the measurement plane. The time separation between the two laser pulses is a critical parameter and must be chosen carefully. If the delay is too large, loss of similarity between particle positions in the two images makes the estimated displacements less reliable. Conversely, if the delay is too short, particle displacement is minimal, reducing the accuracy and sensitivity of the velocity measurement.

The *scale factor* converts pixel coordinates into physical distances and is determined by a spatial calibration procedure. The measurement signal is enhanced by a laser system that emits monochromatic light with high energy density. A set of optical lenses shapes the laser beam into a thin light sheet, which is introduced into the measurement region to illuminate the seeded particles. Particle image velocimetry (PIV) cannot be considered a fully non-intrusive measurement technique since it requires the introduction of tracer particles into the flow. These particles must accurately follow the fluid motion to minimize discrepancies between the measured velocity and the true velocity of the fluid. For this reason, the fluid-mechanical properties of the tracer particles must be carefully evaluated according to the characteristics of the flow being investigated. The particles' ability to respond to flow variations is commonly quantified by the Stokes number, a dimensionless parameter defined as:

$$St = \frac{\tau U}{d_p} \tag{2.71}$$

where U denotes the local flow velocity, d_p is the particle diameter and τ represents the particle response time, defined as the time constant associated with the exponential decay of the particle velocity under the effect of drag forces. When the density of the seeding particles is significantly larger than that of the surrounding fluid, the particle characteristic response time can be approximated as:

$$\tau = d_p^2 \frac{\rho_p}{18\mu} \tag{2.72}$$

To accurately follow the fluid streamlines, the tracer particles must be characterized by a sufficiently small Stokes number. From a practical perspective, maintaining the condition $St < 0.1$ is generally accepted as ensuring reliable flow tracking, resulting in measurement errors typically below 1% [70]. In addition to their dynamic response to flow, seeding particles must also have suitable optical properties to efficiently scatter light and enhance measurement system sensitivity. Depending on the application, the seeding material can be solid, liquid, or gaseous. For low-temperature or non-reacting flows, mineral oil droplets are commonly employed due to their reliability and favorable scattering characteristics. In contrast, metal oxide powders are typically preferred as seeding materials for reactive flow conditions. As is well known, PIV measurements are affected by several potential sources of error, making a rigorous estimation of the overall uncertainty particularly difficult. Some inaccuracies originate from the optical configuration of the system and can be caused by imperfect calibration, small misalignments between the camera sensor and the measurement plane, or image distortions caused by lens aberrations. Additional uncertainties may arise from the laser system due to fluctuations in laser intensity or imperfect laser sheet alignment. Measurement quality can also be affected by seeding-related issues, such as non-uniform particle distribution or particle clustering within the flow. In reactive flow applications, further disturbances may occur when the luminosity of the flame interferes with visualization of the seeded particles. Despite these possible sources of error, an accurate experimental setup combined with appropriate validation procedures allows the measurements to remain reliable and provide a consistent representation of the velocity field.

2.9.1 PIV data post processing

A single PIV measurement results in a pair of digital images, referred to as frame 1 and frame 2. The pixel values of these frames are proportional to the intensity of the light reflected by the seed particles at the time instants t_1 and t_2 at which the images were acquired. The time interval between t_1 and t_2 is denoted by Δt. The post-processing system divides

each frame into smaller interrogation windows and computes the cross-correlation between each pair of corresponding windows from the two frames in order to determine the most probable displacements of different particle groups. The cross-correlation function, Φ, can be written as:

$$\Phi(\Delta m, \Delta n) = \iint_{-\infty}^{+\infty} I_1(m,n)\, I_2(m+\Delta m, n+\Delta n)\, dm\, dn \tag{2.73}$$

where I_1 represents a generic interrogation window of frame 1 and I_2 the corresponding interrogation window of frame 2. The variables m and n denote the pixel indices corresponding to the spatial dimensions in the x and y directions, respectively. The quantities Δm and Δn represent the shifts, expressed in pixels, applied to the second image in the m- and n-directions. In integral form, it represents a continuous scalar product between the interrogation windows, or in other words, a projection of the first window onto the second, with the second window shifted in pixel space by $(\Delta m, \Delta n)$. The quantity Φ is a scalar field, and each value of Φ represents the degree of similarity between the two windows as a function of the shift applied to the second window. A discretization is required in order to apply Equation 2.73 to the discrete image data. In discrete form, the cross-correlation function can be written as:

$$\Phi_d(\Delta m, \Delta n) = \sum_m \sum_n \left[I_1(m,n) \cdot I_2(m+\Delta m, n+\Delta n) \right] \tag{2.74}$$

The shifts Δm and Δn range from zero to the maximum pixel shift for which there remains an overlap between the interrogation windows. Furthermore, the summation limits are not infinite but are defined by the number of pixels in the m- and n-directions of the interrogation window. If the system is set up correctly, Φ_d will have small but non-zero values for all shifts $(\Delta m, \Delta n)$ except for one particular value $(\Delta m_p, \Delta n_p)$, for which Φ_d exhibits a dominant peak. This peak in the cross-correlation indicates that the images inside the interrogation windows most closely resemble each other when the shift $(\Delta m_p, \Delta n_p)$ is applied. This shift is

therefore taken as the net displacement of the particles initially contained in the first interrogation window over the time interval Δt. The velocity of the particle group is consequently given by:

$$\vec{V}_p = \frac{\Delta \vec{p}}{\Delta t} = \frac{[\Delta m, \Delta n]}{\Delta t} \tag{2.75}$$

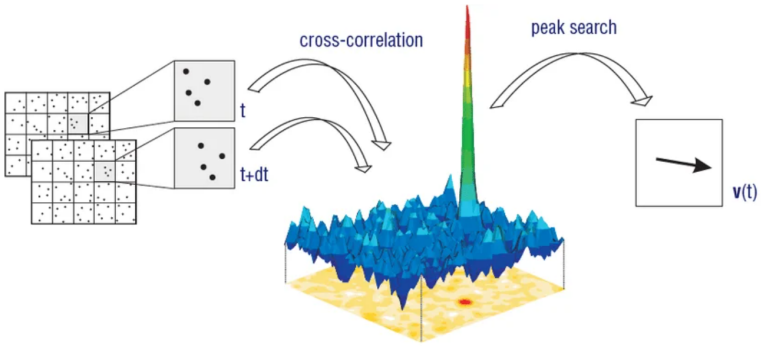

Figure 2.15: The cross-correlation technique is typically used in PIV. The position of the highest peak in the correlation plane indicates the most likely displacement vector.[73]

Where $\vec{V}_p$ is the velocity in pixel space, and $\Delta \vec{p}$ is the net pixel displacement vector. Multiplying $\vec{V}_p$ by the scale factor determined by the calibration procedure.

2.10 PIV applied to multi-phase flow

The presence of multiple phases, such as in the present case of oil and air systems, makes it challenging to apply the traditional PIV technique described above. This is because in multi-phase flows the assumption of a continuous phase, the motion of which is tracked by a large number of uniformly dispersed seeding particles, is no longer valid. Instead, the flow is composed of a continuum-phase and a dispersed-phase. The dispersed-phase may be present in the continuum-phase with a large variability of shapes, sizes, and densities. In these cases, other optical techniques

or modifications to the traditional PIV are required to account for the presence of both phases and their velocity fields. Due to the potentially wide variation in particle concentration (if seeding particles are used) and dispersed-phase concentration (void fraction) across different interrogation areas, the choice of the most appropriate measurement techniques depends on the structure of the studied multi-phase flow. Methods such as Particle Tracking Velocimetry (PTV), Laser-Induced Fluorescence (LIF)-PIV, Shadow Photography (SP), and Planar Fluorescence for Bubble Imaging (PFBI) have been developed for velocity measurements of two-phase flows. These approaches enable the acquisition of experimental data for each individual phase in multiphase flow systems. This section outlines the advantages and limitations of the predominant measurement techniques reported in the literature.

2.10.1 Particle Tracking Velocimetry

Unlike PIV, which determines a velocity vector for each IA with, in general, many particles present in each one, PTV determines velocities for individual particles. PTV is carried out in two steps: in the first step, identification, individual particles are detected by using any one of a variety of possible image processing or machine learning techniques, and in a second step, pair matching, particle displacements are calculated by matching corresponding particles between two images separated by a known time delay. Because the method depends on the explicit calculation of individual particle displacements, and not on the most probable displacement of groups of particles as in PIV, the identification step in PTV has a strong influence on the quantity of particle pairs identified and on the accuracy of their calculated velocities. In fact, individual velocity errors in PTV are mostly related to the estimate of particle centroids [74]. Asymmetry in both shape and illumination profiles yields to an ambiguity on the centroid position and thus introduces a bias on the estimation of the particle location [75]. To minimize the influence of these errors it is desirable to have measurements where the particles travel a longer distance than in PIV. For high-density seeded flows this makes tracking

difficult and a compromise between particle density and image delay is required.
For this reason, PTV historically has been limited to spherical, or nearly spherical, particles and with up to moderate seeding densities. In such cases, algorithms for particle detection such as particle mask correlation [76] and dynamic threshold binarization [77] combined with algorithms to match the pairs of detected particles have provided good performance. Algorithms that solve the temporal matching problem include those based on Binary Cross-Correlation (BCC) and those based on relaxation labeling technique, also called relaxation method (RM) [78]. Such analysis has been applied successfully to multiphase flows where dispersed-phase gas bubbles moving in a continuum liquid phase are treated as the particles to be identified and tracked [74, 79, 80].
More recently, machine-learning-based image segmentation methods have been developed to apply PTV to situations in which the particles to be tracked have highly non-spherical, and large variations of shapes, as well as of densities and sizes [81–84]. Many of these methods were initially developed for segmenting cell nuclei in biomedical images, and generally involve laborious manual annotation required for model training. Furthermore, substantial time and effort may be required to rebuild algorithms or datasets when applied to particles of other shapes.

2.10.2 LIF-PIV

This method is based on the same experimental setup as that of the dual-pulsed laser PIV described previously, but is implemented with the additional use of a fluorescent dye light (e.g., PMMA doped with Rhodamine B) encapsulated in the seeding particles. The fluorescent dye of the particles, added to a single phase of a multiphase flow, absorbs energy at the incident laser wavelength and emits light at a longer wavelength, while in general there is also scattered light present at the incident laser wavelength. Distinguishing fluorescent light from the scattered light requires a camera fitted with an appropriate cut-off filter that transmits only the fluorescent light emitted by the tracers. Application of wavelength

discrimination can be found in studies of two-phase flows, such as particle-laden flows [85] or air/water systems[86] and Honkanen et al. [87]. In all of these works, two CCD cameras were employed to measure the velocity field. The first camera, equipped with a low-pass filter, was used to capture the continuum phase by detecting the fluorescent tracer particles. The second camera, fitted with a band-pass filter, was dedicated to imaging the cavitation or dispersed phase. Several studies in the literature demonstrated the LIF-PIV method for gearbox lubrication applications [88, 89]. Both works focused on measuring the velocity flow field in the oil bath by seeding this continuum phase with fluorescent particles. The results clearly illustrated the recirculation zones created due to the gear motion in the bath. In particular, Hartano et. al.[89] demonstrated a stereo PIV method to measure three-component velocities and determined that the oil squeezing effect in the gear meshing region is minimal compared to the losses associated with recirculation phenomena.

2.10.3 Shadow Photography

Unlike the approaches described to this point that illuminate particles using a planar light sheet, in Shadow Photography (SP) [90] a diffuse backlight is used to illuminate the entire measurement volume and the shadows cast by particles are recorded by a CCD camera. SP was widely employed to determine the position and shape of bubbles in air/liquid multiphase flows with low void fractions (below $1-2\%$). The main advantage of ST is that it can be easily combined with the PIV/LIF technique (i.e., when PIV is applied for fluorescent tracers) by using the appropriate optical filters for light sources with different wavelengths. The use of one or two cameras in ST together with PIV/LIF allows the bubble dynamics and their interaction with the liquid phase to be studied in detail (e.g., Tokuhiro et al.[91] and Lindken and Merzkirch [92]). One of the main problems faced in SP is overlapping particle images, which occurs when the void fraction is high. Advanced image-processing methods, such as those proposed by Honkanen et al. [93], Broder and Sommerfeld [94], and Honkanen and Marjanen [95], are required in these cases to which effec-

tively analyze experimental data images of dense multi-phase flows with irregularly shaped particles of dispersed phase. These methods are generally based on image intensity gradient filters to identify phase boundaries and on geometric analysis to identify overlapping shapes. However, as the domain is backlit, the measured shadows come from particles distributed in the entire measurement volume. Therefore, determining the position of bubbles relative to the camera's focal plane still requires an additional camera. This camera is typically positioned at a 90° angle with respect to the primary camera. At high void fractions, identifying the same bubble in images from both cameras and accurately reconstructing its position in three-dimensional space becomes problematic.

2.10.4 Planar Fluorescence for Bubble Imaging

Planar fluorescence for bubble imaging (PFBI), represents a convenient tool to identify round particles located within and very close a planar laser sheet. Details of the PFBI approach are described by Dulin et al. [96], including the optical principles and a PFBI application test case of singly rising bubbles. One of the principal advantages of this technique is that the particles located far from the measurement plane (i.e., lasersheet) become defocused rapidly (similarly to an interferometric approach), so that experimental information in a rectangular measurement volume with low thickness can be obtained. The post-processing procedure for this technique has much in common with the previous ones described; it involves identifying particle positions and sizes, filtering defocused particle images, matching particle pairs and calculating particle displacement vectors. PFBI can be successfully applied for bubble flows with void fractions up to 6% [97].

Overall, the literature shows that significant research has been devoted to characterizing windage and churning losses in geared systems. However, the complex and highly unsteady multiphase flow generated by splash-lubricated gears remains only partially understood, particularly in terms of the interaction between the dispersed oil phase and the surrounding air. Existing experimental techniques provide valuable information, but

their applicability to the present flow is limited by the wide range of particle sizes, the strongly unsteady nature of the flow, and the difficulty of reliably tracking the dispersed oil phase. These limitations highlight the need for experimental approaches capable of providing spatially and temporally resolved measurements of the oil flow. This work therefore aims to develop and apply an optical velocimetry approach based on PIV to characterize the dispersed oil phase and investigate its relationship with the power losses of splash-lubricated spiral-bevel gears.

Chapter 3

Methodology

Contents

3.1 Test rig overview 67
3.2 Description of the test rig 68
3.2.1 Chamber 69
3.2.2 Power Losses Measurement 74
3.3 Physical model definition 76
3.4 PIV measurement set-up 80
3.5 Application of POD for the study of splash lubricated gears 84

3.1 Test rig overview

According to the expected outcomes of this Ph.D. work described at the end of Chapter 1, a new test rig has been developed to experimentally investigate the churning power losses of spiral bevel gears at high rotational speeds under splash lubrication conditions. The purpose of this chapter is to describe the test rig, including its main components, operating range, and possible configurations.

A photograph of the new test rig, installed in the THT Lab of the University of Florence, can be seen in Figure 3.1.

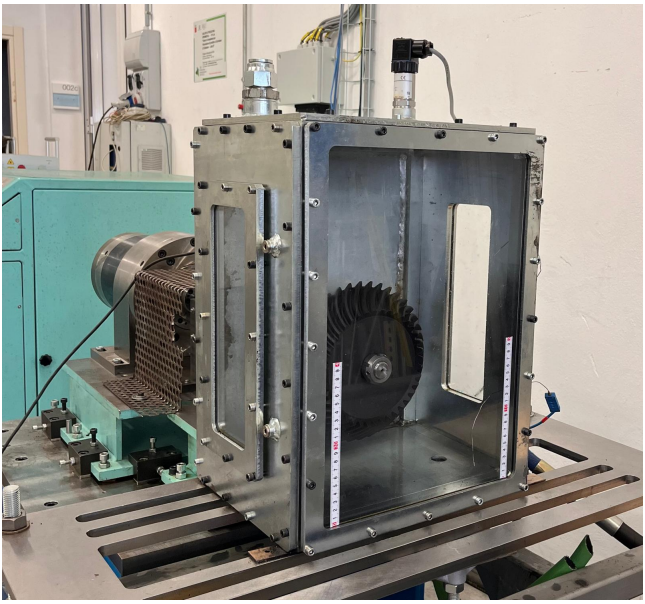

Figure 3.1: Photograph of the splash lubrication test rig installed in the THT Lab at the University of Florence.

3.2 Description of the test rig

The experimental facility was designed to operate in either air-only or oil-bath conditions. In the windage test campaign, the rig operated only in an air environment.

The facility allows a single gear to run inside a closed chamber at speeds of up to 5000 rpm while continuously monitoring air pressure and temperature. As illustrated in Fig. 3.2, the test rig consists of three main different parts.

1. Electrical motor
2. Drive train
3. Test housing

In the drive train there is a rotating shaft supported by two ball bearings arranged in an "O" configuration. The bearings are mounted inside a sealed housing with inlets and outlets for lubrication, as well as ports for sensor installation. A dedicated oil supply unit provides lubrication by delivering ISO VG 46 oil at a controlled mass flow rate and temperature. The bearing housing is instrumented with two accelerometers to monitor system vibrations. Torque transmission between the shaft and the drive system is achieved through a bearing-less torque meter that connects the shaft to an electric spindle. The spindle is capable of reaching a maximum speed of 15000 rpm and a maximum torque of 30 N·m. Windage and churning power losses were measured using a bearing-less rotary torque transducer (Lorenz Messtechnik DR-2500). This device operates at rotational speeds up to 30000 rpm and supports a maximum sampling frequency of 10 kHz. According to the manufacturer, the measurement accuracy is 0.1% of the full scale value (10 N·m). All sensor signals were acquired and managed through a data acquisition system developed in the LabVIEW environment. The experimental campaign was conducted on gears developed at the University of Florence that were characterized by different pitch diameters, face widths, and numbers of (see section 3.2.1.1). Tests were performed with and without lubrication and at tangential velocities of up to about 60 m/s.

3.2.1 Chamber

The test bench chamber is made of structural steel with a surface roughness of Ra 6.3 μm. It is designed to allow windage and churning experiments to be carried out. Since the churning experiments required the test rig to be sealed, this guaranties that the windage test was conducted without air exchanges between the chamber and the ambient. Fig. 3.3 shows a schematic of the chamber, where the main dimensions are reported in non-dimensional form and the position of the test gear within the enclosure is indicated. The gear is located at the center of the chamber, and its relative position is shown in the Fig. 3.3. The gear is secured to the shaft by means of a locknut. Thanks to its specific

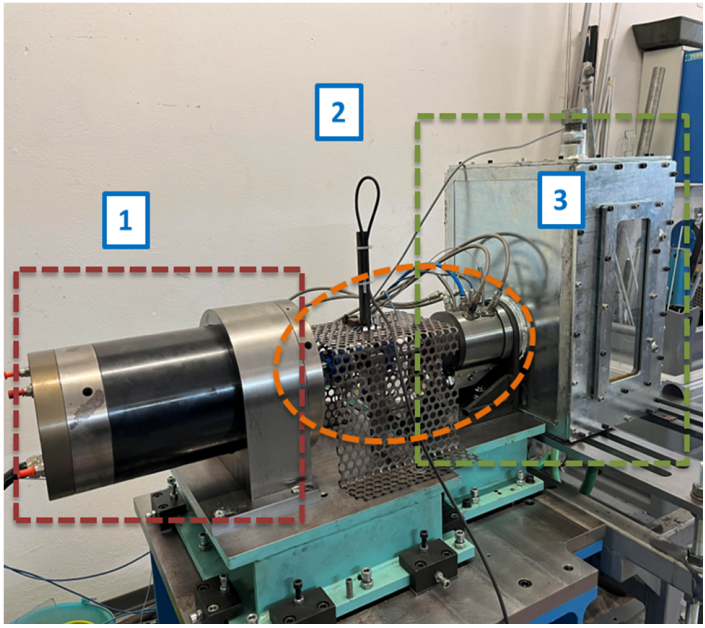

Figure 3.2: High speed test rig layout.

configuration, the system allows the installation of gears with different geometrical characteristics. For clarity, Fig.3.3 also illustrates the chamber and shows how it is equipped with measurement and service instruments. The chamber is instrumented with:

- Two T-type thermocouples are mounted at different heights on a sidewall to measure air temperature (and oil temperature during churning tests) with an accuracy of $\pm 0.5^{\circ}C$;

- A flush-mounted pressure sensor on the top cover operates in a range of -1 to 1.5 bar with an accurancy of $\pm 0.5\%$ of the full scale;

The chamber also featurs side and front optical accesses that allow viewing of the flow during churning tests.

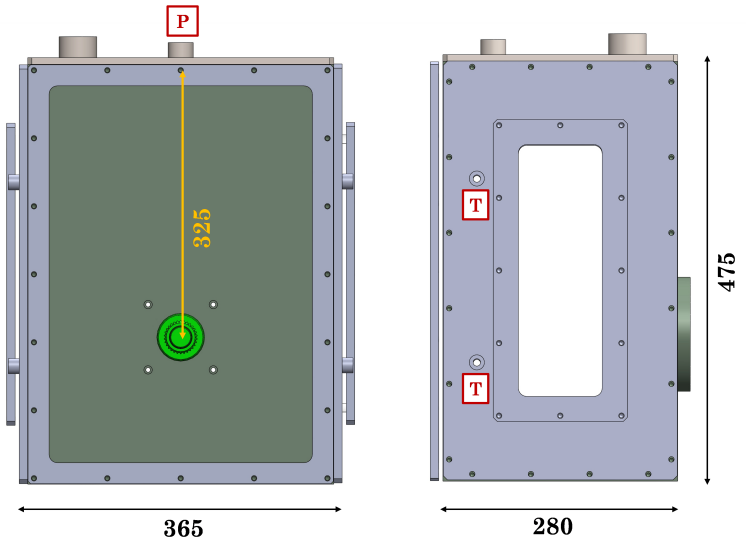

Figure 3.3: Chamber layout.

3.2.1.1 Gear Geometries.

Different spiral bevel gear geometries (see Fig. 3.4, 3.5, 3.6) are designed and manufactured using 3D printing with Onyx. Onyx is carbon-fiber-reinforced nylon. It was chosen for its combination of high stiffness, low deformation under load, an excellent surface finish, and improved wear resistance, all of which make it suitable for functional mechanical components. Using Onyx and 3D printing allows for the rapid production of complex geometries and functional prototypes, enabling quick verification within the test rig. Using Onyx avoids the high cost and longer lead time of metal gears, as well as the need for additional machining, while providing sufficient mechanical performance for low-load testing. The surface finish is typically approximately Ra 10–20 μm. This relatively high surface roughness compared with that of conventional steel gear flanks may influence the measured power losses, particularly through its effect on fluid–surface interaction. In addition, the lower thermal conductivity of

Onyx compared with steel may affect heat dissipation and, consequently, the oil temperature and viscosity. These material-related differences may therefore have an influence on the experimental measurements. Although their effects are not specifically investigated in the present study, they should be considered when interpreting and comparing the experimental results.

The gear geometries investigated in this work differ from one another in terms of their width (see Fig.3.4), pitch cone angle (see Fig.3.5), and mean spiral angle of the teeth (see Fig.3.6). However, their pitch outer diameter and number of teeth are the same for all geometries. Their characteristics are reported in Tab.3.1, 3.2, 3.3.

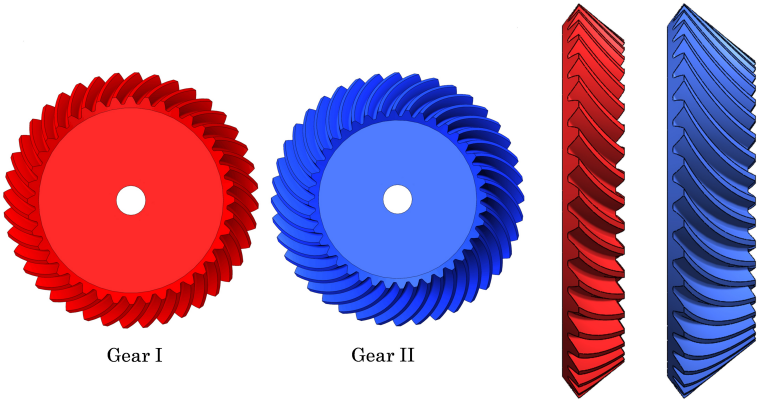

Figure 3.4: Different geometries of the spiral bevel gears for the gear width.

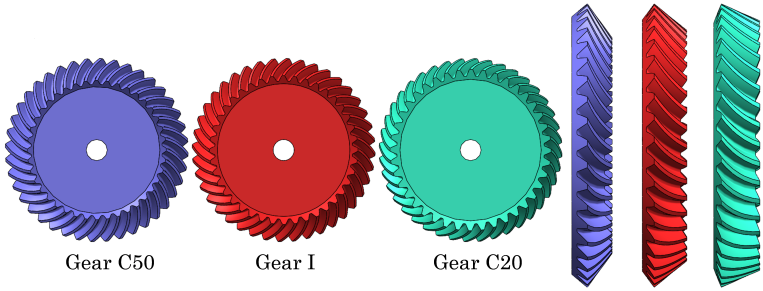

Figure 3.5: Different geometries of the spiral bevel gears for pitch cone angle.

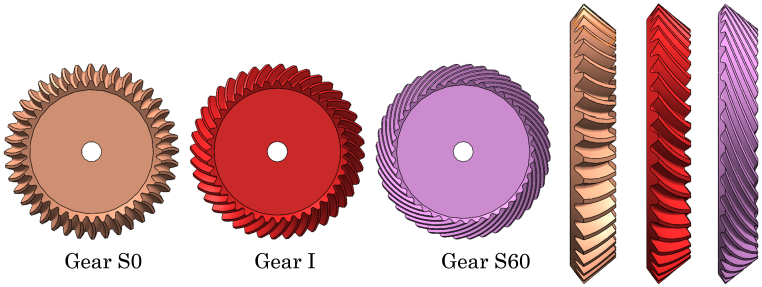

Figure 3.6: Different geometries of the spiral bevel gears for swirl angle of the teeth.

Table 3.1: Gears' characteristics with different Width

	Gear I	Gear II
Outside diameter [mm]	235	235
Number of teeth [-]	40	40
Gear width [mm]	35	55
Normal pressure angle [°]	20	20
Rotation direction	ACW	ACW

Table 3.2: Gears' characteristics with different Cone Angle

	Gear I	Gear C50	Gear C20
Outside diameter [mm]	235	235	235
Number of teeth [-]	40	40	40
Gear width [mm]	35	35	35
Normal pressure angle [°]	20	20	20
Pitch cone angle [°]	36	52	22
Rotation direction	ACW	ACW	ACW

Table 3.3: Gears' characteristics with different Mean Spiral Angle

	Gear I	Gear S0	Gear S60
Outside diameter [mm]	235	235	235
Number of teeth [-]	40	40	40
Gear width [mm]	35	35	35
Normal pressure angle [°]	20	20	20
Mean spiral angle [°]	31	0	60
Rotation direction	ACW	ACW	ACW

3.2.2 Power Losses Measurement

The torque measurements of the system are acquired through the torque meter, which is placed between the electric spindle and the drive train. The latter is sensitive to any torsional force that acts on the driven shaft. Consequently, the bearing chamber affects the device's readings. The torque meter measures all system losses, including the contributions from the bearings, the seals, shaft, and gear. It is therefore necessary to subtract the contributions of the bearings, the seals and shaft from the total measured torque in order to isolate the losses attributable solely to the gears. To this end, a series of preliminary tests is performed to quantify the drive train losses. The lubricating oil temperature, mass flow rate, air density, and gear rotational speed are all parameters that can influence the measurements; therefore, all tests are conducted under steady-state conditions, defined by constant oil and bearing temperature and pressure.

An initial test phase is conducted with the test rig operating without the gears, using only the shaft. During this phase, only the shaft rotational speed is varied, while all other potentially critical parameters are kept constant. In this way, we isolate the contribution of drive train losses so that subtracting it from the torque measurements yields only the contribution of windage losses attributable to the gear. A similar procedure, described in detail in a subsequent section (see section 4.2), was also applied during the churning tests to isolate the contribution of losses specifically attributable to the churning process.

A test campaign is performed to study how different geometric characteristics of spiral bevel gears could influence windage and churning power losses. The test activities are conducted at ambient air pressure and temperature inside the box, at different rotational speeds ranging up to 5000 rpm, and under steady-state conditions of the bearing lubrication system.

3.2.2.1 Uncertainty Analysis.

For the torque meter described above, the accuracy specifications were provided. However, a thorough uncertainty analysis was conducted, since the torque attributed to the gear windage and churning losses is obtained by subtraction, as explained earlier. Therefore, the uncertainty of the resulting windage and churning torque was recalculated by applying the standard error propagation method for the difference between two independent measurements, in accordance with the literature [98].

For the windage measurements, the measurement uncertainty of the gear loss torque was estimated to be approximately 20% at 1000 rpm where the measured torque values are small and comparable to the instrument's resolution. It decreases to about 3% at 5000 rpm. For the churning measurements, the measurement uncertainty was estimated to be approximately 7% at 1000 rpm and decreases to about 2% at 5000 rpm.

To verify repeatability, multiple control tests were performed under various operating conditions and for all tested gear geometries. These

tests revealed minimal variation between repeated measurements, approximately 0.6%, demonstrating that the system provides consistent and reliable torque values, even at low speeds. Overall, although the relative uncertainty is higher at low rotational speeds, the combination of an acceptable measurement uncertainty and good repeatability ensures that windage torque can be reliably estimated across the full operating range.

3.3 Physical model definition

This section proposes a model for predicting windage losses in spiral bevel gears operating in air. The correlation presented here is adapted from the formulation originally developed by Diab et al.[19], which was conceived for spur gears. This study extends and modifies that correlation to account for the geometric characteristics specific to spiral bevel gears, enabling its application to spiral bevel gear transmissions operating in air. In accordance with the literature [19, 27], the parameters assumed to have the greatest influence are the geometric parameters of the gear (e.g. radius, thickness, and number of teeth) and the fluid-dynamic parameters (e.g. ρ and μ). The total windage moment is therefore expressed in the following form:

$$M_g = f(\rho, \omega, \mu, R, b, Z, h_{1,2}) \tag{3.1}$$

The dimensionless windage moment coefficient is defined as:

$$C_t = \frac{M_g}{\frac{1}{2}\rho\omega^2 R^5} \tag{3.2}$$

Based on the dimensional analysis proposed by Diab et al. [19], the C_t equation may be written in terms of dimensionless parameters as:

$$C_t = \alpha Re^{\beta} \left(\frac{b}{R}\right)^{\gamma} Z^{\delta} \left\{ \left(\frac{h_1}{R}\right)^{\phi} + \left(\frac{h_2}{R}\right)^{\phi} \right\} \tag{3.3}$$

Where $\alpha, \beta, \gamma, \delta$ and ϕ are constant coefficients, obtained from experimental results [19], reported in Tab.3.4, and Re is the Reynolds number, and Z is the number of teeth. Meanwhile $h_{1,2}$ is a coefficient that considers

the presence or absence of a deflector.

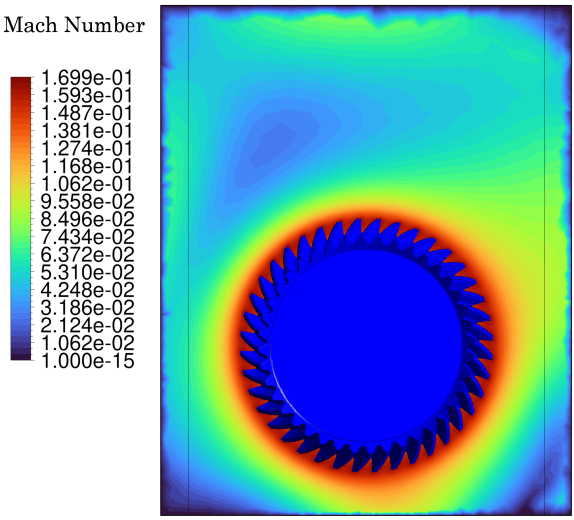

Figure 3.7: Mach number profile.

The main assumption for reformulating the correlation in Eq. 3.3 is that a spiral bevel gear can be traced back to an equivalent spur gear by modifying its radius, thickness, and the number of teeth. In evaluating the modifications to the correlation, it is assumed that, for all tests, variations in tangential velocity remain well below the threshold at which compressibility effects become significant, and that both compressibility effects and pressure-induced density variations can be considered negligible. This assumption is supported by CFD results for Gear I, as shown Fig. 3.7, which show the Mach number values under the most critical test conditions, namely, when the peripheral velocity reaches its maximum, he Mach number is found to be approximately 0.18 under ambient pressure and temperature conditions. This value indicates that the flow remains well within the subsonic regime. Since the Mach number is below 0.3, compressibility effects are expected to be negligible, and the air can therefore be reasonably considered incompressible. Figure 3.8 shows the

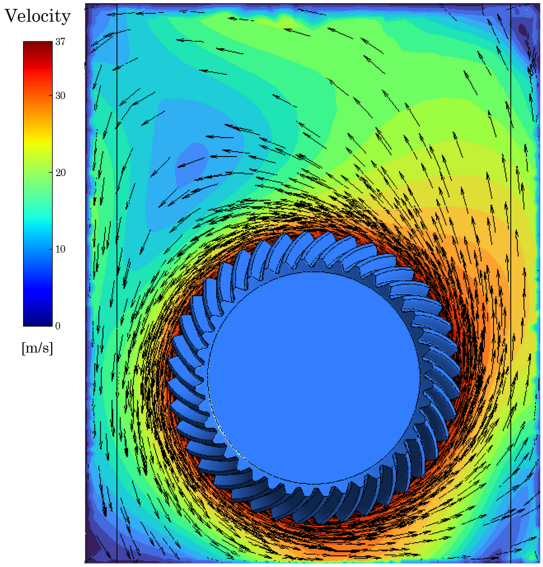

Figure 3.8: CFD result about windage for Gear I at 3500 *rpm.*

corresponding flow field in terms of velocity magnitude and directions. The results were obtained from Unsteady Reynolds-Averaged Navier–Stokes (URANS) simulations performed in ANSYS CFX. The Immersed Solid approach was employed to accurately handle the rotating gear domain (details can be found in [99]).

$$R^* = \frac{2R_c sin(\delta_c) - bsin(\delta_c)}{2} \tag{3.4}$$

In Equation 3.4, R^* is the new radius of the bevel gear converted to the spur gear, while R_c, b and δ_c are the outer pitch cone distance, face width and the pitch cone angle respectively, of the original spiral bevel gear.

$$b^* = bcos(\delta_c) \tag{3.5}$$

b^* is the face width of the corresponding spur gear geometry.

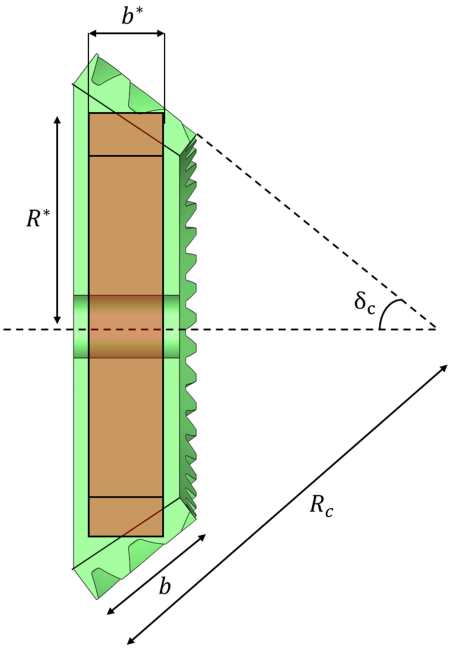

Figure 3.9: Conversion of a bevel gear into an equivalent cylindrical gear.

$$C_t = \alpha Re^{\beta} \left(\frac{b^*}{R^*}\right)^{\gamma} Z^{\delta} cos(\theta) \left\{ \left(\frac{h_1}{R^*}\right)^{\phi} + \left(\frac{h_2}{R^*}\right)^{\phi} \right\} \tag{3.6}$$

The constants introduced in Eq.3.3 are kept unchanged, given the assumption that the spiral bevel gear is referred to an equivalent spur gear, for Eq.3.6 and correspond to the values listed in Tab.3.4. Since in the case of study there aren't any obstacles on the side of the gear, $h_{1,2}$ takes this form:

$$h_{1,2} = 0.5^{1/\phi} R^* \tag{3.7}$$

Multiplying the number of teeth Z by cosine of θ yields the projection

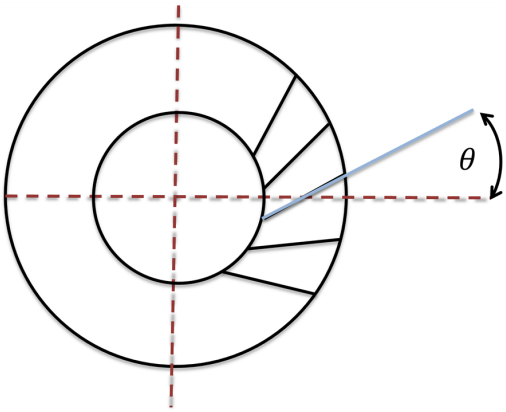

Figure 3.10: Mean spiral angle of spiral bevel gear.

along the axis of the gear itself (see Fig.3.10), converting the teeth of the spiral bevel gear into straight spur teeth.

Table 3.4: Constant coefficients in Eq.3.3.

α	β	γ	δ	ϕ
60	-0.25	0.8	-0.4	0.56

Windage power losses are assessed in the Results section (see Chap. 4) using the following formula:

$$P = M_g \omega \tag{3.8}$$

3.4 PIV measurement set-up

PIV measurements performed in the present experimental campaign have been carried out using a Dantec Dynamics PIV system. Data acquisition and post-processing have been managed through the Dantec FlowManager software. During the acquisition phase, the software regulates the instrument parameters while a programmable timing unit (PTU)

provides the trigger signals needed to synchronize the camera and laser system. The illumination source used in the experiments is a Litron LDY303 pulsed Nd:YLF laser that operates at a wavelength of 527 nm. The system has a sampling rate ranging from 0.2 to 20 kHz and delivers pulse energies up to 20 mJ. Images were recorded with a Phantom MIRO M340 camera, equipped with a 2560x1600 pixel CMOS sensor with 12 bit sensor depth and 10 μm pixel size. The camera acquisition frequency is 800 fps at full resolution and it can be increased up to 50 kHz with lower resolution. The camera was coupled with a Micro NIKKOR 60mm f/2.8 lens and a narrow band pass filter (Central Wave Length (CWL) of 527 nm and Full Width at Half Maximum (FWHM) of 5 nm) to cut out all the incoming light except for the laser light scattered by the seeding particles. A time delay of 100 μs has been used for churning condition and of 300 μs for windage condition. The PIV system was operated with an acquisition frequency of 10 Hz in double frame mode.

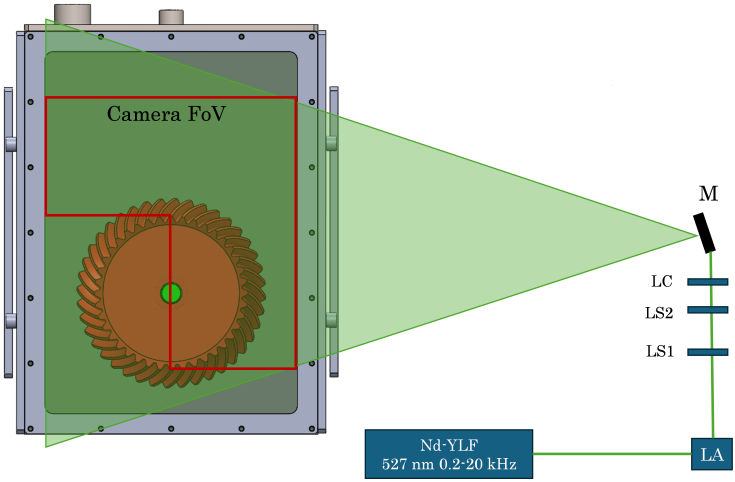

Figure 3.11: Schematic of PIV measurement set-up - Front View.

The PIV technique can be implemented with the optical setup shown in Figures 3.11, 3.12 using the two perpendicular optical accesses on

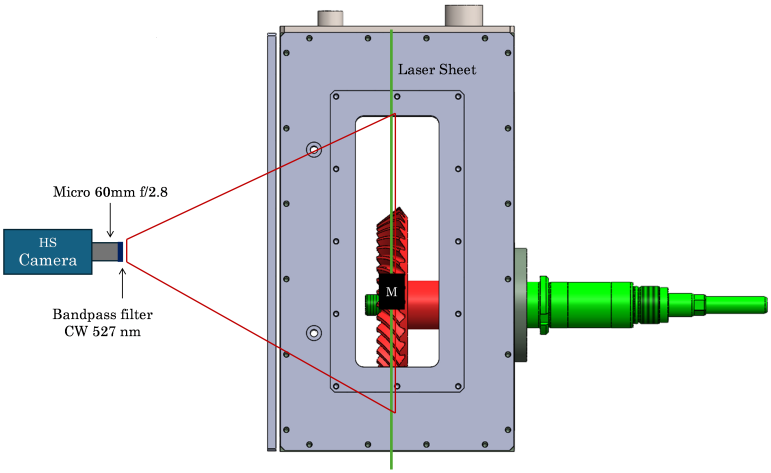

Figure 3.12: Schematic of PIV measurement set-up - Side View.

the chamber. The laser beam enters an optical trail via a laser arm (LA), which is connected to the laser outlet. The optical trail consists of two planispheric lenses (LS): a concave lens (LS1) and a convex lens (LS2). A cylindrical concave lens (LC) follows to generate the laser sheet. A final silver mirror (M), which is mounted on an adjustable system, projects and aligns the laser sheet into the desired part of the test rig. The focal lengths and relative distances of the lenses have been selected to produce the desired focal line with a laser sheet thickness of about 1 mm inside the chamber of the test rig, as shown in Figure 3.13b with the measurement area. However, the area of interest shown in Figures 3.11 and 3.13 is limited by two factors. First, measurements cannot be performed in the oil bath. Second, the left side of the gear obstructs the laser beam. Therefore, the field of view is defined as a single region corresponding to the area of interest: the region extending perpendicular to the gear's axis of rotation, from the side where the wheel draws in and projects oil toward the sidewall. To ensure consistent comparisons for all configurations studied, the laser beam passes through the mean pitch

(a)

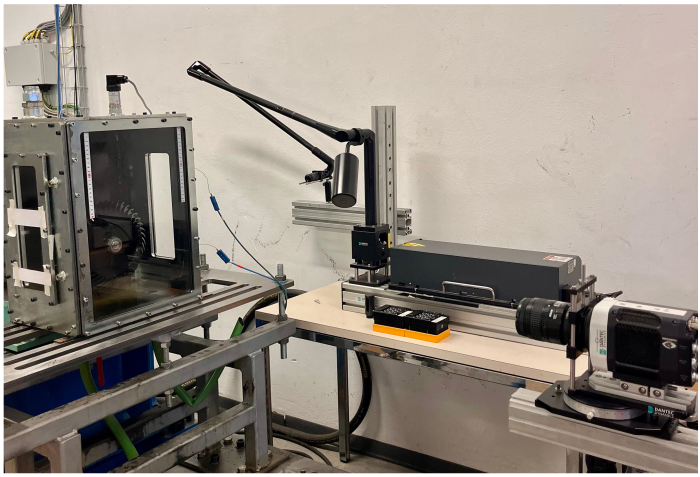

(b)

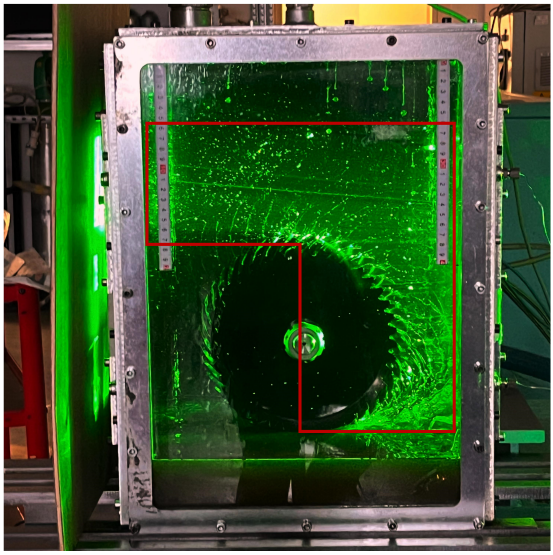

Figure 3.13: Picture of PIV measurement set-up (a) and measurement area (b).

diameter of each gear, which is the diameter corresponding to half the face width. The camera was installed on a fixed structure in front of the test rig. For windage velocity measurements olive oil particles with an average diameter of approximately $1\mu m$ were used as seeding, introduced into the test chamber by a Laskin nozzle.

The cross-correlation of the acquired image pairs was calculated using the DANTEC FlowManager tool. The first step in the post-processing stage is background noise removal. This is achieved by subtracting the averaged single pixel intensity from each acquired image. Then, an iterative adaptive cross-correlation algorithm was applied, starting with a coarse interrogation window of 64×64 pixels and concluding with a finer window of 8×8 pixels, with 50% overlap. This procedure resulted in a spatial resolution of 0.765×0.765 mm^2. A peak validation with a threshold of 1.1 between the dominant and the second-most dominant peaks was used to discriminate between valid and invalid vectors. The universal outlier detection algorithm replaces any rejected vectors with the median of the neighboring vectors. The instantaneous velocity maps obtained with Dantec software undergo further post-processing using user-defined routines in MATLAB.®.

For the churning velocity measurements the oil particles projected by the gear teeth themselves are used as seeding. The method to adapt the traditional PIV to this setting is discussed in the following section.

3.5 Application of POD for the study of splash lubricated gears

One objective of this work is to demonstrate an effective optical velocimetry method to measure the dispersed phase oil particles released by a splash-lubricated spiral-bevel gear in the continuum air phase above the oil bath. This multi-phase velocimetry problem is challenging because, depending on such properties as gear speed and geometry, and oil type, temperature and immersion level, the oil particles flung from the gear may have a large range of sizes, shapes, and concentrations, as shown in

figure 3.13b. Furthermore, the process is highly unsteady, with substantial variations in oil particle behavior depending on the motions of the oil bath. All these factors make the multi-phase flow velocimetry methods reported in the literature (presented in section 2.10) unsuitable for the present application.

In this work, the PIV measurement setup and post-processing algorithm based on the cross correlation of digital image pairs discussed in the previous subsection are used to calculate individual instantaneous velocity fields during churning tests. This takes advantage of the capability of the traditional PIV method to robustly calculate the most probable displacements of groups of particles without having to distinguish each one individually. The oil particles themselves were treated as the seeding particles whose velocities are sought, and the velocity measurements were limited to the oil particles by using an image thresholding technique: first a contrast limited adaptive histogram equalization (CLAHE) [100] is used to enhance the detectability of the oil particles and normalize the intensity of the light scattered by the oil across all mean-subtracted image pairs. Then a binarization of each image was performed by setting all pixels with an intensity above the image mean value equal to 1 and all others to 0. This binary masks were used to limit the velocity field to only IAs that correspond to the oil particles identified by the mask values equal to 1. This makes it possible to neglect the velocity vectors which the PIV algorithm assigns to IAs containing no seeding (dispersed phase) particles, and thus that lack physical significance.

Due to the unsteady nature of the phenomenon, a more generalized and robust characterization of the oil particle distribution and velocities can be obtained via phase averaging of the instantaneous velocity fields. In this case, the periodic component of the motion is defined by the passing frequency of the gear teeth. To accomplish this, the POD-based procedure described in Section 2.8 is applied to the raw images of the PIV data set, and each instantaneous velocity field is sorted according to its phase within the gear tooth-passing cycle. POD is applied to the pixel intensity of raw image data instead of to one of the velocity components

of the instantaneous velocity fields, as the presence of the gear teeth in the images give a very strong signal from which to calculate the phase. Phase-locked averaged velocity fields were then obtained by averaging all of the instantaneous fields falling within the same fixed, narrow phase angle intervals. Fifteen intervals were used, which, given each gear studied has 40 teeth, results in 0.6 degrees of gear rotation per interval.

Chapter 4

Results

Contents

4.1 Windage Power Losses 87
4.1.1 Physical Model Validation 91
4.2 Churning Power Losses 94
4.3 Velocimetry 106
4.3.1 Windage 107
4.3.2 Churning 108

This chapter presents and discusses the results of the tests conducted throughout the campaign. The results include findings on windage losses, churning tests, and velocity measurements. Additionally, the results from windage measurements for various gear geometries were used to validate the previously proposed physical model in a dedicated Section 3.3.

4.1 Windage Power Losses

This section presents the windage results, which aim to analyze the influence of spiral bevel gear geometry on associated power losses. Assuming the same outer pitch diameter and number of teeth, three main geometric parameters were examined: gear width, pitch cone angle, and

Table 4.1: Windage test conditions.

	Geometry	Speed [rpm]
Windage	Gear I Gear II Gear C20 Gear C50 Gear S0 Gear S60	500 1000 : 4500 5000

mean spiral angle. The tests on the different gear geometries were performed under air-only conditions with rotational speeds of up to 5000 rpm. As previously described, the gear's contribution to overall power loss is found by subtracting shaft losses from total system losses.

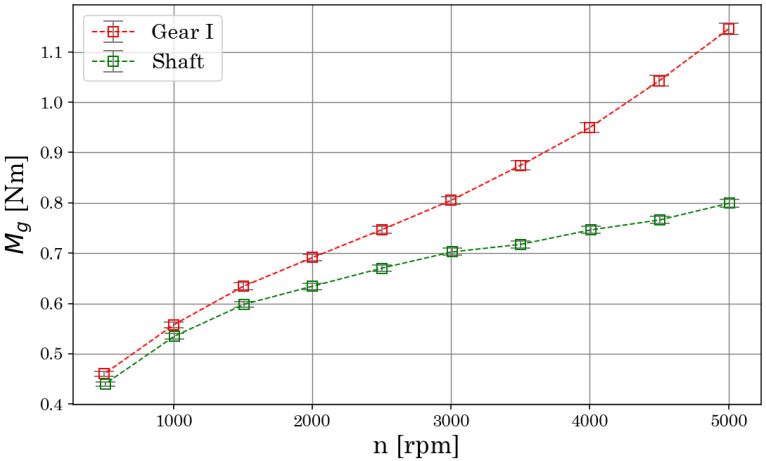

Figure 4.1: Comparison windage power losses between shaft and Gear I

Figure 4.1 illustrates the torque losses of the shaft and Gear I as a function of rotational speed, including the corresponding error bars. As Figure 4.1 shows, the power losses of the shaft and Gear I are comparable

at low speeds. This occurs because at low speeds, windage losses are very low. Fig.4.2 presents the experimental results obtained for Gears I and II, which differ only in gear width.

As shown in Fig.4.2, windage effects become progressively more pronounced as rotational speed increases, which is in agreement with findings reported in the literature [19]. Specifically, the slope of the curve above 3000 rpm clearly indicates the progressive contribution of windage effects, which lead to increased power losses at higher speeds given that windage losses increase proportional to ω^3. A comparison of Gear I and Gear II shows that both cases exhibit similar power loss increases with rotational speed. However, Gear II consistently exhibits higher losses due to its greater tooth width. Since Gears I and II operate at the same peripheral velocity, Fig.4.2 suggests that the observed difference is primarily due to the increased face width. This result is consistent with the direct influence of face width on windage power losses reported by Voeltzel et al. [20].

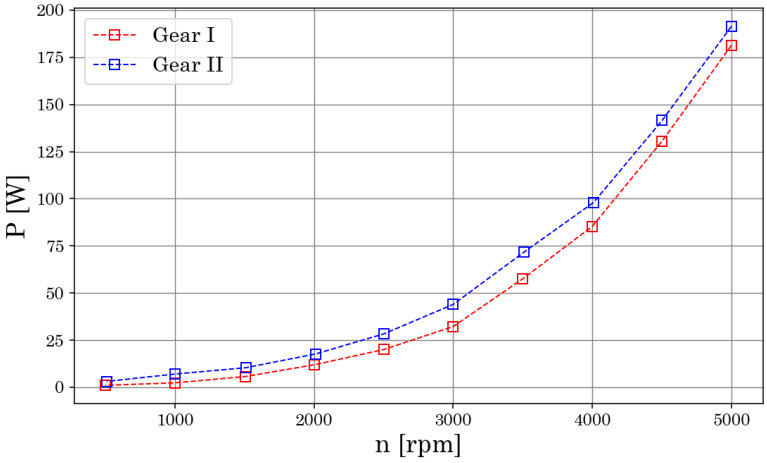

Figure 4.2: Comparison windage power losses between Gear I and Gear II.

The results for spiral bevel gears with different pitch cone angles are shown in Figure 4.3, while Figure 4.4 shows the results for different mean spiral angle. Windage power losses gradually decrease as the pitch cone angle increases. This behavior is consistent with the numerical simulation results reported in Webb's thesis [26]. Additionally, larger spiral angles result in lower windage power losses. As shown in Figure 4.4, it was also observed that the variation in windage power losses due to changes in spiral angle is more pronounced than that caused by changes in pitch cone angle. These results align with those in the literature [27].

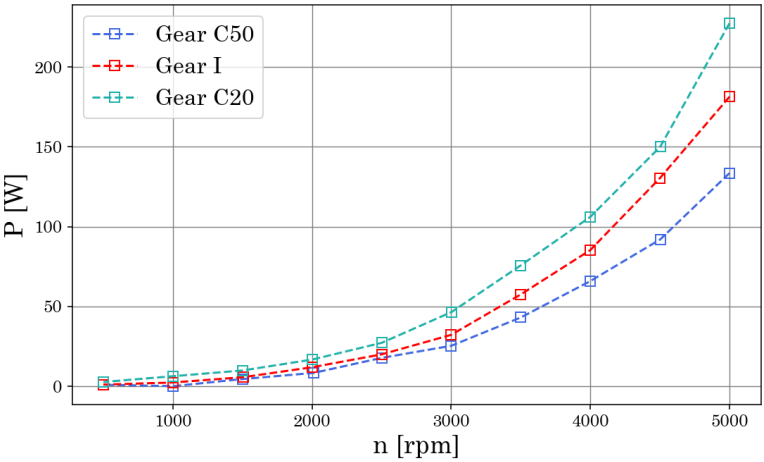

Figure 4.3: Comparison windage power losses between Gear I, Gear C20 and Gear C50.

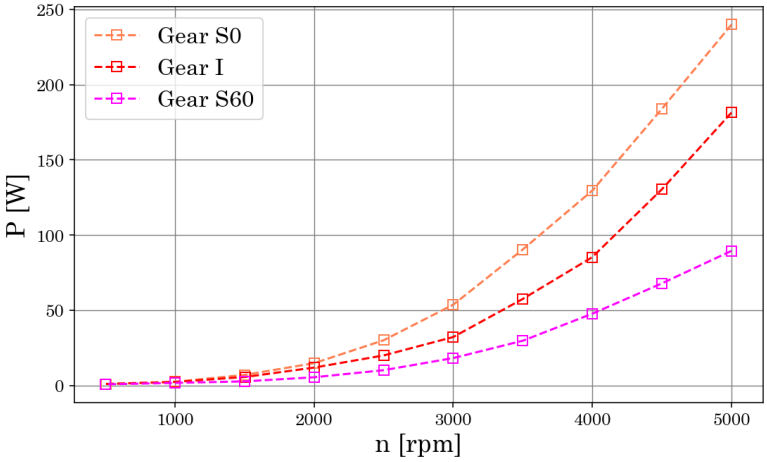

Figure 4.4: Comparison windage power losses between Gear I, Gear S0 and Gear S60.

4.1.1 Physical Model Validation

To validate the accuracy and applicability of the windage model proposed in section 3.3, the results obtained from Eq. 3.6 are compared with experimental measurements of windage power losses. The new predictive model for windage power losses was validated using experimental results that included all data obtained for various gear geometries. This was done to assess the model's sensitivity to the characteristic parameters of spiral bevel gears, such as face width, pitch cone angle, and mean spiral angle. Figure 4.5, 4.6 and 4.7 illustrate these trends and include the error band for the experimental data. The overall error band was determined by propagating the uncertainties associated with the subtraction, as described in the previous section 3.2.2.1.

Fig.4.5 4.6 and 4.7, show that the correlation effectively captures the behavior of power losses for all the gears considered. Not only does it qualitatively reproduce the increase in losses with rotational speed, but it also provides good quantitative agreement. This is further supported

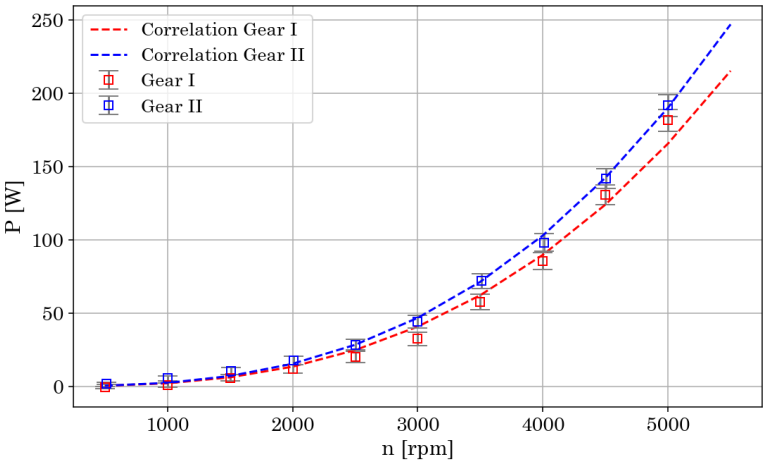

Figure 4.5: Comparison between the experimental data and physical model results for Gear I and Gear II.

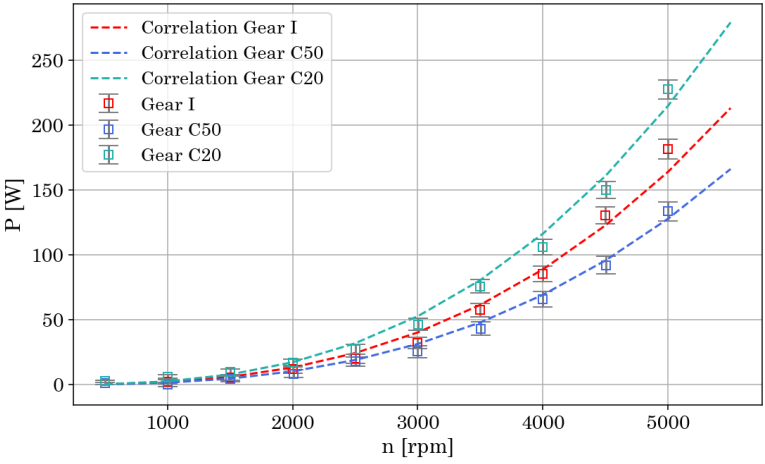

Figure 4.6: Comparison between the experimental data and physical model results for Gear I, Gear C20 and Gear C50.

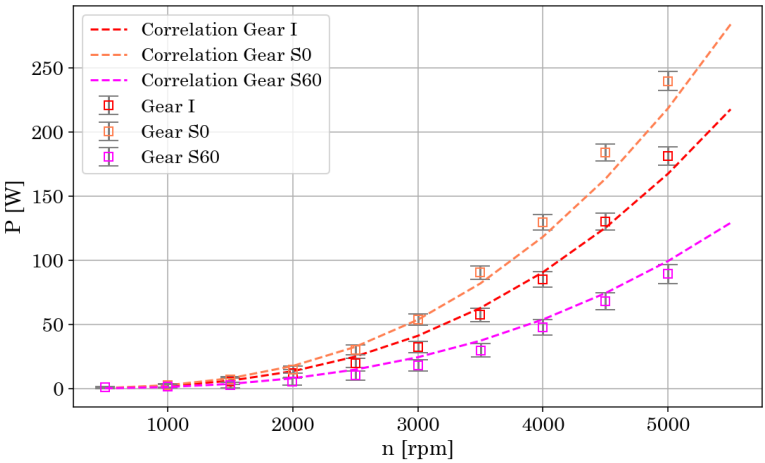

Figure 4.7: Comparison between the experimental data and physical model results for Gear I, Gear S0 and Gear S60.

by the fact that all values predicted by the physical model fall within the uncertainty range of the experimental measurements. Taken together, these results suggest that the physical model is consistent and reliable across all tested geometries. The proposed physical model shows a promising decrease in relative error compared to experimental measurements. It stabilizes at around 3% for all tested geometries at 5000 rpm. This reduction in relative error as rotational speed increases is encouraging for estimating windage power losses at operational speeds relevant to aeronautical applications.

4.2 Churning Power Losses

This section presents the experimental results obtained from the churning tests. The geometries described previously were employed for these tests in order to compare the results with respect to variations in face width, pitch cone angle, and mean spiral angle. A comparison of torque losses was also performed for the Gear I and Gear II as a function of the oil immersion level. Three immersion levels were considered: $h/h_t = 1$, which corresponds to the full height of the immersed tooth; $h/h_t = 2/3$, which corresponds to two-thirds of the tooth height; and $h/h_t = 1/3$, which corresponds to one-third of the tooth height. See Figure below 4.8. The tests were conducted at an oil temperature of 32°C. A further analysis of power losses for Gear I and Gear II was conducted using two oils with different properties, as shown in the Table below, Tab.4.3. In Table 4.2 are reported all test conditions investigated for churning test campaign. Finally, the experimental results were compared to a correlation found in the literature.

Table 4.2: Churning test conditions.

	Geometry	**Speed [rpm]**	**oil level** $[h/h_t]$	**Oil type**
Churning	Gear I Gear II Gear C20 Gear C50 Gear S0 Gear S60	500 1500 2500 3500 5000	1 2/3 1/3	Aeroshell 500 Aerogear 823

As for the windage test, a specific test procedure was adopted in order to isolate the contribution of churning power losses. First, the torque was measured during operation under oil-bath conditions at a given rotational speed. Then, the oil bath was drained through the discharge holes and the no-load torque was recorded. The difference between these two measurements allows us to determine the contribution of churning

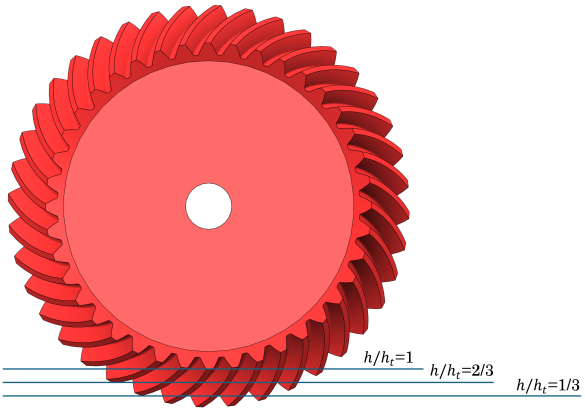

Figure 4.8: Oil level immersion depths for churning tests.

Table 4.3: Oil properties

	Aeroshell 500	Aerogear 823
Type	synthetic	mineral
Kinematic viscosity at $40°C$ $[mm^2/s]$	25.26	63.3
Kinematic viscosity at $100°C$ $[mm^2/s]$	5.17	8.36
Density at $20°C$ $[Kg/m^3]$	993	867

losses exclusively. Figure 4.9 shows an example of this procedure.

The oil bath temperature was maintained at approximately $32°C$ throughout the tests. The temperature variation during each test was monitored and remained within $\pm 1°C$. Since oil viscosity decreases with increasing temperature, this variation results in a change in viscosity. Such variations in viscosity can affect the measured torque loss, as the latter depends on the viscous interaction between the oil and the rotating components. However, given the limited temperature range observed during the tests, the effect is expected to be relatively small. Nevertheless, it may become more relevant at higher power losses and is therefore taken

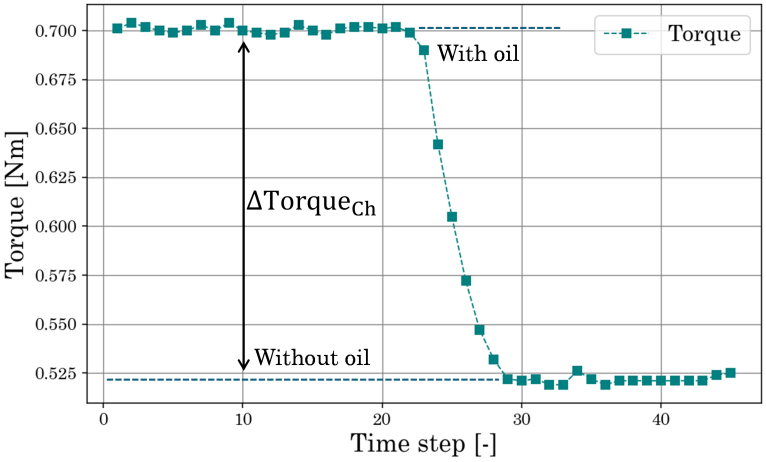

Figure 4.9: Churning post-process method.

into account when interpreting the experimental results. Figure 4.10 and 4.11 show an initial result, where the power trend is reported as a function of the rotational speed of Gear I and Gear II, respectively, for three different oil bath levels. The oil used is the Aeroshell 500 for both case. As expected, power losses decrease with decreasing oil level.

The graphs from the previous figures (4.10 and 4.11) are also presented as a function of torque and rotational speed (4.13 and 4.14) because this representation highlights an interesting trend. Regardless of gear geometry, lubricant type, or immersion conditions, particular drag torque behavior well known in the literature, was observed. Specifically, the torque initially increases with rotational speed until it reaches a local maximum. It then decreases to a local minimum before increasing again at higher speeds. Similar reductions in torque at speeds above 2000 rpm have been reported in experiments by Jeon [43], Laruelle [33], and Quiban et al. [10]. This decrease occurred due to the dynamic evolution of oil immersion as a result of a local decrease in immersion depth.

A direct comparison between Gear I and Gear II is presented in

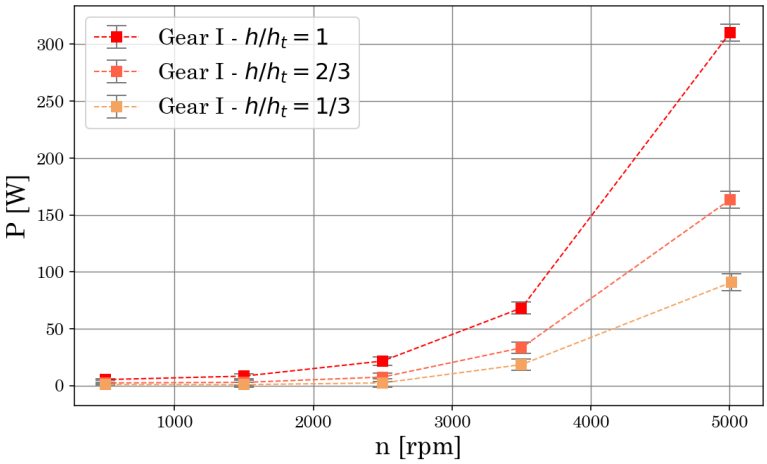

Figure 4.10: Comparison churning power losses for Gear I at different oil levels. Oil used Aeroshell 500.

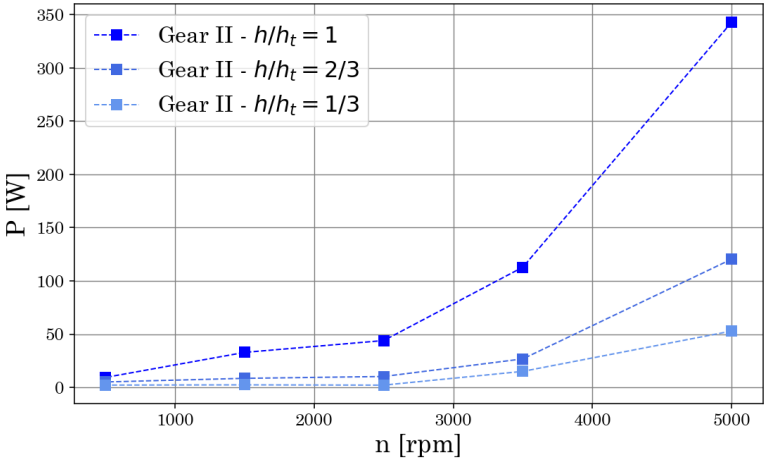

Figure 4.11: Comparison churning power losses for Gear II at different oil levels. Oil used Aeroshell 500.

Fig. 4.12, which shows the variation of torque losses as a function of rotational speed for the $h/h_t = 1$ immersion level. It is evident that the higher torque losses observed for Gear II are attributable to its larger face width. Additionally, it can be seen that the local minimum for Gear II shifts toward higher rotational speeds due to its larger face width. Furthermore, Fig.4.13 and 4.14 show that at higher oil immersion levels lead to greater local maximum torque values, which are also shifted toward higher rotational speeds. This result is consistent with the findings reported by Quiban et al. [10]. Figure 4.15 shows that the relative maxima corresponding to different oil levels occur at the same rotational speeds for Gear I with Aerogear 823 oil as for Gear I with Aeroshell 500 oil. This suggests that the rotational speed at which the local maximum torque occurs is more strongly influenced by the gear immersion level than by the lubricant type. This observation again agrees with the results reported by Quiban et al. [10]. However, the magnitude of the local minimum depends on the oil's properties. Specifically, it can be observed that the local minimum reached with more viscous oil (Aerogear 823) is smaller in absolute value than with less viscous oil (Aeroshell 500).

This result is also confirmed in Figure 4.16 and Figure 4.17, for Gear I and Gear II, respectively, where a direct comparison between the two oils is presented under the same operating conditions and at the oil level $h/h_t = 1$. Consistent with results in the literature, churning power losses are higher for Aerogear 823 due to its greater viscosity. However, at lower rotational speeds, the trend reverses, occurring at the same speed at which a local minimum appears in the torque curve, (at 1500 rpm for Gear I and 2500 rpm for Gear II, Fig.4.13 and 4.14). This behavior is attributed to the phenomenon of a local decrease in immersion depth, which is more pronounced in the case of Aerogear 823 because of its more viscousity.

By comparing the geometries that differ in terms of pitch cone angle, two main observations can be made, see Fig. 4.18 and 4.19. First, Gear C20, characterized by a smaller pitch cone angle, exhibits lower torque losses. This indicates that, for spiral bevel gears, torque losses decrease as the pitch cone angle decreases, which is opposite to the trend previously

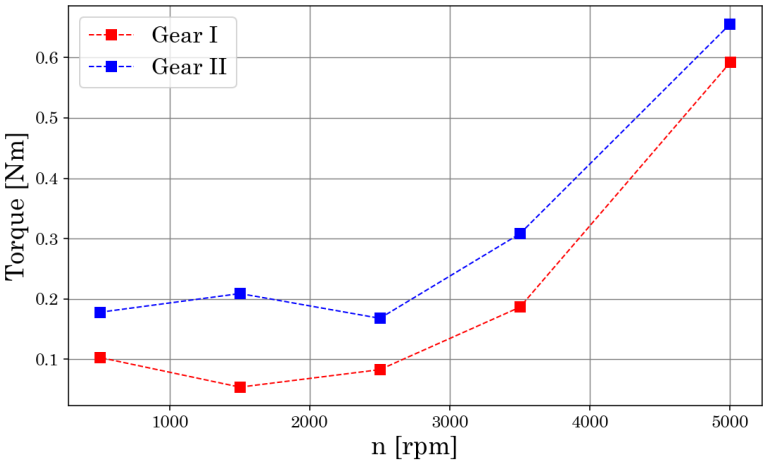

Figure 4.12: Influence of geometric width on the evolution of torque, Gear I and Gear II with oil level $h/h_t = 1$. Oil used Aeroshell 500.

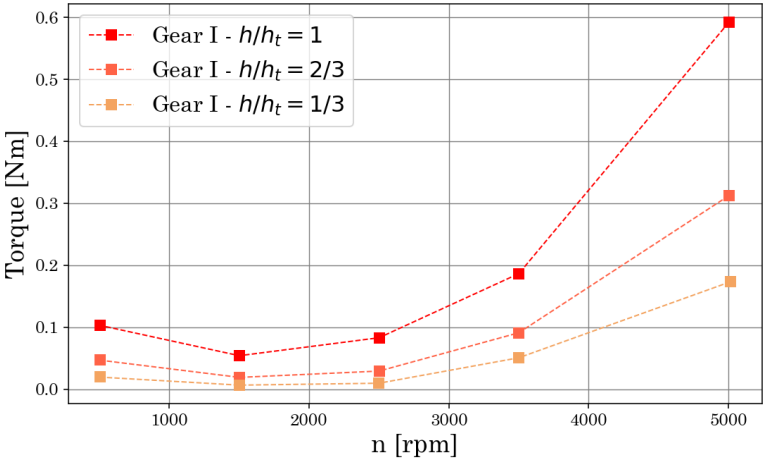

Figure 4.13: Influence of immersion depth on the evolution of torque, Gear I. Oil used Aeroshell 500.

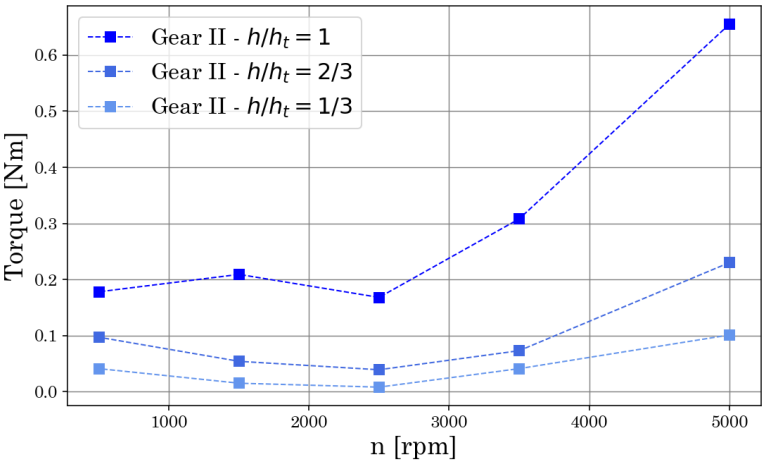

Figure 4.14: Influence of immersion depth on the evolution of torque, Gear II. Oil used Aeroshell 500.

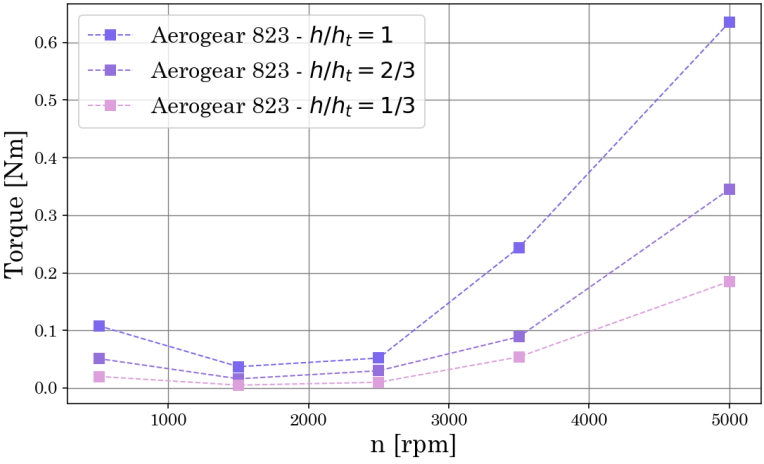

Figure 4.15: Comparison churning power losses for Gear I at different oil levels. Oil used Aerogear 823.

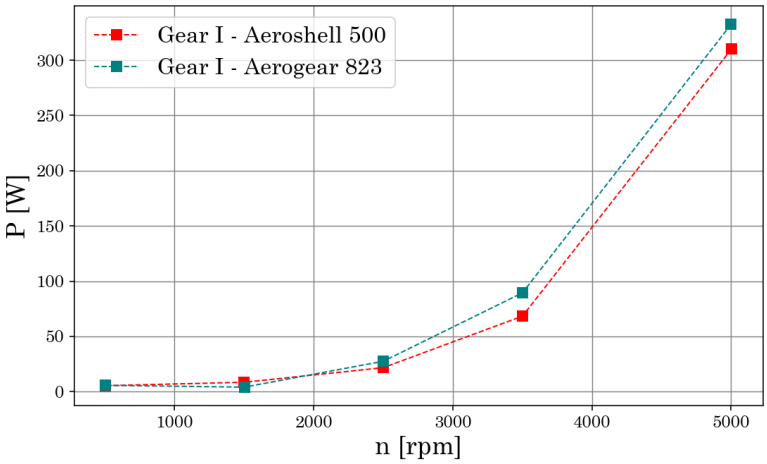

Figure 4.16: Influence of oil type on the evolution of churning power losses for Gear I and with oils at 32°C.

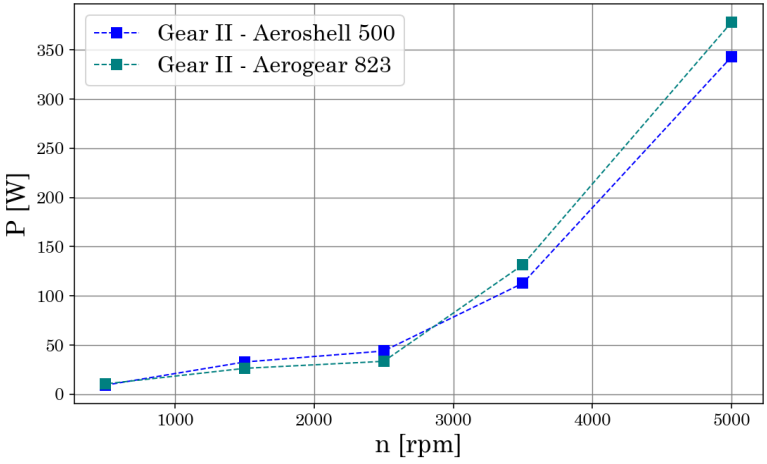

Figure 4.17: Influence of oil type on the evolution of churning power losses for Gear II and with oils at 32°C.

observed for windage losses. This behavior is due to the reduced wetted surface of a gear with a smaller cone angle, which leads to decreased churning effects. Second, as the pitch cone angle decreases, the minimum torque shifts toward lower rotational speeds. A similar trend was observed when the face width of the gear was decreased.

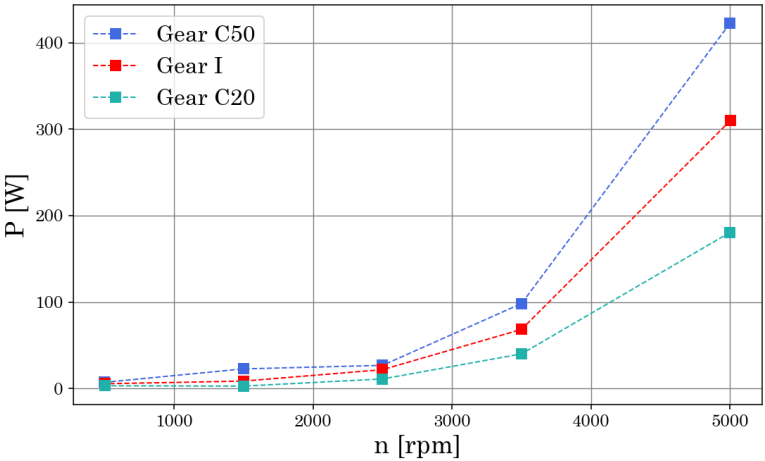

Figure 4.18: Comparison churning power losses for Gear I, Gear C50 and Gear C20.

By comparing geometries with different mean spiral angles, see Fig.4.20 and 4.21, we can observe that this parameter exhibits different trends in churning loss cases. Specifically, the influence of the tooth inclination angle on churning power losses appears to be less significant than that of the pitch cone angle. Gear S60, for example, shows lower churning losses than Gear C20, which highlights an opposite trend compared to that observed for variations in the pitch cone angle. This behavior can be explained by considering the wetted surface, which differs among the three configurations. Specifically, the wetted surface is smaller for Gear S60 and increases as the swirl angle decreases, resulting in higher churning losses.

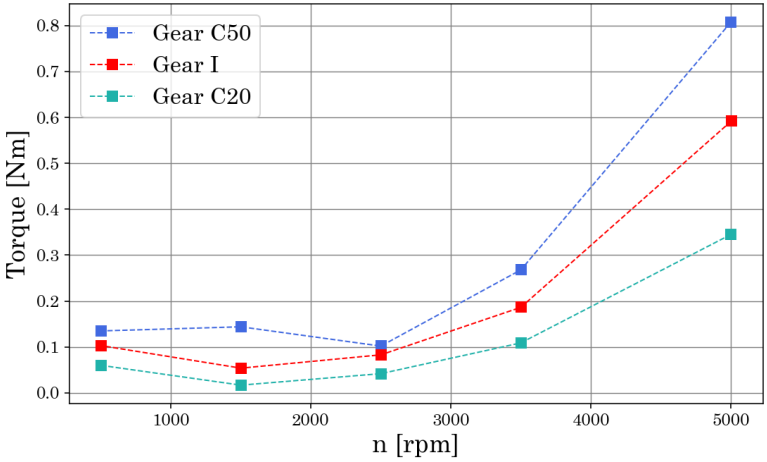

Figure 4.19: Influence of pitch cone angle on the evolution of torque.

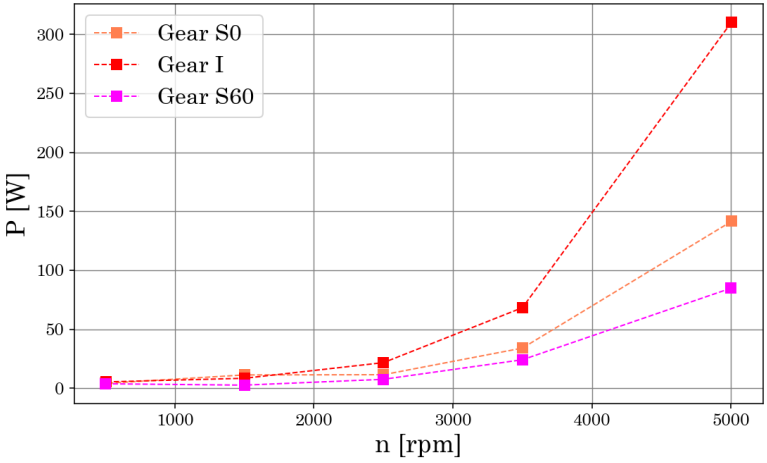

Figure 4.20: Comparison churning power losses for Gear I, Gear S0 and Gear S60.

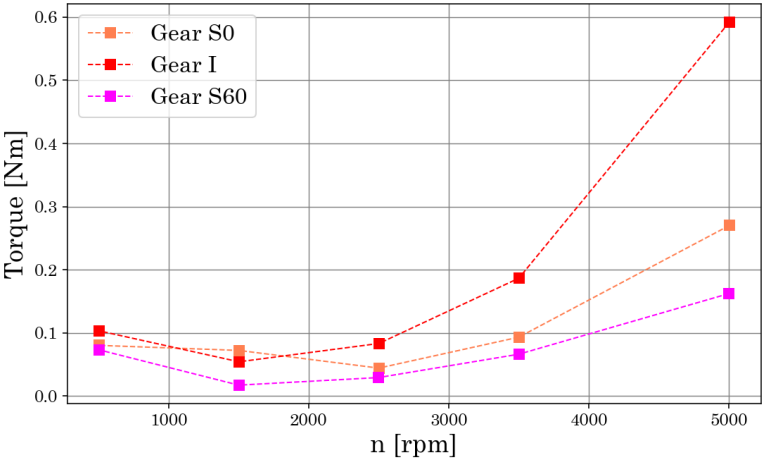

Figure 4.21: Influence of mean spiral angle on the evolution of torque.

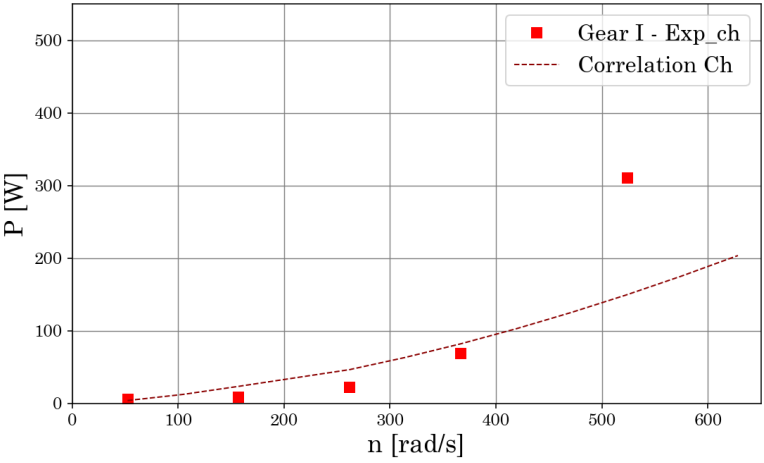

Figure 4.22: Comparison between correlation and experimental results for churning.

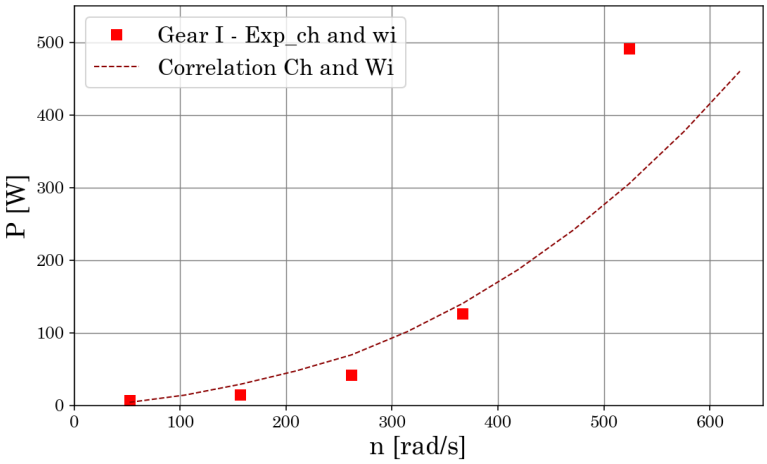

Figure 4.23: Comparison between correlation and experimental results for churning.

Finally, a comparison was made between the experimental data and that predicted by a correlation, accounting for both churning and windage contributions to power losses. For the churning part, the literature correlation of Jeon [43] was used adapted by the dynamic immersion depth model of Quiban et al. [10]. The correlation developed as part of this work, as an adaption of the correlation of Diab [19] was used for windage part. Results are shown for Gear I, in Figure 4.22 for only churning losses, P_{Ch} and in Figure 4.23 for the total losses $P_{tot} = P_{Ch} + P_{wi}$. Up to highest velocity tested of 5000 rpm, the experimental trend is well predicted in both cases. Considering both Figures, it can be seen that the large under-prediction of the experimental total power loss is almost exclusively due to the under-prediction in churning losses by the correlation of Jeon. This is attributable to the fact that the Reynolds number at the highest speed is outside the range of applicability of the correlation. In particular, the exponent of the Reynolds number of -0.25 in Jeon's correlation (see Eq.2.32) does not accurately describe the

experimental trend with increasing speed at the high Reynolds numbers corresponding the maximum speed investigated in this study. To check that this is indeed the case, the Aeroshell 500 and Aerogear 823 test cases characterized by identical gear geometry, oil levels and tested speeds allowed to estimate the Reynold number exponent of the present data. This is possible because the only difference between the test cases are the oil viscosity and the density. Equation 2.33 was used to calculate the Reynolds number exponent for all tested speeds, removing the dependence of density by fist calculating the moment coefficient C_m, using Eq. 2.31. For every velocity except 5000 rpm the value of -0.25 was confirmed while for 5000 rpm the value was slightly less negative. This explains the under-prediction in the Churning torque.

4.3 Velocimetry

In this section results will be presented from velocimetry test campain. First, windage velocity measurements are shown in a time averaged sense since they are not characterized by a significant periodic component. By contrast churning results are presented first in a time average sense and then in a phase average sense thanks to the POD-based phase-ordering procedure presented in section 2 to highlight the periodic nature of churning phenomenon. The test conditions are reported in Table 4.4.

Table 4.4: Velocimetry test conditions.

	Geometry	**Speed [rpm]**	$V_{tan}[m/s]$	**oil level** $[h/h_t]$	**Oil type**
Velocimetry	Gear I Gear C20 Gear C50 Gear S0 Gear S60	500 1000 1500	6.15 12.6 18.45	1 1/3	Aeroshell 500 Aerogear 823

4.3.1 Windage

Windage measurements were performed using the PIV setup, described in the Chapter 3. Figure 4.24 shows the time averaged windage velocity fields calculated from 438 image pairs recorded for Gear I at 500 rpm in an air only environment. In the plots the gear is masked, with the radius of the mask corresponding to the radius at which the laser sheet intersects the gear, and the velocity magnitudes have been normalized using tangential velocity. The velocity magnitudes adjacent to the mask demonstrate that the tangential velocities of the gear are calculated accurately for the 500 rpm case, with the nominal tangential velocity of the gear shown in Table 4.4. Outside the external diameter of the gear the Figure shows much lower air velocities relative to the gear tangential speed. In general the flow direction follows the anticlockwise rotation of the gear with a maximum occurring above and to the right of the gear.

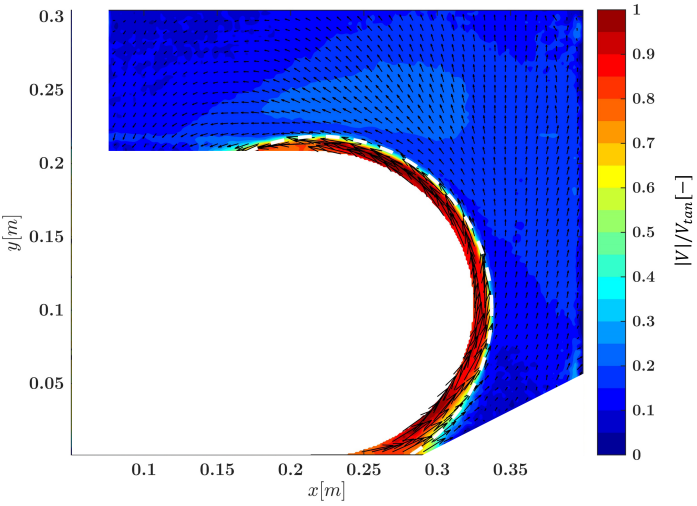

Figure 4.24: Windage PIV result for Gear I at 500 rpm.

This is qualitatively similar to the CFD result, used to estimated windage losses, discussed in Section 3.3. An analogous velocity field to the experimental one is shown in Figure 3.8. This simulation was carried out with a rotational speed of 3500 rpm. Although the gear speeds are different, the simulation captures similar flow behavior inside the chamber. As described previously in Chap.3, the laser sheet is obstructed by the gear; therefore, it is not possible to obtain PIV measurements in the bottom-left zone of the chamber. Similarly, PIV measurements cannot be obtained in the bottom-right corner, as the limited dimensions of the lateral optical access prevent the laser sheet from reaching this region.

4.3.2 Churning

During the churning test campaign, acquisitions by the PIV system described in section 3 were made to calculate the oil velocity fields on the mid-width plane of the tested gears. The results were used to analyze the behavior of the oil flung by the gear above the bath with varying gear geometric parameters, speeds, oil levels and oil properties.

4.3.2.1 Average PIV Results

Average velocity fields were first calculated through traditional PIV method, that is, with no considerations made regarding the oil distribution which acts as the seeding particles for the PIV measurements. Figure 4.25 shows the average velocity field obtained from 438 image pairs for Gear I at three different speeds with Aeroshell 500 at an immersion depth of $h/h_t = 1$. The velocity field is normalized by the tangential velocity of the gear. In the plots the gear is masked, with the radius of the mask corresponding to the radius at which the laser sheet intersects the gear. The velocity magnitudes adjacent to the mask demonstrate that the tangential velocities at each speed, shown in the Table 4.4, of the gear are calculated accurately. The white line indicates the outer pitch diameter of the gear; therefore the velocities outside this line correspond to the oil projected by the gear. Considering the low speed, the velocity

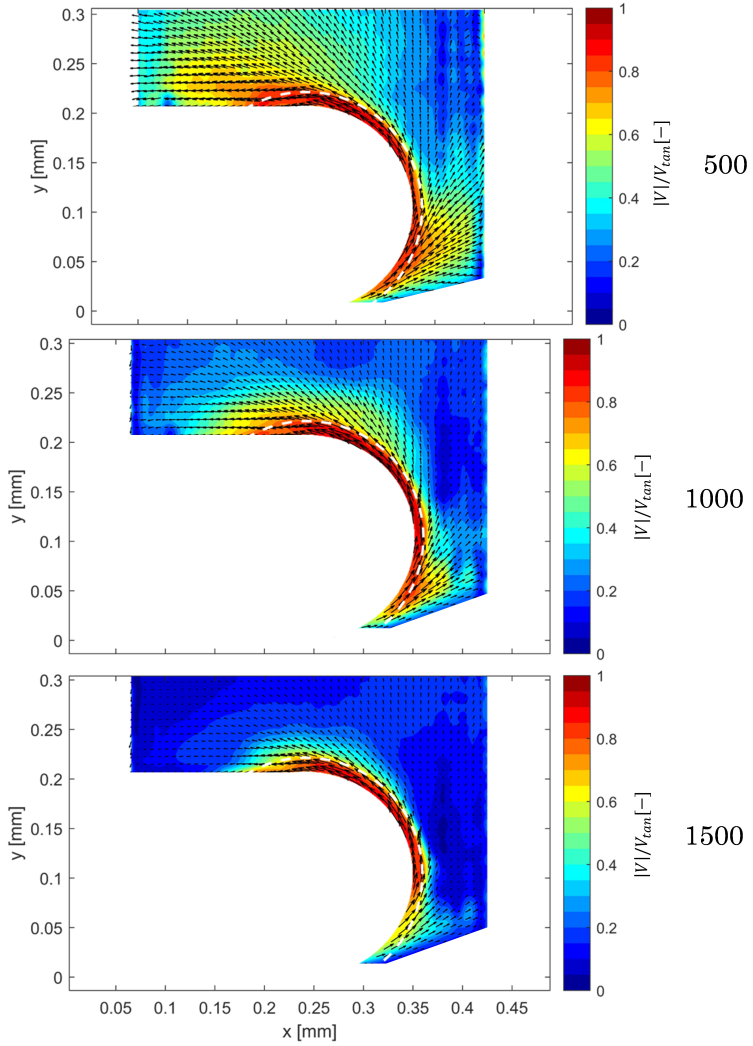

Figure 4.25: PIV average velocity magnitude with vectors of Gear I for three different speeds.

magnitude and direction in the lower right side of the gear is indicative of the oil jet formed as the teeth emerge from the bath. Following the anti-clock wise sense of rotation a low velocity zone appears to the right of the gear which is succeeded by a zone of higher velocity above the gear. The low illumination caused by the shadow of the gear on the left side of the plot reduces the accuracy of the measurements. The velocity in this zone will not be considered in the following analysis and in the velocity field plots, it has been masked. The sheet of oil attached to the oil bath in the bottom right of the plots has been masked as well, since it is a continuos feature present in the same position in essentially all instantaneous acquisitions and is thus difficult to measure with PIV. As the velocity increases the extent of the regions outside the external diameter of the gear, characterized by elevated velocities decreases. In fact, for the highest velocity it can be seen that PIV, outside the gear, measures a very low velocity of the flow field with respect to the gear tangential velocity. If one interprets these time average measurements in the sense of the traditional PIV method, the conclusion could be made that the velocity of the oil relative to the tangential velocity of the gear decreases as the speed increases. However, as discussed in Section 3.5 applying the traditional PIV method to two phase flows where the dispersed phase is used as the seeding particles, can lead to unrealistic results for low dispersed phase density. This is due to the cross-correlation function which calculates a most probable displacement, and therefore a velocity vector for every IA of the instantaneous images. Since in this case the seeding is not introduced intentionally to create a uniform distribution such that significant light scattering occurs in each IA, the cross-correlation function may lack a sufficient information to accurately calculate the local velocities where seeding is less present or absent. Thus the measurements are in such a case influenced by the instantaneous distribution of dispersed phase. Considering the plots of Figure 4.25, while it is possible to identify zones of high and low velocity from the time-averaged results, it is not possible to say how much the velocities depend on the distribution of oil in the instantaneous images used to calculate the individual velocity fields.

4.3.2.2 Phase-Average PIV Results

As described in Section 3.5, in this work to limit the velocity measurements to only the oil phase, a velocity validation based on the pre-processed PIV images was used. To demonstrate the effectiveness of this approach an example of an instantaneous masked velocity fields is shown in the Figure 4.26, superimposed over its corresponding frame-1 PIV image. The Figure shows that the PIV measurements, initially present for every IA, have been effectively reduced to only those corresponding to the oil particles visible in the image.

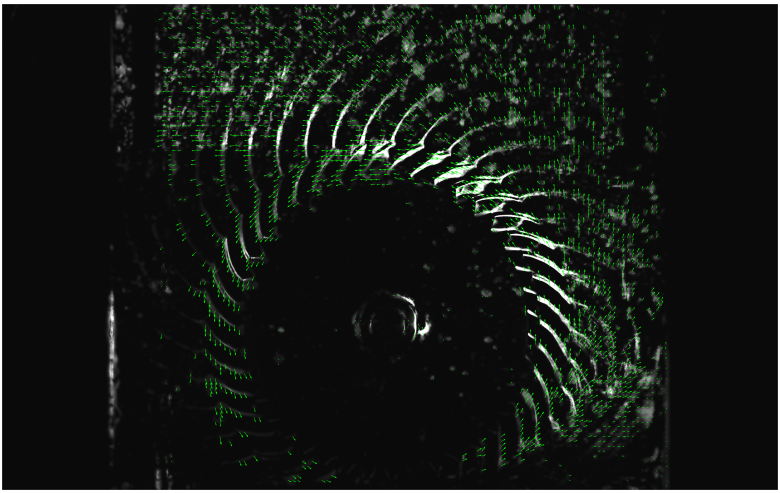

Figure 4.26: Instantaneous image with instantaneous velocity vectors.

To account for the unsteadiness of the churning phenomena, and to obtain more robust results, the velocity fields were phase-averaged using the POD-based phase-ordering procedure presented in Section 2.8. In order to apply the POD phase ordering, a verification that the low-order model of equation 2.68 captures the periodicity of the churning flow (with the period defined by the tooth-passing frequency) is demonstrated in Fig. 4.27. The results of the Figure correspond to Gear I at 500 rpm with

Aeroshell 500 at the largest immersion depth, but analogous results are found for all cases. This Figure is similar to the one found in the work of Oudheusden [66] and demonstrates that the phase angle of the individual velocity fields can be determined by the temporal coefficients of the first two POD modes. Once it was verified that this model could be applied to the present case, it was also checked that, after identifying the different phases, the gear teeth remained nearly stationary in the same position in all images belonging to a small interval of phase angles within the tooth passing period. Figure 4.28 shows the phase-averaged image (for the same test case as that of Fig.4.27) for a given phase obtained from the procedure, dividing the tooth passing period in 15 equally spaced intervals. Considering only the gear teeth the image appears to be an instantaneous one despite being composed of 27 snapshots. Also the oil filaments attached to each tooth appear well defined in space and give a robust visualization of the oil distribution within the phase angle interval shown. To calculate the phase-average velocities all instantaneous and validated velocity fields within the same phase angle interval were averaged together. This resulted in 15 phase intervals with approximately 30 instantaneous velocity fields within in each one.

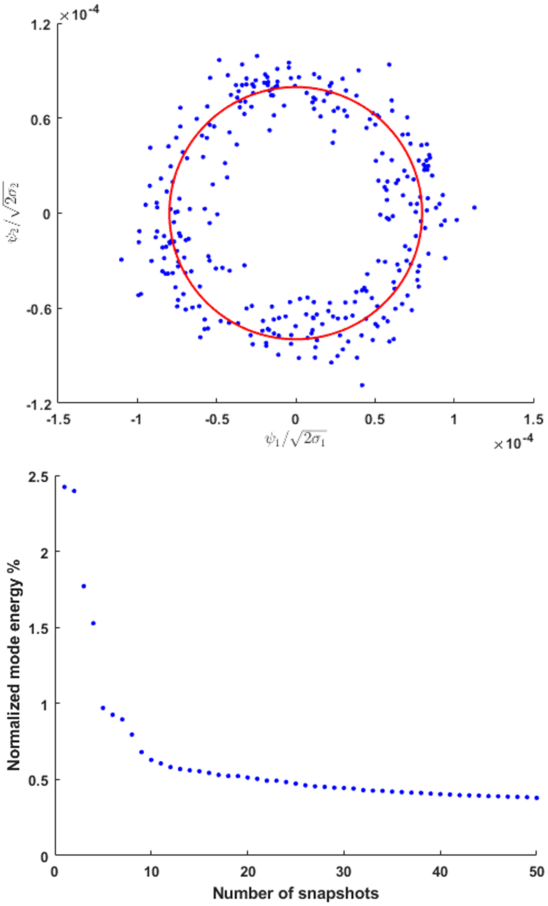

Figure 4.27: Mode coefficients correlation plot (top) and singular value plot (bottom).

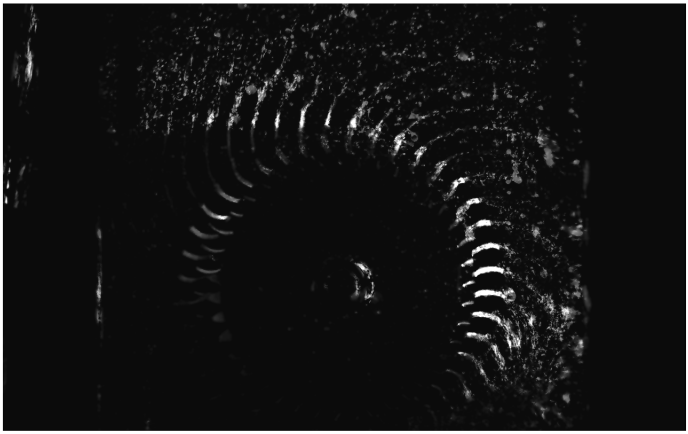

Figure 4.28: Phase-averaged image calculated from POD phase-ordering procedure.

The results obtained for the different cases studied are presented in the following sections. The first comparison considers Gear I operating at the high oil bath level ($h/h_t = 1$) at three different rotational speeds, namely 500, 1000, and 1500 rpm for Aeroshell 500 oil at the same temperature. Only a single phase is shown for each test case, but it was verified that little variation occurs from one phase to another in terms of oil distribution and velocity magnitude. The major difference between the phases is obviously that the gear rotates one full tooth-passing angle from the first phase to the last. The results, shown in Figure 4.29, highlight that at the lowest speed, oil filaments are present in the vicinity of the teeth over the entire investigation area. Adjacent to the teeth, the velocity magnitudes are consistent with those of the gear at the radius where the laser sheet crosses the teeth (indicated by the green dashed circle). Moving radially away from the gear, local filament break-up is observed above the gear at angular positions far away from where the gear teeth exit the oil bath (bottom right). The region adjacent to the oil bath, on the other hand, is characterized by a dense oil distribution with continuos and relatively

thick filaments of uniform velocity. The low-density, low-velocity zone in the far bottom right corner of the plot results from the fact that the gear tends to form a continuous sheet of oil connected to the oil bath in that position, thus yielding little measurement signal for the PIV algorithm. At the intermediate speed the oil filaments are limited to the region adjacent to the gear teeth. The high density of oil droplets in the upper left indicates more intense filament breakup (higher Weber number), as well as a more stochastic behaviour of the oil at this speed. By contrast, the filaments in the region near the oil bath remain relatively more continuous. At the highest speed, the oil filaments have nearly completely disappeared. In fact, very little oil is released from the teeth at any position, indicating that the gear passes through the oil bath without accumulating a sufficient amount on the tooth surfaces for significant release above the bath. An interesting trend is noticeable at the two lower speeds: oil is initially flung from the teeth at relatively high density and velocity before decreasing in the area above and to the right of the gear and then increasing again straight above the gear. This behavior may be due to the effect of gravity, being most disadvantageous to the oil particle motion in the area above and to the right of the gear where their trajectories are nearly vertically upwards, or it may be due to the dynamics of the oil flowing along the teeth and grooves as the gear rotates away from the bath where it is initially accumulated. Recalling the time-averaged flow fields of Figure 4.25, the trend of lower oil velocity relative to the tangential velocity of the gear with increasing speed may be explained by a lower density of oil in the flow field. This lower density is due to the lower accumulation of oil from the bath and a more rapid break up of the filaments as the speed increases. The comparison with the phase average results demonstrates that although the velocity magnitude of the different zones of the flow fields seem well predicted by time averaged results the phase average flow fields give additional information about the oil distribution.

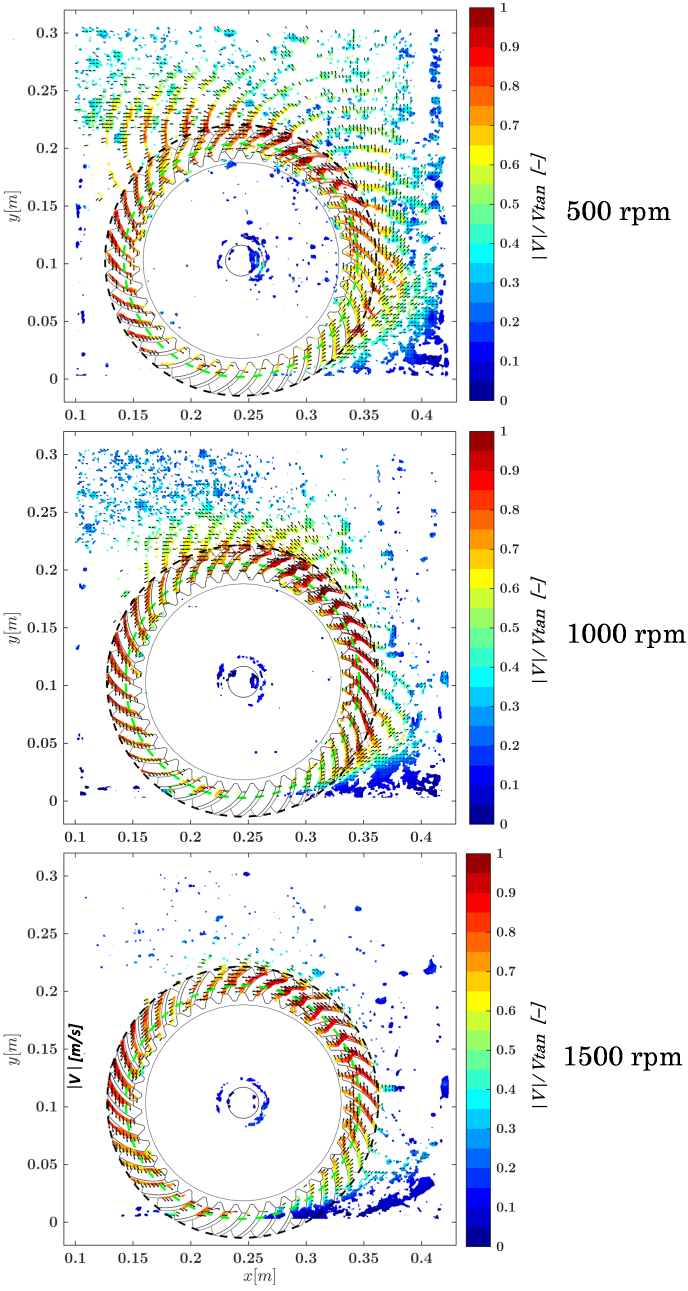

Figure 4.29: Phase-average velocity magnitude and vectors for Gear I for three different speeds.

Firgure 4.30 reports the velocity fields for three different cone angles 22, 36 and 52, respectively. The comparison shown considers the same rotational speed equal to 500 rpm and the same oil level ($h/h_t = 1$) using Aeroshell 500 at the same temperature. The oil particles demonstrate quite different behaviors with varying cone angle. First, the direction of the oil particles near the bath becomes more vertical, and their velocities decrease as the cone angle increases. Second, the distributions present some substantial differences. For Gear C20 the behavior previously discussed, where the velocity and particle density first decrease moving away from the oil bath before increasing again above the gear is particularly strong. By contrast, this behavior nearly disappears for Gear C50 as the oil density and velocity become more uniform throughout the investigated area. Regarding this aspect, Gear I can be regarded as a sort of intermediate case.

Figure 4.31 reports the velocity fields for three different mean spiral angle, 0, 31 and 60, respectively. The comparison shown considers the same rotational speed equal to 500 rpm and the same oil level ($h/h_t = 1$) using Aeroshell 500 at the same temperature. Compared to the effect of cone angle, oil particle behavior is relatively less sensitive to the swirl angle. Oil filament angle and orientation appears relatively unchanged by the swirl of the teeth with only slight variations in velocities.

Figure 4.32 reports the velocity fields of Gear I for two different oil level, the highest ($h/h_t = 1$) and the lower ($h/h_t = 1/3$) respectively. The comparison shown considers the same rotational speed equal to 500 rpm using Aeroshell 500 at the same temperature for both cases. For the low immersion depth, a significantly lower density of oil particles is present throughout the investigated area. However, regarding the spatial distribution of oil, the low-level case appears qualitatively similar to the high-level one. The exception is the zone above and to the right of the gear, which is characterized by a higher concentration of droplets with respect to the high-level case As expected, the angle of the particles flung from the oil bath decreases as the oil level decreases.

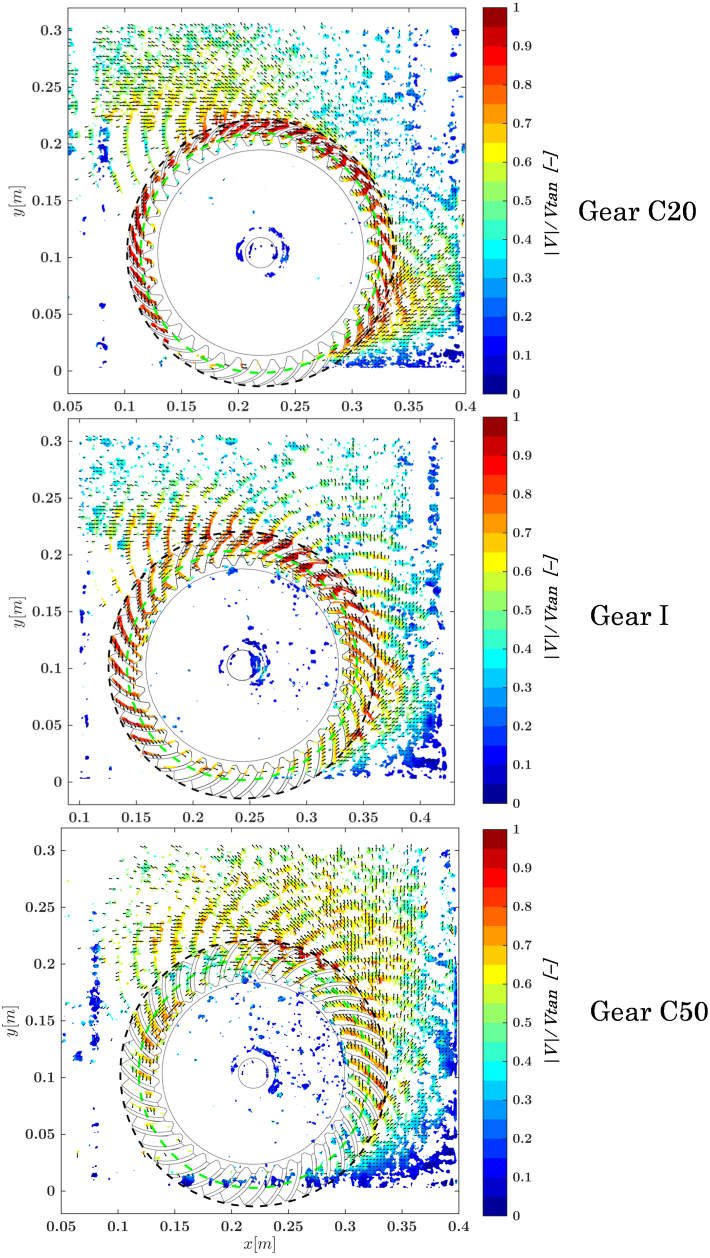

Figure 4.30: Phase-average velocity magnitude and vectors varying cone angle.

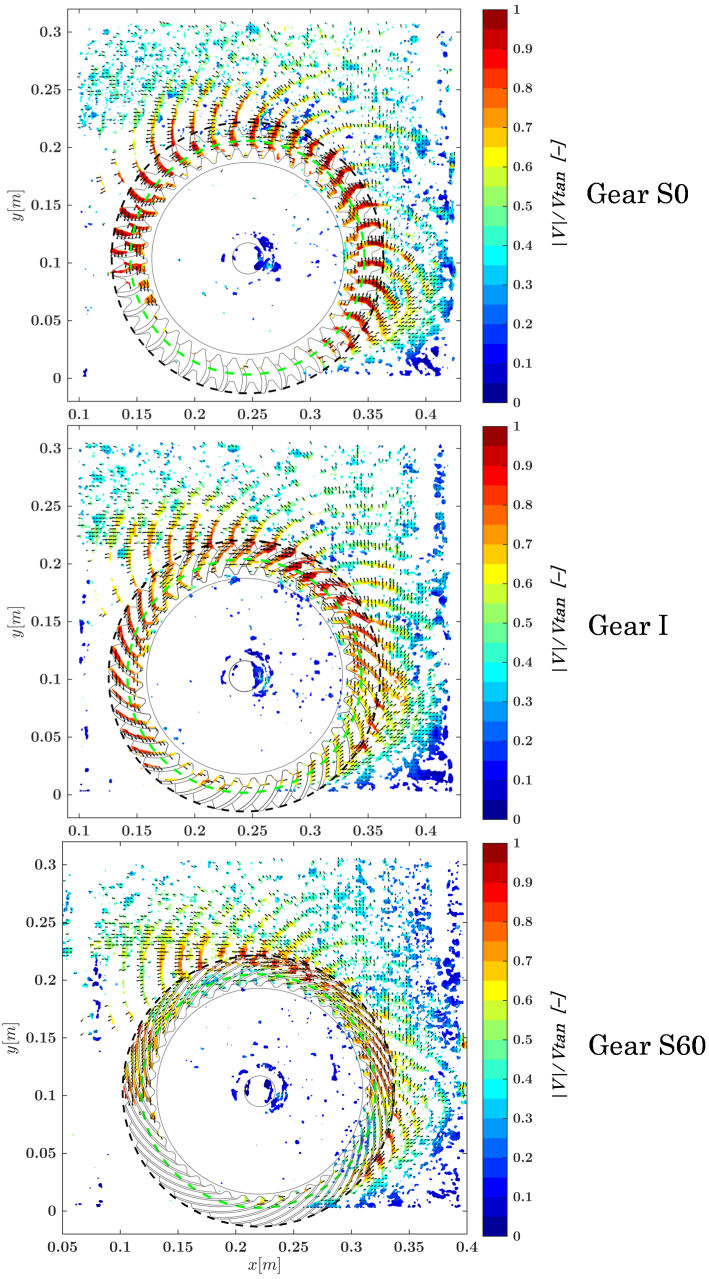

Figure 4.31: Phase-average velocity magnitude and vectors varying mean spiral angle.

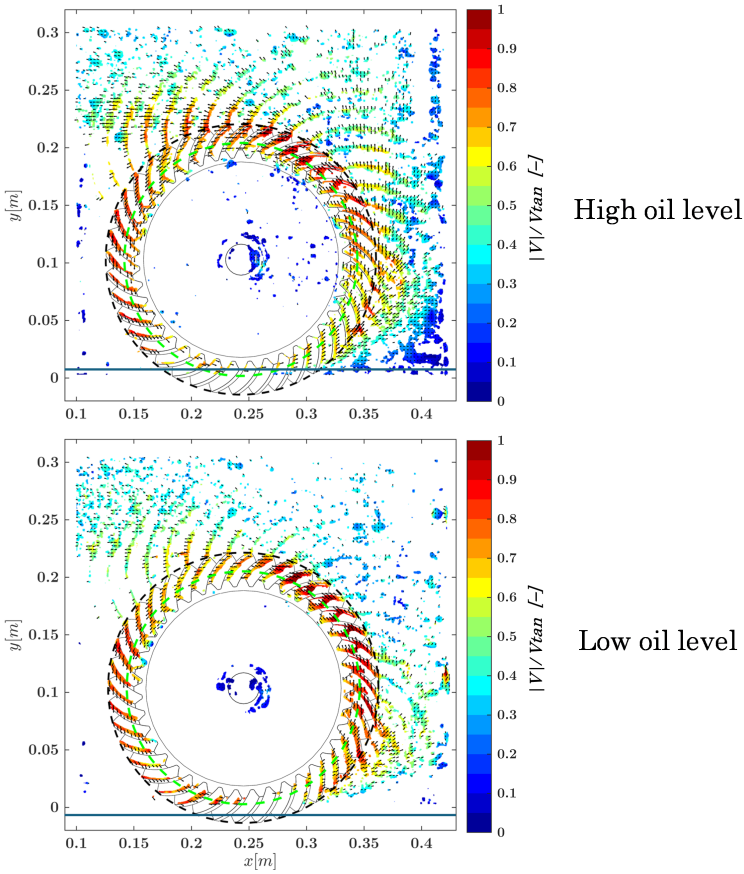

Figure 4.32: Phase-average velocity magnitude and vectors for high and low oil level of Gear I at 500rpm.

The last comparison is done for Gear I at three different rotational speed, 500, 1000 and 1500 rpm, at the same oil level ($h/h_t = 1$) and using two different oil (Aeroshell 500 and Aerogear 823). Figure 4.33 reports the velocity fields of this comparison and highlight that the oil particle behavior changes substantially with oil properties. The higher viscosity of Aerogear 823 with respect to Aeroshel 500 determines much higher densities and also higher velocities throughout the measurement area. Oil filaments are also more elongated as the higher viscosity of Aerogear 823 helps the filaments resist deformation and breakup. Even at the higher speed of 1000 rpm, filaments remain substantially more intact than for the Aeroshell 500 reference case.

In conclusion, the velocimetry and post-processing approach to study the particular phenomena of above-bath oil dynamics in splash lubricated spiral bevel gears was shown to be sufficient robust to identify the main differences in oil behaviour caused by the variation of parameters considered. The phase-averaged analysis clearly demonstrated changes both in distributions and velocities for different zones of the investigated area and highlighted trends with changing variables such as speed, oil level, oil characteristics and geometrical parameters of the gear. Such capability is challenging to achieve due to the highly unsteady nature of the churning phenomena and to the wide range of characteristic sizes, shapes, and densities of the dispersed phase oil above the bath to be analyzed. The methods used obtained these results seem a promising approach to compare experimental results to numerical simulations, in fact, phase average quantities may be calculated in the same manner from time-dependent CFD simulations. Comparing oil distributions and velocities would provide useful feedback to numerical models regarding the ability to capture oil behavior.

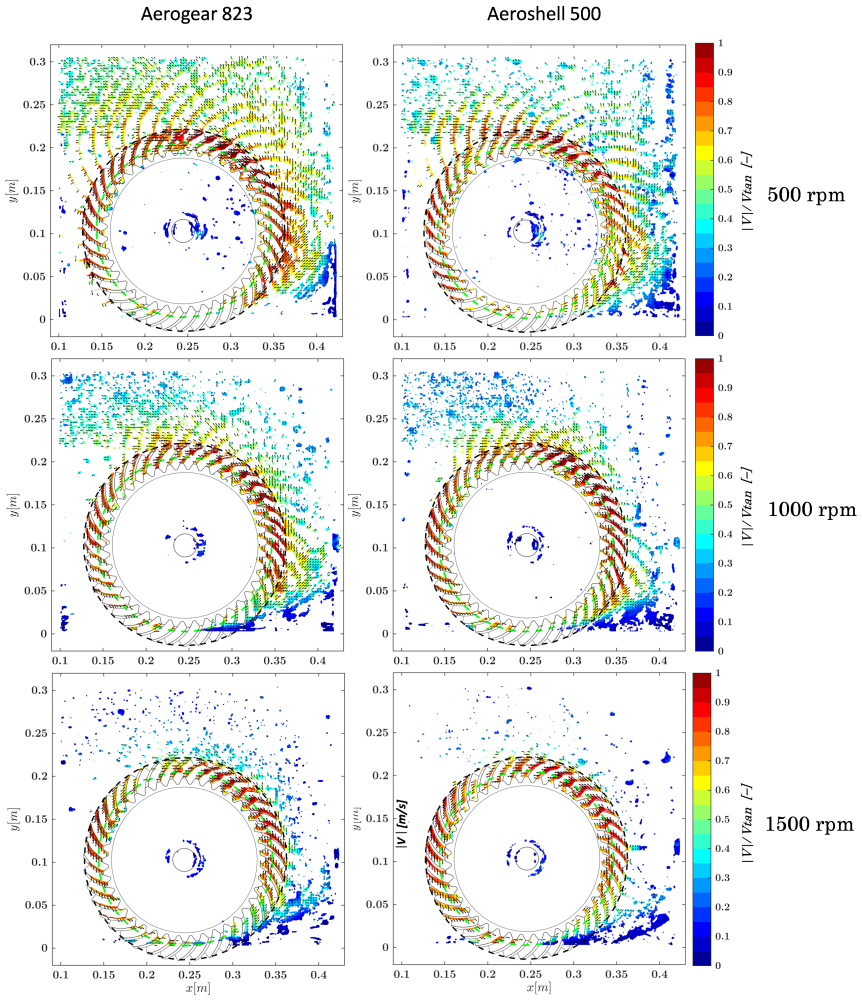

Figure 4.33: Phase-average velocity magnitude and vectors for different oils and velocities of Gear I.

Conclusions

This work compiles the activities performed during the Ph.D. project, focusing on power losses for spiral bevel gears. This concluding chapter presents the main findings of the investigation, offering an overview of the study and summarizing its main achievements. It also discusses the potential impact of these outcomes on future work.

A dedicated test rig was designed to study the churning power losses of spiral bevel gears under splash lubrication conditions at high rotational speeds. New spiral bevel gear geometries were designed and 3D-printed in Onyx to study the influence of different geometric parameters, such as pitch cone angle, mean spiral angle, and face width, on power losses.

The initial phase of the experimental campaign focused on analyzing windage losses for a single spiral bevel gear operating in an air-only environment. Although the pitch diameter is one of the most influential parameters on windage losses, experimental results showed that the pitch cone angle and the mean spiral angle are also critical factors. In fact, the results show that windage losses decrease as both the cone angle and the mean spiral angle increase. Additionally, the change in windage power losses caused by spiral angles is more noticeable than that caused by pitch cone angle.

Additionally, a physical model for spiral bevel gears was proposed and derived from a reformulation of an existing model that was originally developed for windage power losses in spur gears. The model proposed was developed to account for the main geometric parameters of spiral bevel gears, including not only the pitch outer diameter, number of teeth,

and face width, but also the pitch cone angle and the mean spiral angle. Thanks to different geometries designed, this new physical model was successfully validated and demonstrated a promising trend of decreasing relative error with increasing speed for all configurations tested. These results suggest the model's potential for estimating windage losses in spiral bevel gears.

After testing gears with different geometric characteristics for windage power losses, the next step was to evaluate churning losses, which are closely related to windage behavior. Thus, the initial phase was preparatory to the subsequent analysis of churning losses, providing a comprehensive framework for understanding fluid-dynamic losses in high-speed gearing systems.

Churning tests were carried out under different operating conditions, varying the rotational speed, the oil bath level, and the type of lubricant, using two oils with different viscosity and density properties. The oil bath temperature was kept constant at around $32°C$ throughout all tests. The results clearly showed that churning losses strongly depend on the portion of the gear immersed in the oil. Furthermore, geometric parameters, particularly the cone angle and the mean spiral angle, also have a significant influence on the immersed surface and so also on the churning losses. In fact, increasing the cone angle the churning power losses increase. During these tests, a particular drag torque behavior was observed, in agreement with the literature. In fact, regardless of gear geometry, lubricant type, or immersion conditions, the torque initially increases with rotational speed until it reaches a local maximum and then decreases to a local minimum before increasing again at higher speeds. This trend occurs due to the dynamic evolution of oil immersion level that lead to a local decrease in immersion depth.

Finally, measurements of velocimetry were carried out using PIV method to study and analyze the behavior of the oil flung by the gear above the bath with varying gear geometric parameters, speeds, oil levels and oil properties in splash lubricated spiral bevel gear. Firstly, velocity fields were calculated in terms of time-average results. Since in this case

the traditional PIV method was applied to two phase flow where the dispersed flow was used as a seeding, this approach can lead to results where it is possible to identify zones of high and low velocity but it is not possible to say how much the velocities depend on the distribution of oil in the instantaneous images used to calculate the individual velocity fields. Subsequently, a different approach, based on phase-average analysis, was applied to limit the velocity measurements to only the oil phase and to enhance the robustness of the measurement to identify the main differences in oil behaviour caused by the variation of the parameters considered. These results are a challenge to achieve due to highly unsteady nature of the churning phenomena and to a non uniform distribution of the dispersed phase oil above the bath to be analyzed. However, these methods seem a promising approach to compare oil distributions and velocities obtained from numerical simulations with experimental results in order to improve their ability to capture oil behavior in splash lubrication systems.

List of Figures

1.1 General gearbox power losses [2] 2
1.2 Principle of a helicopter drive train [5] 4
1.3 Niemann -Winter model for oil viscosities [7] 5

2.1 The active surface of the teeth is considered in the definition of the tooth coefficient [19]. 19
2.2 Windage power losses for a spur gear varying the rotational speed: comparison between the results obtained by the formulas of Anderson and Loewenthal, Dawson, Diab and Dorfman for a Rotating disk. 20
2.3 Windage power losses for a spur gear varying the pitch diameter: comparison between the results obtained by the formulas of Anderson and Loewenthal, Dawson, Diab at 5000 rpm. 21
2.4 Windage power losses for a spur gear varying the gear face width: comparison between the results obtained by the formulas of Anderson and Loewenthal, Dawson, Diab at 5000 rpm. 21
2.5 Schematic of the geometric parameters of an oil-bath lubricated gear. 25
2.6 Photo of the submerged part of a straight cylindrical gear rotating in a bath of distilled water, clockwise rotation. $h_R = 0.20$, $\nu = 1$ cSt, a) $V_T = 0.5$ m/s, b) $V_T = 2.5$ m/s [35]. 28

2.7 Simulated oil fraction by CFD in the symmetry plane of the gear. $V_T = 2.1$ m/s, $(h_R/)_1 = 0.10$ and $(h_R/)_2 = 0.40$, $\nu = 480$ cSt [40]. 29
2.8 Effect of gear rotation direction on oil bath deformation. . 30
2.9 Effect of housing shape on the deformation of the oil bath: comparison between the experiments of Jeon and Laruelle et al.[33, 43]. 31
2.10 Influence of oil viscosity on gear churning losses [51]. . . . 33
2.11 Schematic representation of data-driven modal analysis. . 45
2.12 Instantaneous velocity vector map (left side), and phase average vector map using the POD method (right side) [68]. 53
2.13 Singular value plot (left side) and mode coefficients correlation plot (right side) [66]. 54
2.14 Schematic of the experimental arrangement for planar 2D PIV [70]. 56
2.15 The cross-correlation technique is typically used in PIV. The position of the highest peak in the correlation plane indicates the most likely displacement vector.[73] 60

3.1 Photograph of the splash lubrication test rig installed in the THT Lab at the University of Florence. 68
3.2 High speed test rig layout. 70
3.3 Chamber layout. 71
3.4 Different geometries of the spiral bevel gears for the gear width. 72
3.5 Different geometries of the spiral bevel gears for pitch cone angle. 73
3.6 Different geometries of the spiral bevel gears for swirl angle of the teeth. 73
3.7 Mach number profile. 77
3.8 CFD result about windage for Gear I at 3500 rpm. 78
3.9 Conversion of a bevel gear into an equivalent cylindrical gear. 79
3.10 Mean spiral angle of spiral bevel gear. 80

3.11 Schematic of PIV measurement set-up - Front View. . . . 81
3.12 Schematic of PIV measurement set-up - Side View. 82
3.13 Picture of PIV measurement set-up (a) and measurement area (b). 83

4.1 Comparison windage power losses between shaft and Gear I 88
4.2 Comparison windage power losses between Gear I and Gear II. 89
4.3 Comparison windage power losses between Gear I, Gear C20 and Gear C50. 90
4.4 Comparison windage power losses between Gear I, Gear S0 and Gear S60. 91
4.5 Comparison between the experimental data and physical model results for Gear I and Gear II. 92
4.6 Comparison between the experimental data and physical model results for Gear I, Gear C20 and Gear C50. 92
4.7 Comparison between the experimental data and physical model results for Gear I, Gear S0 and Gear S60. 93
4.8 Oil level immersion depths for churning tests. 95
4.9 Churning post-process method. 96
4.10 Comparison churning power losses for Gear I at different oil levels. Oil used Aeroshell 500. 97
4.11 Comparison churning power losses for Gear II at different oil levels. Oil used Aeroshell 500. 97
4.12 Influence of geometric width on the evolution of torque, Gear I and Gear II with oil level $h/h_t = 1$. Oil used Aeroshell 500. 99
4.13 Influence of immersion depth on the evolution of torque, Gear I. Oil used Aeroshell 500. 99
4.14 Influence of immersion depth on the evolution of torque, Gear II. Oil used Aeroshell 500. 100
4.15 Comparison churning power losses for Gear I at different oil levels. Oil used Aerogear 823. 100

4.16 Influence of oil type on the evolution of churning power losses for Gear I and with oils at $32°C$. 101
4.17 Influence of oil type on the evolution of churning power losses for Gear II and with oils at $32°C$. 101
4.18 Comparison churning power losses for Gear I, Gear C50 and Gear C20. 102
4.19 Influence of pitch cone angle on the evolution of torque. . 103
4.20 Comparison churning power losses for Gear I, Gear S0 and Gear S60. 103
4.21 Influence of mean spiral angle on the evolution of torque. 104
4.22 Comparison between correlation and experimental results for churning. 104
4.23 Comparison between correlation and experimental results for churning. 105
4.24 Windage PIV result for Gear I at 500 rpm. 107
4.25 PIV average velocity magnitude with vectors of Gear I for three different speeds. 109
4.26 Instantaneous image with instantaneous velocity vectors. . 111
4.27 Mode coefficients correlation plot (top) and singular value plot (bottom). 113
4.28 Phase-averaged image calculated from POD phase-ordering procedure. 114
4.29 Phase-average velocity magnitude and vectors for Gear I for three different speeds. 116
4.30 Phase-average velocity magnitude and vectors varying cone angle. 118
4.31 Phase-average velocity magnitude and vectors varying mean spiral angle. 119
4.32 Phase-average velocity magnitude and vectors for high and low oil level of Gear I at 500rpm. 120
4.33 Phase-average velocity magnitude and vectors for different oils and velocities of Gear I. 122

List of Tables

2.1 Coefficients of the dimensional analysis formulation 17
2.2 Coefficients of the fluid flow analysis formulation. 18

3.1 Gears' characteristics with different Width 73
3.2 Gears' characteristics with different Cone Angle 74
3.3 Gears' characteristics with different Mean Spiral Angle . 74
3.4 Constant coefficients in Eq.3.3. 80

4.1 Windage test conditions. 88
4.2 Churning test conditions. 94
4.3 Oil properties 95
4.4 Velocimetry test conditions. 106

Bibliography

[1] Petry-Johnson, Travis T, Kahraman, A, Anderson, NE, and Chase, DR. "An experimental investigation of spur gear efficiency." 2008.

[2] Paschold, Constantin, Sedlmair, Martin, Lohner, Thomas, and Stahl, Karsten. "Efficiency and heat balance calculation of worm gears." *Forschung im Ingenieurwesen*, 84(2):115–125, 2020.

[3] Hildebrand, Lucas, Lohner, Thomas, and Stahl, Karsten. "A mechanism-based characterization of the load-independent power loss of dip-lubricated gears." *Proceedings of the Institution of Mechanical Engineers, Part J: Journal of Engineering Tribology*, 239 (10):1382–1400, 2025.

[4] Stadtfeld, Hermann J. The applications of bevel gears. In *Technical, Power Transmission Engineering*. The Gleason Works, 2014.

[5] Klingelnberg, Jan. "Bevel gear." *Fundamentals and Applications. Springer*, 2016.

[6] Niemann, Gustav, Winter, Hans, Höhn, Bernd-Robert, and Stahl, Karsten. *Maschinenelemente*, volume 1. Springer, 1975.

[7] Michaelis, Klaus. *Gear Oil Viscosity Recommendation*. Springer Berlin Heidelberg, Berlin, Heidelberg, 2014.

[8] Niemann, Gustav and Winter, Hans. "Getriebe allgemein, zahnradgetriebe-grundlagen stirnradgetriebe." *(No Title)*, 1989.

[9] Handschuh, Robert F and Kilmain, Charles J. Efficiency of high-speed helical gear trains. In *ANNUAL FORUM PROCEEDINGS-AMERICAN HELICOPTER SOCIETY*, volume 59, pages 1367–1378. AMERICAN HELICOPTER SOCIETY, INC, 2003.

[10] Quiban, R, Changenet, C, Marchesse, Y, Ville, F, and Belmonte, J. "Churning losses of spiral bevel gears at high rotational speed." *Proceedings of the Institution of Mechanical Engineers, Part J: Journal of Engineering Tribology*, 234(2):172–182, 2020.

[11] Eastwick, Carol N and Johnson, Graham. "Gear windage: a review." 2008.

[12] Von Karman, Th. On laminar and turbulent friction. Technical report, 1946.

[13] Goldstein, S. On the resistance to the rotation of a disc immersed in a fluid. In *Mathematical Proceedings of the Cambridge Philosophical Society*, volume 31, pages 232–241. Cambridge University Press, 1935.

[14] Dorfman, Lev Abramovich and Kemmer, N. "Hydrodynamic resistance and the heat loss of rotating solids." *(No Title)*, 1963.

[15] Townsend, Dennis P. *Dudley's gear handbook*. McGraw-Hill, 1992.

[16] Anderson, Neil E. *Spur-gear-system efficiency at part and full load*, volume 79. National Aeronautics and Space Administration, Scientific and technical, 1980.

[17] Anderson, Neil E and Loewenthal, Stuart H. "Effect of geometry and operating conditions on spur gear system power loss." 1981.

[18] Dawson, PH. "Windage loss in larger high-speed gears." *Proceedings of the Institution of Mechanical Engineers, Part A: Power and Process Engineering*, 198(1):51–59, 1984.

[19] Diab, Youssef, Ville, Fabrice, Velex, Philippe, and Changenet, Christophe. "Windage losses in high speed gears—preliminary experimental and theoretical results." *J. Mech. Des.*, 126(5):903–908, 2004.

[20] Voeltzel, Nicolas, Marchesse, Yann, Changenet, Christophe, Ville, Fabrice, and Velex, Philippe. "On the influence of helix angle and face width on gear windage losses." *Proceedings of the Institution of Mechanical Engineers, Part C: Journal of Mechanical Engineering Science*, 230(7-8):1101–1112, 2016.

[21] Ruzek, Michal, Ville, Fabrice, Velex, Philippe, Boni, Jean-Baptiste, and Marchesse, Yann. "On windage losses in high-speed pinion-gear pairs." *Mechanism and Machine Theory*, 132:123–132, 2019.

[22] Massini, Daniele, Fondelli, Tommaso, Andreini, Antonio, Facchini, Bruno, Tarchi, Lorenzo, and Leonardi, Federico. "Experimental and numerical investigation on windage power losses in high speed gears." *Journal of Engineering for Gas Turbines and Power*, 140(8):082508, 2018.

[23] Winfree, Don D. Reducing gear windage losses from high speed gears. In *International design engineering technical conferences and computers and information in engineering conference*, volume 35166, pages 747–756. American Society of Mechanical Engineers, 2000.

[24] Farrall, Mark, Simmons, Kathy, Hibberd, Stephen, and Young, Colin. Computational investigation of the airflow through a shrouded bevel gear. In *Turbo Expo: Power for Land, Sea, and Air*, volume 47268, pages 1259–1265, 2005.

[25] Johnson, Graham, Simmons, Kathy, and Foord, Colin. Experimental investigation into windage power loss from a shrouded spiral bevel gear. In *Turbo Expo: Power for Land, Sea, and Air*, volume 47950, pages 57–66, 2007.

[26] Webb, Thomas Andrew. *Power losses in spiral bevel gears*. PhD thesis, University of Nottingham, 2010.

[27] Zhu, Xiang, Dai, Yu, and Ma, Feiyue. "Development of a quasi-analytical model to predict the windage power losses of a spiral bevel gear." *Tribology International*, 146:106258, 2020.

[28] Akin, LS, Mross, JJ, and Townsend, DP. "Study of lubricant jet flow phenomena in spur gears." 1975.

[29] Zhu, Xiang, Dai, Yu, and Ma, Feiyue. "On the estimation of the windage power losses of spiral bevel gears: An analytical model and cfd investigation." *Simulation Modelling Practice and Theory*, 110: 102334, 2021.

[30] Quiban, Romain, Changenet, Christophe, Marchesse, Yann, and Ville, Fabrice. "Experimental investigations about the power loss transition between churning and windage for spur gears." *Journal of Tribology*, 143(2):024501, 2021.

[31] Terekhov, AS. "Hydraulic losses in gearboxes with oil immersion." *Russian Engineering Journal*, 55(5):7–11, 1975.

[32] Changenet, Christophe, Leprince, Gauthier, Ville, Fabrice, and Velex, Philippe. "A note on flow regimes and churning loss modeling." 2011.

[33] Laruelle, S., Fossier, C., Changenet, C., Ville, F., and Koechlin, S. "Experimental investigations and analysis on churning losses of splash lubricated spiral bevel gears." *Mechanics & Industry*, 18(4): 412, 2017.

[34] Polly, J, Talbot, David, Kahraman, Ahmet, Singh, Avinash, and Xu, Hai. "An experimental investigation of churning power losses of a gearbox." *Journal of Tribology*, 140(3):031102, 2018.

[35] Várhegyi, Zsolt and Kristóf, Gergely. "Mass flux distribution measurements and visualizations of a fluid sheet generated by a partially immersed dip-lubricated gear." *Periodica Polytechnica Mechanical Engineering*, 60(2):66–81, 2016.

[36] Luke, P and Olver, AV. "A study of churning losses in dip-lubricated spur gears." *Proceedings of the Institution of Mechanical Engineers, Part G: Journal of Aerospace Engineering*, 213(5):337–346, 1999.

[37] Leprince, Gauthier, Changenet, Christophe, Ville, Fabrice, and Velex, Philippe. "Investigations on oil flow rates projected on the casing walls by splashed lubricated gears." *Advances in Tribology*, 2012(1):365414, 2012.

[38] Hirt, Cyril W and Nichols, Billy D. "Volume of fluid (vof) method for the dynamics of free boundaries." *Journal of computational physics*, 39(1):201–225, 1981.

[39] Lucy, Leon B. "A numerical approach to the testing of the fission hypothesis." *Astronomical Journal, vol. 82, Dec. 1977, p. 1013-1024.*, 82:1013–1024, 1977.

[40] Liu, Hua, Jurkschat, Thomas, Lohner, Thomas, and Stahl, Karsten. "Detailed investigations on the oil flow in dip-lubricated gearboxes by the finite volume cfd method." *Lubricants*, 6(2):47, 2018.

[41] Chernoray, Valery and Jahanmiri, Mohsen. "Experimental study of multiphase flow in a model gearbox." *WIT Transactions on Engineering Sciences*, 70:153–164, 2011.

[42] Seetharaman, S, Kahraman, A, Moorhead, MD, and Petry-Johnson, TT. "Oil churning power losses of a gear pair: experiments and model validation." 2009.

[43] Jeon, Soo Il. *Improving efficiency in drive lines: an experimental study on churning losses in hypoid axle.* PhD thesis, Imperial College London, 2010.

[44] Fossier, Charlotte, Barday, Dennis, Changenet, Christophe, Ville, Fabrice, and Berier, Vincent. "Investigations on drive axle thermal behaviour: power loss and heat-transfer estimations." *SAE International Journal of Engines*, 11(03-11-01-0004):55–66, 2018.

[45] Changenet, Christophe and Velex, Philippe. "A model for the prediction of churning losses in geared transmissions—preliminary results." 2007.

[46] Chen, Sheng-Wei and Matsumoto, Susumu. "Influence of relative position of gears and casing wall shape of gear box on churning loss under splash lubrication condition—some new ideas." *Tribology Transactions*, 59(6):993–1004, 2016.

[47] AYEL, Jean. "Lubrifiants. propriétés et caractéristiques." *Techniques de l'ingénieur. Génie mécanique*, (B5340):B5340–1, 1996.

[48] LEPRINCE, Gauthier, Changenet, Christophe, Ville, Fabrice, Velex, Philippe, and JARNIAS, Frederic. Gle-01 influence of oil aeration on churning losses (gear lubrication and efficiency). In *The Proceedings of the JSME international conference on motion and power transmissions 2009*, pages 463–468. The Japan Society of Mechanical Engineers, 2009.

[49] Kolekar, Anant S, Olver, Andrew V, Sworski, Adam E, and Lockwood, Frances E. "Windage and churning effects in dipped lubrication." *Journal of Tribology*, 136(2):021801, 2014.

[50] Michaelis, K and Höhn, B-R. "Influence of lubricants on power loss of cylindrical gears©." *Tribology transactions*, 37(1):161–167, 1994.

[51] Mauz, Wolfgang. *Hydraulische Verluste von Stirnradgetrieben bei Umfangsgeschwindigkeiten bis 60m/s*. na, 1987.

[52] Changenet, Christophe and Velex, Philippe. "Housing influence on churning losses in geared transmissions." 2008.

[53] Neurouth, A, Changenet, C, Ville, Fabrice, Octrue, M, and Tinguy, E. "Experimental investigations to use splash lubrication for high-speed gears." *Journal of Tribology*, 139(6):061104, 2017.

[54] Boness, RJ. Churning losses of discs and gears running partially submerged in oil. In *Proceedings of the ASME International Power Transmission and Gearing Conference*, volume 1, pages 355–359. Chicago, 1989.

[55] Seetharaman, S and Kahraman, A. "Load-independent spin power losses of a spur gear pair: model formulation." 2009.

[56] Hussain, A. K. M. F. and Reynolds, W. C. "The mechanics of an organized wave in turbulent shear flow." *Journal of Fluid Mechanics*, 41(2):241–258, 1970.

[57] Giezendanner, R., Keck, O., Weigand, P., Meier, W., Meier, U., Stricker, W., and Aigner, M. "Periodic combustion instabilities in a swirl burner studied by phase-locked planar laser-induced fluorescence." *Combustion Science and Technology*, 175(4):721–741, 2003.

[58] Canepa, Edward, Lengani, Davide, Nilberto, Alessandro, Petronio, Daniele, Simoni, Daniele, Ubaldi, Marina, and Zunino, Pietro. "Flow coefficient and reduced frequency effects on wake-boundary layer interaction in highly accelerated lpt cascade." *International Journal of Turbomachinery, Propulsion and Power*, 6(3), 2021.

[59] Perrin, Rodolphe, Braza, Marianna, Cid, Emmanuel, Cazin, Sebastien, Barthet, Arnaud, Sevrain, Alain, Mockett, C, and Thiele, F. "Obtaining phase averaged turbulence properties in the near wake of a circular cylinder at high reynolds number using pod." *Experiments in Fluids*, 43(2):341–355, 2007.

[60] Mendez, MA, Balabane, M, and Buchlin, JM. "Multi-scale modal analysis of complex fluid flows." *preprint available in*, 2018.

[61] Mendez, Miguel A, Balabane, Mikhaël, and Buchlin, J-M. "Multi-scale proper orthogonal decomposition of complex fluid flows." *Journal of Fluid Mechanics*, 870:988–1036, 2019.

[62] Lumley, JL. "Stochastic tools in turbulence, courier corporation." 2007.

[63] Volkwein, Stefan. "Proper orthogonal decomposition: Theory and reduced-order modelling." *Lecture Notes, University of Konstanz*, 4 (4):1–29, 2013.

[64] Sirovich, Lawrence. "Turbulence and the dynamics of coherent structures. i. coherent structures." *Quarterly of applied mathematics*, 45(3):561–571, 1987.

[65] Sirovich, Lawrence. "Chaotic dynamics of coherent structures." *Physica D: Nonlinear Phenomena*, 37(1-3):126–145, 1989.

[66] Oudheusden, BW van, Scarano, F, Hinsberg, NP van, and Watt, DW. "Phase-resolved characterization of vortex shedding in the near wake of a square-section cylinder at incidence." *Experiments in fluids*, 39 (1):86–98, 2005.

[67] Lengani, Davide, Simoni, Daniele, Ubaldi, Marina, and Zunino, Pietro. "Pod analysis of the unsteady behavior of a laminar separation bubble." *Experimental thermal and fluid science*, 58: 70–79, 2014.

[68] Lengani, Davide, Simoni, Daniele, Ubaldi, Marina, Zunino, Pietro, and Bertini, Francesco. "A pod-based procedure for the split of unsteady losses of an lpt cascade." *International Journal of Turbomachinery, Propulsion and Power*, 2(4), 2017.

[69] Ben Chiekh, M, Michard, Mare, Grosjean, Nathalie, and Bera, JC. "Reconstruction temporelle d'un champ aérodynamique instationnaire à partir de mesures piv non résolues dans le temps." *Proceedings of 9ème Congrès Francophone de Vélocimétrie Laser, Brussels, Belgium*, 2004.

[70] Raffel, Markus, Willert, Christian E, Scarano, Fulvio, Kähler, Christian J, Wereley, Steve T, and Kompenhans, Jürgen. *Particle image velocimetry: a practical guide*. springer, 2018.

[71] Atkins, MD. Velocity field measurement using particle image velocimetry (piv). In *Application of thermo-fluidic measurement techniques*, pages 125–166. Elsevier, 2016.

[72] Willert, Christian E and Gharib, Morteza. "Digital particle image velocimetry." *Experiments in fluids*, 10(4):181–193, 1991.

[73] Wieneke, Bernhard. *PIV Uncertainty Quantification and Beyond*. PhD thesis, 12 2017.

[74] Pereira, Francisco, Stüer, Heinrich, Graff, Emilio C, and Gharib, Morteza. "Two-frame 3d particle tracking." *Measurement Science and Technology*, 17(7):1680, jun 2006.

[75] WESTERWEEL, Jerry and ADRIAN, Ronald J. *Particle image velocimetry Ronald J. Adrian, Jerry Westerweel*. Cambridge University Press, 2011.

[76] Takehara, Kohsei and Etoh, Takeharu Goji. "A study on particle identification in ptv particle mask correlation method." *Journal of Visualization*, 1:313–323, 1998.

[77] Ohmi, Kazuo and Li, Hang-Yu. "Particle-tracking velocimetry with new algorithms." *Measurement Science and Technology*, 11(6):603, jun 2000.

[78] Baek, S.J. and Lee, S.J. "A new two-frame particle tracking algorithm using match probability." *Experiments in Fluids*, 22:23–32, 01 1996.

[79] Hassan, Y.A., Blanchat, T.K., Seeley, C.H., and Canaan, R.E. "Simultaneous velocity measurements of both components of a two-phase flow using particle image velocimetry." *International Journal of Multiphase Flow*, 18(3):371–395, 1992.

[80] Lin, T.-J., Reese, J., Hong, T., and Fan, L.-S. "Quantitative analysis and computation of two-dimensional bubble columns." *AIChE Journal*, 42(2):301–318, 1996.

[81] Xu, Jiayu, Zhang, Shuai, and Ge, Wei. "An efficient non-spherical particle tracking strategy based on deep-learning and simulation-experiment integration." *Powder Technology*, 468:121681, 2026.

[82] Tinevez, Jean-Yves, Perry, Nick, Schindelin, Johannes, Hoopes, Genevieve M., Reynolds, Gregory D., Laplantine, Emmanuel, Bednarek, Sebastian Y., Shorte, Spencer L., and Eliceiri, Kevin W. "Trackmate: An open and extensible platform for single-particle tracking." *Methods*, 115:80–90, 2017.

[83] Stringer, Carsen, Wang, Tim, Michaelos, Michalis, and Pachitariu, Marius. "Cellpose: A generalist algorithm for cellular segmentation." *Nature Methods*, 18(1):100–106, Dec 2020.

[84] Hessenkemper, H., Starke, S., Atassi, Y., Ziegenhein, T., and Lucas, D. "Bubble identification from images with machine learning methods." *International Journal of Multiphase Flow*, 155:104169, 2022.

[85] Elhimer, M., Praud, O., Marchal, M., Cazin, S., and Bazile, R. "Simultaneous piv/ptv velocimetry technique in a turbulent particle-laden flow." *Journal of Visualization*, 20(2):289–304, Oct 2016.

[86] Bröder, D. and Sommerfeld, Martin. "An advanced lif-plv system for analysing the hydrodynamics in a laboratory bubble column at higher void fractions." *Experiments in Fluids*, 33:826–837, 12 2002.

[87] Honkanen, Markus and Saarenrinne, Pentti. Turbulent bubbly flow measurements in a mixing vessel with piv. 11th Symp. on Applications of Laser Techniques to Fluid Mechanics (7-10 July 2002, Lisbon, Portugal), 01 2002.

[88] Hartono, Erwin Adi, Golubev, Maxim, and Chernoray, Valery. Piv study of fluid flow inside a gearbox. In *PIV13; 10th International Symposium on Particle Image Velocimetry, Delft, The Netherlands, July 1-3, 2013*. Delft University of Technology, Faculty of Mechanical, Maritime and . . . , 2013.

[89] Hartono, Erwin Adi, Pavlenko, Alexandr, and Chernoray, Valery. Stereo-piv study of oil flow inside a model gearbox. In *17th international symposium on applications of laser techniques to fluid mechanics*, pages 07–10, 2014.

[90] Bongiovanni, C, Chevaillier, J Ph, and Fabre, J. "Sizing of bubbles by incoherent imaging: defocus bias." *Experiments in Fluids*, 23(3): 209–216, 1997.

[91] Tokuhiro, A., Maekawa, M., Iizuka, K., Hishida, K., and Maeda, M. "Turbulent flow past a bubble and an ellipsoid using shadow-image and piv techniques." *International Journal of Multiphase Flow*, 24 (8):1383–1406, 1998.

[92] Lindken, Ralph and Merzkirch, Wolfgang. "A novel piv technique for measurements in multiphase flows and its application to two-phase bubbly flows." *Experiments in fluids*, 33(6):814–825, 2002.

[93] Honkanen, Markus, Saarenrinne, Pentti, Stoor, Tuomas, and Niinimäki, Jouko. "Recognition of highly overlapping ellipse-like bubble images." *Measurement Science and Technology*, 16(9):1760, jul 2005.

[94] Bröder, D and Sommerfeld, M. "Planar shadow image velocimetry for the analysis of the hydrodynamics in bubbly flows." *Measurement Science and Technology*, 18(8):2513, jul 2007.

[95] Honkanen, M. and Marjanen, K. Analysis of the overlapping images of irregularly-shaped particles, bubbles and droplets. In *Proceedings of ICMF 2007 6th International Conference on Multiphase Flow, Leipzig, Germany, 9.-13.7.2007*, 2007.

[96] Dulin, V. M., Markovich, D. M., and Pervunin, K. S. "The optical principles of pfbi approach." *AIP Conference Proceedings*, 1428(1): 217–224, 03 2012.

[97] Akhmetbekov, Yerbol K., Alekseenko, Sergey V., Dulin, Vladimir M., Markovich, Dmitriy M., and Pervunin, Konstantin S. "Planar fluorescence for round bubble imaging and its application for the study of an axisymmetric two-phase jet." *Experiments in Fluids*, 48 (4):615–629, Jan 2010.

[98] Cigada, Alfredo et al. "Strumenti e metodi di misura." 2004.

[99] S. Brocchi, R. Becchi B. Facchini G. Lo Santo M. Konle A. Andreini A. Fratini. Windage power losses in high-speed spiral bevel gears: A preliminary experimental and numerical evaluation. American Society of Mechanical Engineers, 2026.

[100] Sharma, Richa and Kamra, Amit. A review on clahe based enhancement techniques. In *2023 6th International Conference on Contemporary Computing and Informatics (IC3I)*, volume 6, pages 321–325, 2023.